SOUNDING ROCKET XUV OBSERVATIONS OF CAPELLA

Thesis by

Norman Bobroff

In Partial Fulfillment of the Requirements

for the Degree of

Doctor of Philosophy

California Institute of Technology

Pasadena, California

1983

(Submitted on October 22, 1982)

Dedication

to my parents,

Allen and Ethel Bobroff

for their many years of encouragement

and

to my wife,

Ann

for all her love and support

Acknowledgements

The successful flight of the sounding rocket XUV spectrometer constructed for this observation of Capella owes much to a very dedicated group of individuals at Caltech, the Sounding Rockets Division of the Goddard Space Flight Center, and the White Sands Missile Range.

I inherited a largely completed telemetry emulator, based on a sound (well documented!!), and inherently flexible design, from Stu Buchanan, which provided a cornerstone upon which the payload electronics system was designed and built. I would especially like to thank Mike Juda for his considerable aid in the electronic systems debugging, the NBS calibration, and the diffraction grating fabrication. Dean Davey provided some early assistance with the mechanical design of the payload and Mel Kriegel flawlessly carried out much of the machining.

Dr. John Nousek made substantial contributions to the project. He was responsible for design of the CEMA vacuum system and provided considerable advice, many useful suggestions, and an essential calming influence to the project. John was an integral part of all phases of the interfacing with GSFC and the final launch preparations at WSMR. George Kraft of the Goddard Space Flight Center deserves special thanks as our patient "mission mother", steering us through many physical and bureaucratic obstacles in an effort to meet our launch date and coordinating the integration of the many rocket systems. I would like to thank Ted Cannon of GSFC for useful discussions concerning details of the payload electronics and telemetry interfacing. Don Patterson and Ed Beatty of WSMR are also thanked for their considerable assistance in the hectic time before launch. Robert Madden, Steve Ebner, and Lanny Huey of the NBS

were responsible for our calibration effort at the SURF II synchrotron. Dino Ciarlo of Lawrence Livermore Labs was instrumental in the fabrication of the diffraction gratings.

I would like to thank Dr. Jeff Linsky for helpful discussions regarding the formation of the He II 304 Å line, as well as Dr. Tom Ayres for his comments, and providing preliminary results of the Capella IUE monitoring. John Nousek also provided much input to the analysis of the flight data and his mark is certainly left on this thesis. Dr. Edward Stone contributed a large number of suggestions regarding the text and analysis and I appreciate his taking the time to read and assist me in finishing my thesis.

I express great appreciation to my advisor Dr. Gordon Garmire for his patient support in the development of this project. I was allowed full responsibility for a very large and unique undertaking and thus acquired a very wide range of knowledge about cool type stars, the interstellar medium, and the details of designing and debugging a large electronics system. Gordon provided assistance at crucial moments and allowed me the independence to learn from my mistakes.

I owe much to Ann Bobroff for her love and consideration, and for her help with the manuscript. I would also like to thank my colleagues at Caltech and elsewhere for their stimulating discussions and supportive friendship: Mark Bowick, John and Ellen Markey, Erich Grossman, David Ennis, Ken Jensen, John Nugent, Kristen Sellgren, Sarbmeet Kanwal, Michael Weimer, Jeff White, and Lars Hernquist. Special thanks to Pat Neill, a resource of skilled knowledge and a friend whose help I will always appreciate. I offer thanks to my undergraduate advisors at the University of Chicago, V. L. Telegdi and Bruce Winstein for stimulating my interest in physics, and to my extended family whose love will always

be a source of strength: Sondra and Carol Bobroff, all the Levines, Mr. and Mrs. Eggerding, and Grandma Bos.

My first three years of graduate study were support by a National Science Foundation Fellowship for which I am very grateful.

ABSTRACT

Capella (d=13pc) was observed in the 170 Å to 450 Å band by a sounding rocket borne spectrometer with a spectral resolution of 35 Å FWHM. Minimum flux sensitivity varies with wavelength and a 2σ upper limit is 0.25 and 0.6 photons $cm^{-2}s^{-1}$ at 180 Å and 304 Å respectively. The prominent stellar emission line in this bandpass is He II 304 Å. The Capella flux at earth in this line is expected to be in the range 2.8 to 5.4 photons $cm^{-2}s^{-1}$ in the absence of interstellar extinction. Interstellar absorption was computed from the Copernicus satellite measure of the neutral hydrogen column density, N(H I)= $1.2\times10^{18}cm^{-2}$, towards Capella and a ratio of N(He I)/N(H I)=0.1. The 50% attenuation at 304 Å results in a flux at earth of 1.4 to 2.7 $phcm^{-2}s^{-1}$.

No significant Capella flux was detected in the bandpass despite inflight verification of instrument's sensitivity obtained from observations of the He II 304 Å geocoronal emission. The most reasonable explanation for the absence of the 304 Å line is that absorption in the intervening medium exceeds that predicted from N(He I) = 0.1N(H I). A lower limit to the Capella line of sight N(He I) is determined from the 304 Å observation. We find that N(He I)/N(H I) is greater than 0.4. A helium to hydrogen abundance ratio of 0.1 is retained if the hydrogen ionization in the local interstellar medium (LISM) exceeds 60%. Several models of the LISM which incorporate this ionization fraction are treated for self consistency, as well as compatibility with observations of the temperature and ionization fraction of the interplanetary medium. The most plausible model consists of a local, warm (10,000 K), gas embedding the solar system, surrounded by a hot ($10^5 \rightarrow 10^6$ K) plasma. Ionization of hydrogen in the warm cloud must be maintained by a local interstellar radiation field.

Table of Contents

		page
Acknowledgements		iii
Abstract		vi
Chapter I.	**Overview**	1
1.1	Introduction	
1.2	Coronal Phenomena in Cool Stars	
1.3	The Binary System Capella	
1.4	The Nature of a Capella XUV Observation	
Chapter II.	**The Sounding Rocket Spectrometer**	19
2.1	Spectrometer System	
2.2	Support Systems	
Chapter III.	**The Pre-Flight Calibration**	41
3.1	Introduction	
3.2	The SURF II Facility	
3.3	Efficiency loss in the NBS CEMA; The Flight Plate	
3.4	Results of the NBS Calibration	
Chapter IV.	**Observations of Capella**	80
4.1	Vehicle and Support System Performance	
4.2	The Inflight Geocoronal Photon Background	
4.3	The Capella Spectrum; Upper Limit Fluxes	
Chapter V.	**Implications of the Capella Observation**	107
5.1	Introduction	
5.2	The Capella He II flux reconsidered	
5.3	Models with Absorption	
5.4	Coronal line emission in the Bandpass	
5.5	Summary	
References		133

CHAPTER 1

1.1 Introduction

The advent of satellite borne x-ray telescopes has greatly increased the sensitivity to low luminosity soft x-ray sources. Specifically, the capability now exists of observing local stellar objects whose total x-ray luminosity (L_x) is not much greater than solar (10^{27} ergs/s). A remarkable result of the recent High Energy Astrophysical Observatory (HEAO I; Walter et al 1980) and Einstein (Vaiana et al 1981) stellar surveys has been the detection of hot, coronal plasmas associated with stars occupying nearly every spectral class. Furthermore, within a given spectral class, the ratio of x-ray to total luminosities can vary by several orders of magnitude. The ubiquity of coronal phenomena and indications that spectral class alone may not be the essential ingredient in determining total L_x, were not anticipated by the widely accepted acoustic heating models evolved to account for the solar atmospheric structure (Stein and Leibacher 1974, Ulmschneider 1979). Substantial revision in our understanding of the physics of coronal formation has been mandated.

The delineation of the detailed structure of the outer atmosphere is an important aspect of the stellar coronal formation problem. This structure manifests itself through spectral emission lines characteristic of the underlying temperature, density, and physical processes in the region of formation. Soft x-ray emission originates primarily in the corona where the temperature exceeds a million degrees. Lines in the XUV (100 -> 1000 Å) are copiously produced in a 10^4 - 10^6 K plasma. EUV (1000 Å - 2000 Å) spectra primarily originate in regions

where the temperature ranges from 10^4 K to a few times 10^5 K. Measurements of these spectra not only provide a data base against which future, comprehensive models of atmospheric emission can be tested, but also are useful in isolating those stellar parameters which underlie the non-radiative heating processes in the outer atmospheres of cool stars. Thus, observations will probably provide substantial input to the direction of theoretical work.

To date the sun is the only star to have been extensively studied in the entire 100 Å to 2,000 Å band. While recent spatially resolved studies of the solar spectrum have allowed for some discerning of the differences in atmospheric structure caused by magnetic fields and local activity levels, fundamental parameters such as surface gravity, convective activity, surface magnetic fields and rotation cannot be varied. Clearly there is considerable motivation to encompass a wide variety of stellar objects in x-ray, XUV, and EUV studies.

Observations in the EUV and XUV also provide a unique opportunity to study the composition, density, temperature, and ionization structure of the nearby interstellar medium. The XUV portion of the spectrum is particularly sensitive to the column density of H I below 912 Å, He I below 504 Å, and He II below 227 Å. Column densities of neutral hydrogen have been deduced along lines of sight to several nearby stars (including Capella) from the Lyα absorption; however, no observations sensitive to the neutral helium column densities have been made. This Capella observation at 304 Å coupled with the Copernicus satellite measurement of the Capella H I column density is thus potentially sensitive to He I. This point is discussed in considerable detail in section 5.3.

The primary objective of the work summarized in this thesis was to observe the XUV spectrum of the nearby binary system Capella. Subsequent sections of this chapter review the problem of coronal formation with emphasis on Capella

as a model testing ground. Detailed consideration is given to the formation and interpretation of the XUV spectra, particularly the He II lines formed in the stellar transition region. Finally, the feasibility of a XUV observation of Capella is summarized, incorporating anticipated interstellar absorption, geocoronal background, and instrumental capabilities.

1.2 Coronal Phenomena in Cool Stars

Coronal Formation

The temperature profile of the solar atmosphere is expected to be typical of stars having comparable surface temperature. The temperature in the solar atmosphere falls from about 5,600 K in the photosphere to a minimum of 4,000 K in the mid chromosphere. It then rises gradually to about 10,000 K in the upper chromosphere before rapidly increasing through the narrow (a few hundred kilometers thick) transition region (TR) to coronal values exceeding 10^6 K. Existence of TR and corona was surmised over forty years ago; however, a concise understanding of the formation mechanism and physics of the outer solar atmosphere remains elusive.

Prior to the Einstein stellar survey (Vaiana et al 1981), a general consensus had been reached that the solar outer atmosphere was heated by the dissipation of energy contained in upward propagating acoustic waves. Wave motion is generated in the turbulent environment of the surface convective zone (Reviews are given by Stein and Leibacher 1979, and Ulmschneider 1979). Detailed considerations of atmospheric propagation indicated that waves of about 300 seconds period were capable of transferring energy to the upper chromosphere. It was also deduced that waves of this period would be copiously produced in the surface convective zone. Indirect, but very leading, observational support for this model came from time series analysis of the chromospheric Ca II line Doppler shifts which indicated the presence of waves possessing a period of approximately 300 seconds (Liu 1974). Subsequent observations were undertaken to search for similar waves in higher temperature TR lines. Power spectra in the line of C IV (1549 Å) formed at 10^5 K were taken by the OSO VIII satellite. From these data Athay and White (1978) concluded that the acoustic flux present in

the TR was at least a factor of 30 below that required to heat the corona. Reanalysis of the OSO VIII C IV data by Bruner and McWhirter (1979) has pushed the discrepancy to a factor of approximately a thousand.

Spatially resolved, x-ray images of the solar corona show that emission originates primarily in magnetically confined loop structures. This has raised additional problems for the solar acoustic heating models. It is now felt that some form of magnetic heating (Linsky 1980 and references therein), possibly through magnetic generation of electrical currents, may be the dominant source of energy input.

The greatest difficulties for the acoustic heating models have been raised by the results of the HEAO I (Walter et al 1980) and Einstein (Vaiana et al 1981) x-ray surveys, and the IUE ultraviolet (Linsky and Ayres 1978; Ayres, Marstad, and Linsky 1981) stellar surveys. Strong convective zones, essential to effective wave generation, are only expected on stars with spectral class similar to solar (G2 V) (Linsky and Haisch, 1979). Furthermore, convective activity is expected to be inversely proportional to surface gravity (Linsky 1980), so that within a given spectral class, ratios of x-ray to bolometric luminosities are expected to be approximately constant. These model features imply confinement of coronal activity to discrete regions of the HR diagram (Mullan 1978; Linsky and Haisch 1979), and predict that within a given spectral class L_x / L_{bol} will be roughly constant. As noted in Section 1.1 both these assumptions were demonstrated to be incorrect.

In an important work Ayres, Marstad, and Linsky (1981; hereafter AML) combined data from the IUE and Einstein stellar observations to compare the relative efficiencies of non-radiative heating in the upper chromosphere, the transition region, and the corona. From a sample of F-K dwarfs and giants the

intensities of sequentially increasing temperature emission lines were compared with that of the mid-chromospheric Mg II (2800 Å) line. Scatter plots of fluxes in the lines of O I (8000 K), Si II (10,000 K), C II (20,000 K), Si IV (80,000 K), C IV (10^5 K), NV (2×10^5 K), and soft x-rays against Mg II (8,000 K) were constructed. All line fluxes are normalized to L_{bol}. AML find a general trend for a power law correlation between the normalized line fluxes f_l and the Mg II flux, f_{MgII} of the form $f_l \sim f_{MgII}^{\alpha}$. They find α = 1 for O I and Si II, $\alpha \cong$ 1.5 for C II, $\alpha \cong$ 1.5 for Si IV, C IV, N V, and $\alpha \cong$ 3 for soft x-rays. The authors suggest that different mechanisms are responsible for heating distinct layers of the atmosphere though clearly interaction between the layers must also be considered.

Expansion of the observational data base has forced considerable revision of our understanding of the important physical process in stellar atmospheres. Extensive knowledge of the spectra and physical parameters of a few of the detected stars in the x-ray and EUV surveys will also provide considerable input to model making. The binary system Capella, discussed in detail in Section 1.3, is a particularly clear example of this. Capella consists of two giants of comparable mass, surface temperature, and radius, yet possessing vastly different coronal emission measures. The distinctive property of the x-ray bright secondary is its high rotational velocity (~ 40 km/s) compared to the primary (~ 5 km/s) (Ayres and Linsky 1980). Models of coronal formation are now focusing on the connection between surface convection and rotation, and the ensuing magnetic field structure.

The Formation of Helium Spectra

Lines of He II formed in the upper chromosphere and TR, are particularly sensitive to the structure and physical process active in the outer atmosphere.

We focus primarily on emission at 304 Å from the 2p → 1s transition, 256 Å from 3p → 1s, and 1640 Å corresponding to 3s,3p,3d → 2s,2p. Hearn (1969) first suggested the usefulness of these lines as TR temperature and density diagnostics, however substantial disagreement regarding the formation mechanism of these lines has inhibited their usefulness. Recent observational evidence and improving theory have converged to eliminate much of the debate over the roles in line formation played by electron collisional excitation and recombination following photoionization by coronal photons short of the 227 Å ionization edge. As a coherent picture of He II spectra formation emerges, its diagnostic value will be useful for local stellar objects, as well as the sun.

Pure collisional models of the He II 304 Å line were computed by Milkey, Heasley, and Beebe (1973), and particularly by Jordan (1975). Jordan used the emission measures implied by EUV line fluxes in the solar spectrum to model the distribution of emission measure ($\int_{\delta h} n_e^2 \, dh$; where n_e is the electron density and the integral is over the region of altitude δh at approximate temperature T) with temperature in the TR. The electron density in the region of temperature T is given by the assumption that the pressure, $n_e T \cong 5.6\times10^{14}$, is constant through the TR. The model ignores effects of radiative transfer on the ionization equilibrium despite the fact that both coronal radiation and the 304 Å line can increase the fraction of He II relative to He I in the cooler regions of the atmosphere. Because of the low TR election densities, collisional damping is unimportant for resonance lines. Integrating the contribution to 304 Å emission from each temperature region, the total model 304 Å flux was found to be a factor of five below the observed value. This was considered a significant discrepancy in spite of uncertainties in the solar emission measures and the constant pressure assumptions. The observation that He II lines (256 Å, 304 Å,

and 1640 Å) are significantly weakened in coronal holes while strengths of the TR lines of C IV, S IV, and N V were not appreciably altered, (Huber et al 1974) poses an additional problem for collisional models. Decreased emission in coronal holes was a major motivation behind the concept that the helium lines were formed by recombination (Zirin 1975) following photoionization of He I and He II by coronal radiation.

The photoionization-recombination (P-R) method of forming the solar helium spectra has received a heuristic treatment by Zirin (1975). In this model coronal radiation short of 227 Å photoionizes He II, and recombinations of the resulting He III produce a 304 Å photon 70 percent of the time. The net result of the P-R mechanism is to convert the coronal flux short of 227 Å to 304 Å. The 304 Å flux radiated downward further contributes to the photoionization of He I. Recombination of He II leads to formation of the triplet as well as singlet ground states in He I. Presence of the triplet state is indicated by the presence of a 10830 Å absorption feature in solar and stellar spectra. Since the triplet state is formed in the cool chromosphere where it cannot be excited by electron collision its presence is expected to be indicative of the 304 Å emission and hence total coronal flux. An important prediction of this model is that spatially resolved spectrograms of the sun should show high correlation between the n=2->1 transition (304 Å), and the transition from the n=3 level (1640 Å, 256 Å). High resolution spectrograms taken in 256 Å and 304 Å (Glackin et al 1978, Mango et al 1978) showed an absence of correlation between the n=3 and n=2 lines. An additional problem for the P-R mechanism of 304 Å production is that central reversal of the line profile is predicted (Milkey 1975). High dispersion spectra at 304Å show the profile to be essentially gaussian (Doschek, Behring, and Feldman 1974). As noted by Zirin (1975) the relative fluxes in the transitions from the n=8, n=6, and n=3 levels are in good agreement with P-R

predictions.

An important advance in the theory of solar helium spectra formation was the simultaneous treatment of both collisional and photoionization processes on helium ionization equilibrium and line excitation (Avrett, Vernazza, and Linsky, 1976; hereafter AVL). The ionizing flux radiated inward from the corona is estimated from the values obtained at one AU. The attenuation of this flux depends on the model opacity as a function of altitude, a function of the hydrogen and helium ionization equilibrium and densities. In turn the ionization equilibrium depends on the coronal flux and the model emission from the 227 Å recombination edge of He II and the 304 Å flux. The model is solved in a self-consistent approximation. AVL also included a more sophisticated TR model than the constant pressure one adopted by Jordan. The primary conclusions of their work are that recombination following photoionization is responsible for producing the He I and He II continuum emission, as well as excitation of the n=3 level lines, while 304 Å is essentially a collisional line. Thus, the 256 Å, and 1640 Å lines are formed in the cool low TR while 304 Å is a 10^5 K line produced by collisions. The physical reason for the small contribution of collisional excitation to the $n \geq 3$ level is the somewhat higher excitation threshold which appears exponentially in the collisional cross-section. The contribution of photoionization to the formation of 304 Å was shown to be diminished by absorption in He I of most of the coronal flux short of 227 Å.

Observational evidence favoring the AVL conclusions results from the lack of spatial correlation between 304 Å and 256 Å intensities over the solar disk (Glackin et al 1978, Mango et al 1978) indicating different formation mechanisms for each line. Spatial chromospheric network structure observed in TR zone lines was also present in the 304 Å emission, but not in the 256 Å line. The AVL model also shows good agreement with the 227 Å (He II) and 504 Å

recombination continuum spectra which are produced by P-R, as well as with the emergent 304 Å line profile. The predicted 304 Å flux remains a factor of about two below the observed. The persisting challenge to collisional models is to account for the weakening of 304 Å emission in coronal holes where other high temperature TR zones are not strongly affected.

A plausible explanation for both the low model flux and the coronal hole line weakening is that He II ions diffuse from their region of formation up the TR temperature gradient where collisional excitation is enhanced (Shine, Gerola, and Linsky 1975). In the standard collisional models (Jordan 1975, AVL 1976) ionization equilibrium at each temperature T is computed and, together with the emission measure and excitation cross section at that temperature, the total line flux originating at temperature T is calculated. An assumption of these models is that He II ions produced at T are also collisionally excited by electrons at T. Because of the very steep temperature gradients in the transition region, it is possible for He II ions formed at one temperature to drift to regions of higher temperatures where collisional population of the n=2 state is enhanced. The effectiveness of this enhancement mechanism is limited by the distance ions can drift before their ionization equilibrium becomes consistent with the local temperature, i.e., the n=2 state of He II is excited until the He II becomes He III. In a heuristic treatment of the problem Shine, Gerola, and Linsky (1975) found that the He II 304 Å line could be enhanced by factors of 3 to 4 by diffusion in the region $T>10^5$ K. The EUV lines (e.g. C IV 1549) are not enhanced significantly by the mechanism because of their lower excitation threshold. Diffusion may simultaneously account for the discrepancy between model and observed fluxes and the weakening of the line in coronal holes where the emission measures of the high temperature material is lessened. Direct observational support for such an effect is not available. A precise treatment of the theory has not been

undertaken, and the model remains speculative.

In summary the formation mechanisms of the helium spectral lines appear to be moderately well understood, however uncertainties in the TR structure and the extent to which processes such as diffusion contribute to line formation persist. Study of the problem in the atmosphere of Capella which is considerably more active than the sun, and possesses vastly greater high temperature emission measures, may aid greatly in the removing of some of the uncertainties in the theory of formation of this very basic emission line.

1.3 The Binary System Capella

The spectroscopic binary system Capella (d=13pc) is an extremely interesting example of a cool star possessing a corona. It was the first stellar soft x-ray source detected (Catura, Acton and Johnson 1975) and x-ray spectra from the system have been obtained from the HEAO I (Cash et al 1978) and Einstein (Holt et al 1981) satellites. EUV spectra were first taken by the Copernicus satellite (Dupree 1975). With its improved sensitivity an extensive EUV data base on Capella has been provided by the IUE (Ayres and Linsky 1980, hereafter AL).

The two components of the widely separated (1AU) 104 day period binary are giant stars of comparable mass, the primary is about 2.6 $M_{\odot}$ while the secondary is 2.5 $M_{\odot}$. Their spectral types are similar (the primary is G6 III and secondary F9 III), as are their radii ($R^a \sim 11.5R_{\odot}$, $R^b \sim 7.1R_{\odot}$), and surface temperatures ($T^a \sim 5{,}100$ K, $T^b \sim 6{,}000$ K; AL 1980). Aside from their size, they are quite similar to the sun (G2 V, $T_{\odot} \sim 5{,}600$ K). The most significant difference between the two components is the equatorial rotation velocities of about 5 km/s for the primary and 40 km/s for the secondary. The solar $V_{rot} \sim 5 km/s$. The spectrum of the primary also shows significant lithium depletion while the secondary is normal in this regard. An evolutionary scenario for the two giants has been prepared by Iben (1965). The slightly more massive primary has evolved past the helium flash point on the giant track while the secondary is still approaching this stage. The primary has developed deep convective zones, which account for its observed depletion of lithium while the secondary appears normal in lithium. Within this framework the largely different rotation velocities of the two stars at nearly identical positions in the HR diagram can be accounted for by either magnetic baking of the secondary through interaction between its fields and convection zones, or mass loss at helium flash. It is also

possible that their main sequence progenitors had different rotation rates.

Soft x-ray spectra from Capella have been analyzed by Cash et al (1978) and Holt et al (1981). The spectrum contains substantial temperature components in the range from $10^6 \rightarrow 7\times10^7$ K with emission measures exceeding solar by a factor of 10^4. The ratio of x-ray luminosities (L_x) to total luminosity (L_{bol}) is about 2×10^{-5} for Capella compared with 10^{-6} for the sun. Capella thus possesses a considerably hotter, more active outer atmosphere than the sun.

EUV studies of Capella were first carried out with Copernicus (Dupree 1975), however the low sensitivity of the instrument limited coverage to only a few of the brightest lines. The IUE has obtained extensive EUV spectra of Capella in the low (6 Å FWHM) and high (0.1 Å FWMM) resolution modes. Absolute fluxes in about thirty lines in the 1000 Å to 2000 Å band have been determined. These lines cover the temperature range from 10^4 in the upper chromosphere to about 5×10^5 K at the TR-corona boundary (See Table 1.3A). Detailed analysis of the high resolution line profiles as a function of orbital phase led to the conclusion (AL 1980) that nearly all the high temperature emission from the system was associated with the rapidly rotating secondary. With this assumption surface fluxes in the high temperature EUV lines were found to be factors of 50 to 90 times their solar counterpart. Comparison between the two Capella system components and the sun have greatly supported the hypothesis that rotation is a crucial parameter in the non-radiative heating problem (e.g. AL, Hartmann, Dupree and Raymond, 1981). Though few of the stars detected in the Einstein survey have known rotation rates, those which do show a correlation between their rotational velocities and the ratio L_x to L_{bol} (Vaiana et al 1981).

Clearly the presence of many similarities and a few differences between each Capella component and the sun make the three stars particularly useful cases

from which to increase our understanding of the surprisingly widespread phenomena of stellar activity. Emission in the XUV band has only been studied in the solar atmosphere. Detection of an XUV spectra has been reported from only one extra-solar object, the white dwarf HZ 43 (Malina, Bowyer, and Paresce 1978). This region contains the very interesting TR line of He II 304 Å, as well as several important coronal lines of Fe which are very useful diagnostics of the emission measure at particular temperature in the corona. When XUV line spectra become available they will provide for greater coronal diagnostic value than the present soft x-ray continuum observations. Capella's proximity and large EUV and coronal fluxes give it excellent potential to be detected in the XUV with current state of the art instrumentation. The parameters relevant to a Capella observation are assessed in the following section. These include source flux, interstellar absorption, background source, and the sensitivity of present instrumentation.

1.4 The Nature of a Capella XUV Observation

Flux estimates for the XUV lines and particularly He II can be made on the basis of the observed EUV emission. As discussed in section 1.2 He II 304 Å is a collisionally excited line, produced in the temperature range from 8×10^4 K to 5×10^5 K. Although a precise theory accounting for the absolute flux in the solar line is unavailable, it is reasonable to assume that the total intensity of the 304 Å line will scale with the emission measures in this temperature range. The emission measures are reflected by the intensities in the EUV lines. Thus, the ratio of Capella to solar emission measures at T is expected to be comparable to the ratio of intensities of the EUV lines formed at T. This provides a method of predicting the Capella flux which is independent of the details of the TR structure, and the accuracy to which the solar high temperature emission measures are known. Sensitivity to emission measures at these temperatures are provided by the IUE absolute fluxes from Si IV (1394 Å, 6-> 8×10^4 K), C IV (1500 Å, 10^5 K), N V (1240 Å, 2×10^5 K) and O VI (1032 Å,4×10^5 K). Estimates of the Capella 304 Å intensity at earth are deduced from the ratio, at earth, of the flux in each of the above Capella lines to their solar counterpart. This ratio is then used to scale the solar He II flux at earth thus giving an estimate of the Capella He II flux at earth in the absence of absorption in the interstellar medium. The solar He II 304 Å flux at earth is 8×10^9ph-cm^{-2} s^{-1} (AVL, Timothy 1977, Glackin et al 1978) during periods of low activity. The fluxes in the solar EUV lines are also taken at periods of low activity. Recent monitoring of the solar EUV and XUV spectra indicates that the variation in the He II 304 Å line tracks very closely with that of the 10^5 K lines providing further support that He II is produce in this temperature regime (Torr et al 1979; Mount and Rottman 1980; and Rottman 1981).

The contribution of photoabsorption by interstellar H I and He I is derived from the Capella line of sight neutral hydrogen column density (1.2×10^{18} cm^2) (Dupree, Baliunas, and Shipman 1977) and the absorption cross-section (6×10^{-19} cm^2) averaged over a solar abundant ISM (Cruddace et al 1974). An optical depth of 0.72 results corresponding to an attenuation of about 50 percent of the flux. Table 1.3a summarizes the Capella and solar fluxes at earth in several of the chromospheric and TR zone lines, and the He II 304 Å flux expected from Capella based on these $6 \times 10^4 \rightarrow 5 \times 10^5$ K lines. He II 304 Å fluxes at earth in table 1.4a range from 1.4 to 2.7 ph $cm^{-2}s^{-1}$. This estimate has assumed that N(He I)=0.1N(H I) which is reasonable given the Copernicus measured temperature of 8,000 K for the H I gas. This experiment however, is the first to be sensitive to absorption in He I, and as discussed further in Chapter 5, provides evidence that N(He I) $\geq$ 0.25 N(H I). Several plausible explanations consistent with the 8,000 K temperature are considered in section 5.3.

Line emission in the XUV also arises from highly ionized species in the corona. The brightest lines are those near 195 Å of Fe XVI, formed at 10^6 K in the corona. Stern, Wang and Bowyer (1978) have performed the only calculation to date of the XUV spectrum of a hot, tenuous plasma. Their volume emissivities for XUV lines coupled with the Capella coronal emission measures of Cash et al (1981) and Holt et al (1981) are used to produce the iron line fluxes of table 1.4a.

It is important to consider the possibility that coronal and TR emission in Capella may be variable. Capella has been extensively observed by IUE in 1978 (AL 1980), 1979 and 1981 (Ayres 1982). The 1981 data consist of observations nearly every other day in the month of February and March. No variations in the intensity of the Mg II, Si II, or C IV lines between these data sets were found within the +/- five percent normalization errors of the IUE. Searches for variability on time scales from an hour to a day were also negative to within the same

Capella He II 304 Å Flux at Earth						
species	λ (Å)	T (K)	$f_{\odot}^{1}$	f_{C}^{2}	$F_C / F_{\odot}^{3}$	f_{304}^{4}
Si IV	1394	$6 \rightarrow 8 \times 10^4$	5.4	2.3	60	1.7
C IV	1549	10^5	12.6	4.4	50	1.4
N V	1240	2×10^5	1.9	1.3	90	2.7
O VI	1032	$3 \rightarrow 4 \times 10^5$	2.1	0.9	60	1.7
x-rays	100 eV→1 Kev	$3 \rightarrow 30 \times 10^6$	35.0	17.0	70	-
Capella Coronal Iron Line Flux						
-	-	-	EM	vem	-	f_{Fe}
Fe	195	1.6×10^6	4×10^{52}	1.5×10^{-13}	-	0.3

1. flux in the solar line at 1AU (10^{-2} ergs/cm^2–s)
2. Capella line flux at earth (10^{-11} ergs/cm^2–s)
3. ratio of Capella surface flux to solar (AL 1980)
4. Capella 304 Å flux (ph / cm^2–s) at earth for an ISM optical depth of 0.72

table 1.4a

errors. The XUV observation reported in this thesis was taken March 23, 1981 within the period of coverage by the IUE.

The spectrometer constructed for this observation consists of a set of nested grazing incidence imaging optics and a microchannelplate focal plane detector. Free standing diffraction gratings provide a dispersion of 46 Å per mm in the focal plane. The spectrometer resolves 0.7 mm or 32 Å. It has an effective area in first order of 0.13 cm^2. The instrument is described in detail in chapter 2. For 200 seconds of observing time with a source rate of 1.5 ph $cm^{-2}s^{-1}$ 40 counts are expected in first order. The main source of background is 304 Å photons from the sun which are resonantly scattered by He II ions in the upper atmosphere. These are expected to contribute about twenty counts to a resolution element in first order during a 200 second interval. A reasonable signal to noise ratio is expected to prevail. The earth's atmosphere is opaque to the XUV below an altitude of 170 km requiring the experiment to be carried aloft on a sounding rocket. A two stage launch vehicle obtaining an altitude of 262 km provides over 200 seconds above 200 km. The instrument and calibration are described in considerable detail in Chapter 2 and Chapter 3.

CHAPTER 2

2.1 Spectrometer System

The detection of XUV radiation relies on photoemission of electrons from a suitable cathode. The photoelectron signal is usually amplified by using an electric field to induce bombardment of a secondary emitter in a process analogous to that of a conventional photomultiplier tube. Both the single channel electron multiplier (CEM; Samson 1967, Lapson and Timothy 1976), and the channel electron multiplier array (CEMA; Wiza 1979) operate on this principle. The CEMA is an adaptation of the CEM in which many single channels are bundled together to produce a two dimensional image intensifier which converts single input photon to a 10^6 - 10^8 electron cloud at the output. Limitations to the CEMA as a spectrometer element are its lack of energy resolution and small intrinsic geometric area, less than 13 cm^2. These are overcome by situating the CEMA at the focus of a set of imaging, grazing incidence mirrors with dispersive diffraction gratings in the optical path. The spectrometer configuration selected for this work is shown in figure 2.1a. The concept was partially dictated by the availability of the grazing incidence optics which were designed and constructed for a previous flight by our group.

Radiation incident on free standing transmission gratings is diffracted and imaged by a nested set of Wolter type I x-ray mirrors (Agrawal et al 1974) onto a CEMA based focal plane camera. A thin foil, broadband filter consisting of a 1500 Å aluminum base with a 270 Å carbon overcoat is introduced to the converging beam to eliminate most of the x-ray flux short of 170 Å. It also rejects the diffuse ultraviolet background, particularly the geocoronal lines at He I 584 Å

and hydrogen lyα. The points at which the filter transmission falls to ten percent of its maximum are the aluminum L edge, 170 Å, and at 450 Å (see figure 2.1c). The mirrors have a focal length of 1275mm. The grating period is six microns with equal lines and spaces. A first order diffraction angle of 17.4 arcminutes at 304 Å results in a focal plane separation between the zero and first order images in the focal plane of 6.46 mm. Two dimensional imaging is provided by the focal plane camera with a spatial resolution of about 0.5mm (FWHM). Combined with the mirrors, this leads to a $\lambda/\Delta\lambda$ of approximately nine at 304 Å, sufficient for this experiment. The instrument was calibrated for both efficiency and spectral resolution at the National Bureau of Standards synchrotron. The subsequent paragraphs describe the spectrometer components in some detail.

X-ray Imaging Mirrors

Normal incidence reflecting optics are generally not useful below 1000 Å. Consequently much effort has been placed in the development of high resolution grazing incidence optics for use in x-ray astronomy (eg Brauninger, Lenzen, and Trumper 1978). A set of two nested Wolter type I mirrors was fabricated by the Caltech x-ray astronomy group (Agrawal et al 1974) for use in sounding rocket experiments. The Wolter type I configuration consists of an initial paraboloidal imaging surface, followed by a hyperboloid to provide correction for coma aberrations introduced by the paraboloid surface. The entrance aperture of the mirrors has a total geometric area of 211 cm^2, 37 cm^2 of which are obscured by the support structures for the inner mirror cell and the mountings for the diffraction gratings. The average angle of incidence to the nickel reflecting surface is 1.5°. The small angle of incidence allows the sensitivity of the system to

extend to about 2 KeV. Thus the mirrors are somewhat mismatched to the XUV where 75 percent reflection efficiencies extend to 8° angles of incidence. Utilization of larger angles of incidence requires Wolter type II optics to maintain a long focal length, and hence good resolution. The extreme cost and difficulty involved in mirror fabrication dictates this sacrifice of collecting area, by using the mirrors in hand.

The imaging quality of the mirrors has been measured optically under uniform illumination of the entire entrance aperture by a collimated twenty four inch diameter beam of laser light produced by a Cassegrain telescope. The optical FWHM is less than twenty arc-sec. XUV imaging can only be tested by illuminating small regions of the surface because of the difficulty in producing a large collimated beam of radiation at these wavelengths. The XUV blur was measured at the NBS synchrotron and found to be less than one arc minute (see Section 3.3).

Diffraction Gratings

The development of fine line transmission diffraction gratings has been motivated by recent astrophysical interest in high resolution x-ray spectroscopy. Free standing gratings of one thousand lines per millimeter have been produced by groups in the Netherlands for use on the Einstein (Schnopper et al 1977) and EXOSAT (Brinkman et al 1979) x-ray satellite. In both these applications the grating period is defined by the interfering of two coherent beams of light on a nickel substrate coated with a thin layer of photoresist. After developing and etching, channels corresponding to the grating lines are formed in the resist and subsequently electroplated with gold. A drawback to this interfering beam exposure technique is that the channel walls are not vertical. Maintaining

the linewidth control limits the thickness of the electroplated gold to a few tenths of a micron. The resulting gratings are extremely fragile.

In contrast, through conventional integrated circuit fabrication techniques based on exposure of resist through an image mask, it is possible to produce channels with approximate vertical profiles to a depth of about 2.5 microns. The disadvantage of this technique relative to the interference method is that linewidths are currently limited to two to three microns. A grating of six micron period has sufficient dispersion at XUV wavelength to provide better than 30 Å (FWHM) resolution when used with the Wolter type I grazing angle telescope and focal plane camera. The efficiency of a transmission grating in nth order is given by:

$$\varepsilon^n = \frac{\sin^2 (n\pi a/p)}{(n\pi)^2}$$

where p is the period and a is the open line width. The ratio a/p = 0.5 maximizes the grating efficiency in the first order, and eliminates second order contamination. Gratings with 3μ lines with a 6μ period were selected for this work. An additional superstructure of alternating 25μ and 10μ lines, each separated by 140μ, was placed perpendicular to the 3μ lines. This support wire structure was selected on the basis of vibration testing of prototype gratings at the Jet Propulsion Laboratories. Tests were carried out at atmospheric pressure and in an evacuated chamber. The payload is also pumped out to 10^{-4} torr prior to launch. The primary problem induced by vibration is a tendency for the 3μ lines to deform slightly when the support wire spacing was 280μ. Even with a 280μ spacing, no tearing or gross deformation of the gratings occurred.

The gratings were made in collaboration with the integrated circuits group at Lawrence Livermore Laboratories while a 1:1 image mask defining the grating

and support structure was generated by the NBK corporation. The mask consists of chromium lines on a quartz slide. It is proximity printed to a 2 to 3.5 micron-deep layer of photoresist spread on a 2 1/4" by 2 1/4" glass slide which has been coated with a uniform few hundred Angstrom thick layer of chromium. The chrome layer serves as a substrate for the electroplated gold. Alignment of the mask and each glass slide is maintained so that the support wires lie parallel to an edge of the glass slide. This facilitates the subsequent process of mutually aligning each of the 2 1/4" by 2 1/4" facets around the entrance aperture of the telescope. Following exposure the photoresist is etched leaving 3μ to 4μ deep channels which are filled in with electroplated gold.

The proprietary solution used for electroplating was developed to minimize internal stresses in the gold structure arising from the deposition process. Though their origins are not well understood these stresses can cause a very fine wire grid to distort when released from the supporting substrate. All gratings were thoroughly examined by using an optical microscope for such distortion. The channel profiles are slightly wider at the top than bottom as a result of lateral etching of unexposed resist. Thus, the deeper the gold is deposited the wider the lines tend to be. Because precise control of the electroplating thickness is difficult, linewidths of the flight gratings generally vary from 3.0 to 3.2 microns, with some of the early prototype gratings possibly having up to 3.5μ lines. Also, the only direct methods of determining the linewidth are electron microscopy and XUV measurements of the relative efficiencies in each spectral order. Electron microscopy was performed on one of the flight gratings showing a linewidth of 3.0 +/- 0.05μ. A prototype grating was used for calibration at the National Bureau of Standards and was found to have a linewidth of 3.5μ from the relative efficiencies in zero order, first order, and second order. This NBS grating was not electron-micrographed because it would have been destroyed while

being mounted to the specimen table. The discrepancy in linewidth between the prototype and flight grating was caused by the 3μ to 3.5μ depth of gold electroplated in the prototypes. The flight gratings were made two to three microns deep. The period of the grating is easily checked by measuring the first order diffraction angle of He-Ne laser (6328 Å) beam passing through the grating: it is 6μ +/- 0.05μ.

Following electroplating the unexposed resist is removed, along with the chrome which has not been plated with gold. The gratings remain fixed to the glass slide. Each grating segment must be aligned and mounted to one of the 24 trapezoidal brass facets which fill the entrance aperture of the telescope. The diffraction axis is defined by a rigid bar suspended over a table fixed to a dividing head. The bar can slide across the table but remains parallel to the diffraction axis. Each brass facet is aligned to this axis, then rotated to the angle at which it will mount on the mirror cell. The glass slide with the grating is then oriented over the facet by the bar and secured to the brass frame with lapidary wax. Alignment is good to better than 0.5 degrees. The brass frame with glass attached is then bathed in concentrated hydrofluoric acid to etch the glass from the gold, leaving a free standing grating. An ultrasonic cleaner was also used to assist in removing the glass.

Focal Plane Camera

The focal plane detection system incorporates a CEMA, in conjunction with a resistive disk readout (Lampton and Paresce 1974) to convert the electron cloud output of the CEMA to a digital two dimension coordinate (figure 2.1c). The CEMA (Wiza 1979) is a forty millimeter diameter bundle of microscopic (38μ diameter), extruded lead glass tubes, each functioning independently as an

amplification device. A single tube is two millimeters long and biased by a 1100V potential - photons intercepting a tube entrance may produce a photoelectron. Emitted electrons are accelerated by the local electric field until colliding with the channel wall, where typically two secondaries are produced. The subsequent avalanche generates gains of $10^3 \rightarrow 10^4$ Two CEMA's were obtained from the Galileo Electro-Optics Corporation and cascaded to produce a gain of 3×10^7. The space charge density of the electron avalanche ultimately limits the gain to approximately 10^8. The plates also produce occasional spurious pulses. These avalanches are initiated either by electrons thermally emitted from the top of the channel walls, or by ions formed in the ambient vacuum which accelerate up the channel potential until colliding with the walls releasing an electron which begins a cascade. The first internal background source is an inherent, unavoidable feature of the plate and typically produces one to two counts/cm^2–s. The ion feedback problem is reduced by introduction of a 16° angle between the channels of the input and output plates as indicated in figure 2.1b. The channels of the input plate are parallel to the optic axis while those of the output plate are at 16° to the axis. Single ions feeding up the channels have difficulty circumventing the discontinuity in angle. Ion feedback is also reduced by maintaining a high quality ambient vacuum, preferably in the 10^{-8} torr range. Laboratory internal background rates were 3.5 counts/cm^2–s over a vacuum range of 10^{-5} to 3×10^{-7} torr. The rate obtained from the flight data was 3.3 counts per second (see section 4.2).

The sensitivity of the detector depends primarily on the photoemission efficiency of the input surface. Although the base material of the CEMA, lead glass, is responsive to XUV photons, considerable enhancements can be achieved by evaporating a suitable photocathode such as MgF_2, LiF or CsI on the surface of the input plate. (Lukirskii et al 1964; Lapson and Timothy 1976; Macau, Jamar,

and Gardier 1976). MgF_2 provides a factor of about two in improvement in XUV efficiency, while CsI may provide as much as five times the efficiency of the untreated plate. Materials other than M_gF_2 tend to be chemically unstable and require extensive care to achieve shelf lines greater than one year. A 1200 Å layer of MgF_2 was chosen as the primary photocathode. The efficiency is expected to be about five percent (Mack, Bowyer, and Paresce 1976). In the near future the CEMA will undergo several considerable improvements. Curved channels 5 to 10 mm long, providing comparable gains to the cascaded plate configuration, but much lower internal backgrounds, will become prevalent. Furthermore, the x-ray astronomy group at the University of California at Berkeley has been able to stabilize a CsI cathode CEMA for over a year, reporting a forty percent quantum efficiency (Roger Taylor priv. communication 1982). In present plates the tube packing leaves about forty percent of the input surface inactive. Chemical etching to produce funnel shaped entrances to the tubes will allow an increase in active areas.

The CEMA converts an interacting photon to an electron cloud emitted from the core of a single microchannel. Various techniques have been developed to locate the centroid of the emergent cloud. These include:

1. Crossed wire grids (Kellogg et al 1976) as utilized by the Einstein satellite's high resolution image (HRI);

2. phosphor screens which convert the electrons to optical photons which are imaged by photodiode arrays (Wiza 1979); and

3. two dimensional, thick film, resistive disks which collect the electron pulse and are read out by risetime sensing or charge division (Lampton and Paresce 1974).

Though all three methods have the capacity to produce resolution better than 0.1 millimeters (the Einstein HRI resolves $\sim 15\mu$), the resistive disc technique is particularly convenient to implement because of the simplicity of the mechanical structure and signal processing electronics (see below). The disc is constructed on a fifty millimeter diameter piece of *MACOR*^{TM} machinable ceramic which is an insulator. A layer of resistive ink is applied to the surface of the disk. The ink was obtained from Engelhard, and has a nominal resistivity of 10^5 $\Omega/[]$. Deposition of the ink is accomplished by a conventional screening process. The MACOR disc is mounted in a vacuum chuck, parallel to and about 0.020" beneath a 230 line/inch, 0.0014" diameter wire taut stainless steel mesh obtained from the Microcircuit Engineering Corporation. The mesh area is approximately eight inches by eight inches, however all but a fifty millimeter diameter hole in the center is masked. The ink is placed on the top of the mask at the edge of the hole, and a squeegee is used to spread it over the central exposed mesh, printing the ink. The thickness of the film, hence its resistivity, and its uniformity depend crucially on the pressure, attack angle, and draw rate of the squeegee, as well as on the mesh dimensions. Considerable experimenting with the parameters was necessary to generate a quality flight disk. The applied layer of ink has a finite viscosity for several hours after application, until the solvent evaporates. This slow flow of the ink compensates somewhat for non-uniformities introduced in the screening process. When the solvent has dried the disc is fired at 850° producing an extremely durable surface. In a nearly identical procedure, four electrical contacts of silver-palladium conductive inks are screened to the edges of the disk, separated by 90°. The resistivities of the discs were found to be about 90 $k\Omega/[]$ with the four point technique of Stevens (1974).

An orthogonal coordinate system is established by taking the ratio of charge collected at two adjacent contacts to the total charge collected. If A, B, C, and D denote the charge collected at each of the contacts labeled in a clockwise fashion, the x and y coordinates are defined by:

$$x = \frac{A+B}{A+B+C+D}, \qquad y = \frac{B+C}{A+B+C+D}$$

The ratios are performed by low noise, discrete component, logarithmic and summing amplifiers. The processing electronics were developed for similar XUV astronomy applications at the Space Science Laboratory of the University of California at Berkeley. They are marketed commercially and were obtained from Surface Science Devices. The design minimizes component heating and power consumption as the payload is not pressurized and has a limited battery supply.

In addition to the 0-5 V x and y position pulses, the total charge output, A+B+C+D, is also available on a 0-5V scale with 5 V equivalent to a gain of 1.5×10^7. A threshold discrimination generates a TTL level strobe pulse when the gain exceeds 1×10^6, corresponding to a output of about 0.3 volts. This threshold rejects power supply ripple and low level background pulses. The pulse distribution is centered close to 2.5 volts with a FWHM of 120 percent. The electronic deadtime of the analog signal processing is less than $8\mu s$.

Position signals accompanied by a strobe pulse are digitized by a ten bit successive approximation A to D converter, of which the eight most significant bits are retained. $35\mu s$ of dead time are introduced to the conversion process. Linearity of the entire camera system was tested using a highly collimated x-ray beam mounted on an x-y table moving under micrometer control. The smallest resolution element is 0.2 millimeters. Within a ten millimeter radius of detector center the apparent position of the source does not deviate by more than 0.1

millimeters from the real position. At 16 mm the linearity is about 0.2 millimeters, after which it very rapidly degenerates. For a point source targeted at detector center the region out to ten millimeters includes wavelengths in first order up to 460 Å. The point response of the camera is 0.6 millimeters FWHM.

Figure 2.1a - The primary components of the scientific instrument are shown. Radiation incident on the diffraction gratings is imaged by two nested Wolter type I grazing incidence telescopes onto a channel electron multiplier array situated in the focal plane. A bandpass filter is placed in the converging beam to remove the geocoronal background from the solar He I line at 584 Å which is resonantly scattered by He I in the upper atmosphere, as well as the H Lyα background. Guidance is provided by a star tracker on the mirror cell coupled with gas jets below the experimenter's section. Aspect verification is performed by a Nikon camera mounted in the mirror cell.

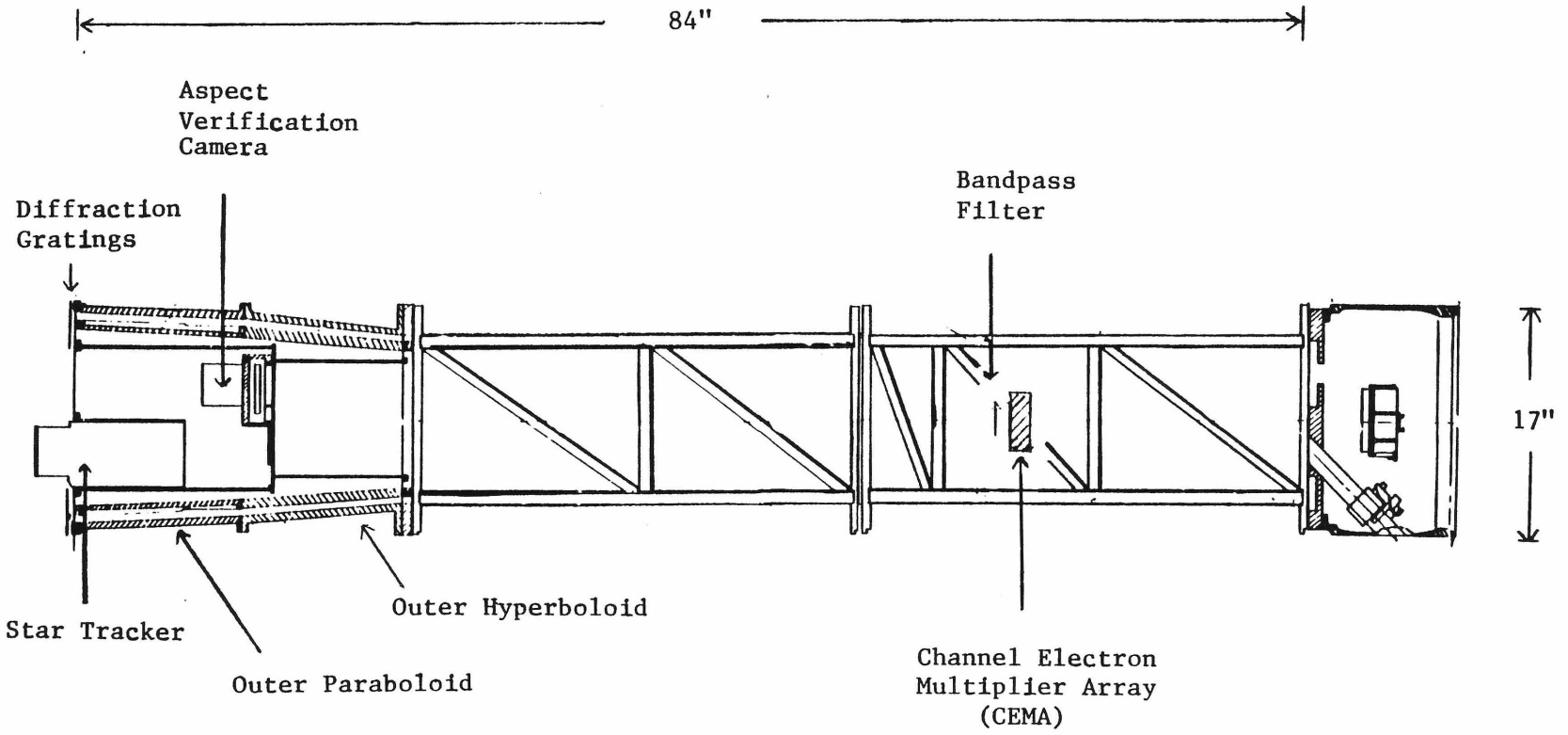

INSTRUMENT SCHEMATIC

figure 2.1a

Figure 2.1b - The response of the bandpass filter to XUV radiation is shown. The sharp edge at 170 Å is caused by the L absorption edge in Al while the decrease in transmission at longer wavelengths is primarily caused by the 270 Å layer of carbon.

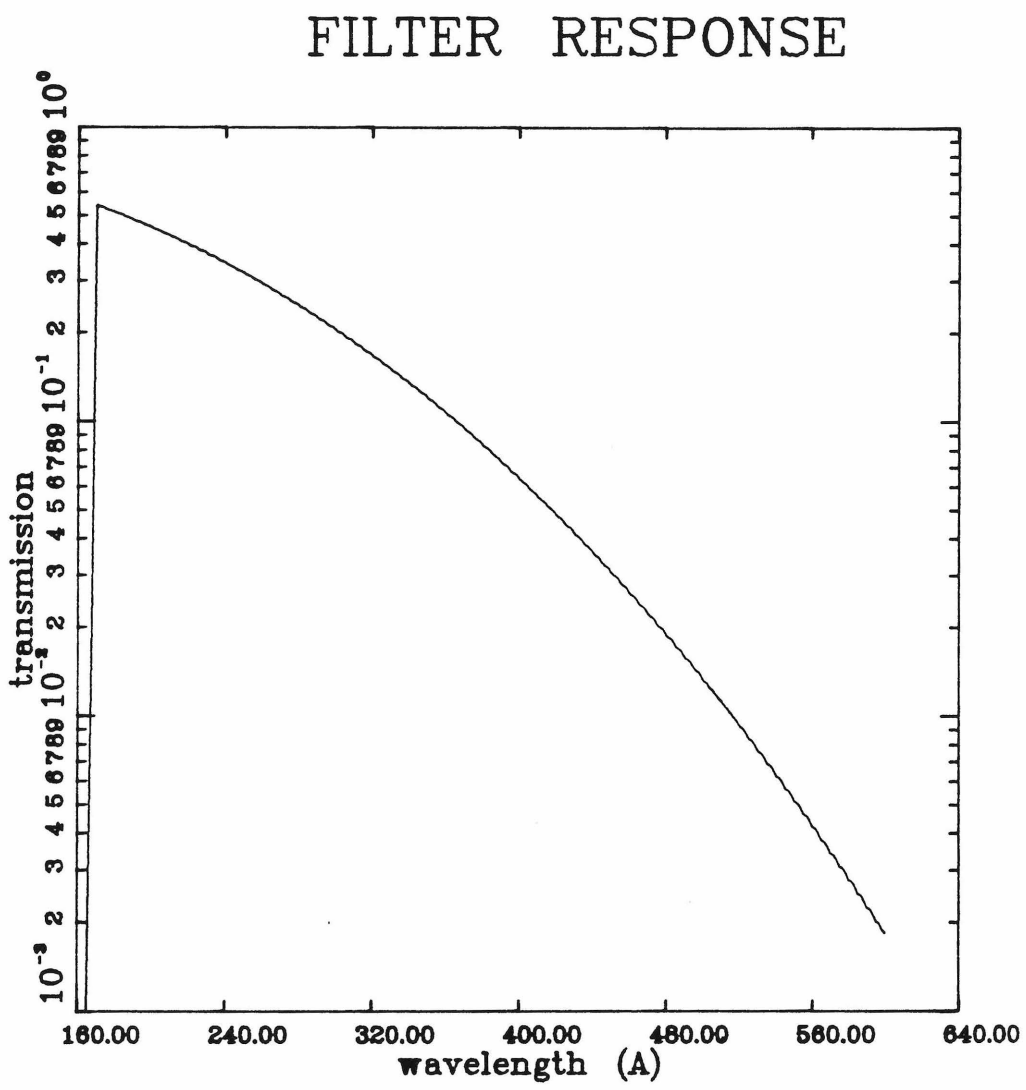
FILTER RESPONSE
transmission
10^{-3} 2 3 4 5 6 7 8 9 10^{-2} 2 3 4 5 6 7 8 9 10^{-1} 2 3 4 5 6 7 8 9 10^{0}
160.00
240.00
320.00
400.00
480.00
560.00
640.00
wavelength (A)

figure 2.1b

Figure 2.1c - The focal plane camera, bandpass filter and resistive readout are shown. The channels of the input CEMA are parallel to the optic axis, while those of the second plate are cut at 16°. This discontinuity in angle reduces the ion feedback internal background as described in the text. A brief summary of the x,y coordinate signal processing is also given.

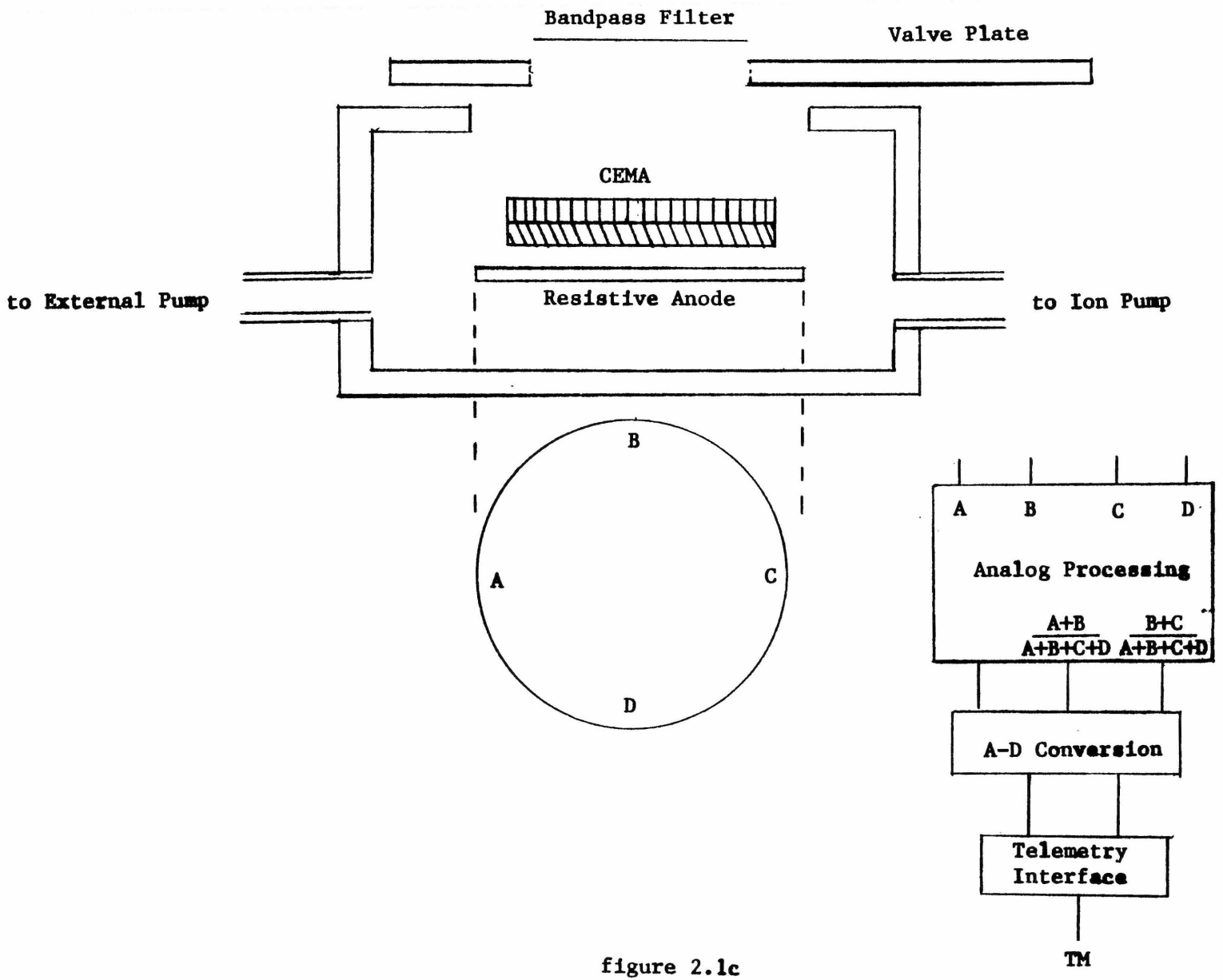
Bandpass Filter
Valve Plate
CEMA
to External Pump
Resistive Anode
to Ion Pump
B
A
C
D
A
B
C
D
Analog Processing
A+B
A+B+C+D
B+C
A+B+C+D
A-D Conversion
Telemetry
Interface
TM

figure 2.1c

2.2 Spectrometer Support Functions

The spectrometer support systems are comprised of functions essential to flight performance, and those assisting ground operation. Primary members of the former category are:

- the attitude control system (ACS);
- the aspect verification camera and fiducials;
- the telemetry system (TM); and
- the payload control, monitoring, and power electronics.

Ground support equipment developed for this payload includes a very flexible telemetry emulator used in debugging the flight TM interfacing, as well as a microcomputer based data acquisition system to allow storage of calibration data on nine track tape and assist in the instrument diagnostics.

Attitude Control System and Aspect Verification System

The Goddard Space Flight Center (hereafter GSFC) provides a Strap III gas jet guidance system for spectrometer pointing control. A Ball Brothers image tube mounted on the front flange of the mirror cell constitutes the primary component of the tracking system. Absolute pointing is good to within 5 arc-min and the jitter cycle is only a few arc-secs. Alignment of the attitude control system (hereafter ACS) was carried out at GSFC during payload integration and at the White Sands Missile Range prior to flight. A point "star" generated by a Cassegrain telescope is imaged by the Wolter optics to a 0.003" aperture situated in front of a photodiode located in the geometric center of the focal plane camera. The tracker also images this star and is set to orient the spectrometer so that Capella is placed in the geometric center of the field of view.

The aspect verification system utilizes a Nikon camera with an 85mm lens and power winder to take photographs of the star field during flight. Fiducial marks are generated at the edges of the field by a Litronix LED array. Calibration of the pointing verification camera is concurrent with the ACS alignment. When the laboratory "star" is set to the geometric center of the focal plane camera, the Nikon takes several photographs. The position of the calibration source relative to the fiducials defines the location on the sky of the center of the field of view. Comparison with the flight star field photos enables determination of the Capella aspect to a 2.7 arc-min error box.

Telemetry

Real time telemetry relays the payload data to ground receiving stations during flight. The telemetry format provides a time ordered sampling of the experimenter's data lines which is repeated forty times a second. Analog and digital data as well as pulsed signals which must be scaled, may be passed to the telemetry. Analog data are converted to digital by the encoder prior to transmission. A thorough description of the telemetry capabilities and interfacing requirements is given by Acuna et al (1979). Each data line is sampled for 50μs and the data present at the end of this period are latched by the telemetry system. The repeated format, a mainframe, consists of 512 50μs periods, 64 of which are committed to use by GSFC for timing and synchronization. The 512 sampling periods which constitute a mainframe are subdivided into thirty-two subframes of sixteen time slots each. The experimenter may have a particular data line sampled once in each subframe (subcommutation), so that it is recorded 40 × 32= 1280 times per second. A given data line may also be sampled more than once in each subframe (supercommutation). Both super- and

subcommutation were utilized in this flight. The telemetry section provides the experimenter with its mainframe clock (40 Hz) and sampling clock (20 kHz) from which the code indicating which line is being sampled at a given time is regenerated. This is useful in passing data between the experiment electronics and the TM. Two telemetry encoders and downlinks are provided with each rocket for a total 1024 independent data channels. This experiment required less than 200 channels so the second TM served as a redundant link.

Spectrometer Electrical Subsystems

A primary task of the spectrometer support electronics is to convert the output of the CEMA to digital event coordinates which can be passed to the real time telemetry for ground transfer. Signal processing up to the A-D conversion of the x and y coordinates has been outlined in section 2.1. Events occur asynchronously, while the telemetry provides synchronous sampling of the data. The TM interface was designed around a first in - first out buffer memory (FIFO) which accepts events from the MCP camera and passes them to the TM section. The FIFO can hold up to eight events before a readout to the telemetry is necessary and hence would be useful in strong source applications. This feature was not essential to this flight. The write pointer of the FIFO is incremented by the event strobe and the read pointer is incremented by a handshake from the TM when the x and y data lines have been sampled. Both counters reset to zero when seven is reached. The FIFO was designed for resiliency against potential glitches and rf noise on the read and write lines, however a rocket payload is a moderately noise free environment. The event strobe is also passed to a scaler line from the TM and provides the total event rates as a function of time.

Experiment power is provided by two battery packs which demonstrated a 30% reserve capacity in pre-flight simulations. Analog and digital grounds are isolated, as is the ground to the aspect camera control board since camera firing is a potential source of noise. No glitching on any of the power lines was noted when the camera shutter was driven. High voltage for the CEMA is supplied by a Venus sure start DC-DC converter designed for high altitude operation. The output voltage is feedback stabilized and output ripple is not sufficient to interfere with the analog event processing circuitry. Timing signals which initiate payload functions are produced by a redundant system of mechanical Haydon timers which pass signals to relays in the experimenter's section.

Flight performance of the hardware is provided by monitors of the battery and regulator voltages and currents, the MCP voltage, camera and led switching, and numerous other housekeeping functions.

Ground Support Equipment

The two central hardware systems constructed were the TM emulator encoder and decoder, and a microcomputer based data acquisition system. The emulator performs the identical function of the flight unit and is used primarily to debug the experiment electronics before integration with the flight system at GSFC. The encoder portion takes the payload data lines, samples them in the same format as requested for flight operation, and converts them to an eight bit wide serial data stream. The decoder emulates the flight ground station and receives a serial 8 bit data stream from which it extracts the payload data. It is used during integration to verify that the data encoded and transmitted by the flight TM package is properly placed on the data bus. By using EPROMs to decode the telemetry clock the device is programmable to handle any TM

format. A display monitor was integrated with the decom unit to provide both real time displays of the focal plane events and displays originating from the supporting computer.

A microcomputer was constructed to facilitate system debugging, and provide a realtime data analysis and record storage system. The machine employed a Z-80 CPU and interfaces were constructed to a nine-track Kennedy tape drive, a CRT, and the decommutator. A monitor and control basic programming language were obtained from Cromemco to assist in software development. The I-O drivers were written in Z-80 machine language subroutines which were called by the basic. I-O transfer was allowed both on a polling and priority interrupt basis. Data written to the Kennedy could be transferred to the VAX for detailed analysis. Frequently used software was downloaded from the VAX to a EPROM programmer for permanent storage. The entire ground support system proved to be both extremely reliable and exhibited great flexibility when changes in operation were required.

CHAPTER 3

3.1 Introduction

The XUV portion of the spectrum has only recently been opened to study for radiometry and spectroscopy. Consequently the responses of photodetectors and, reflecting and transmitting surfaces to this radiation are not well documented in the literature. Inconsistencies in published results make it impossible to safely estimate spectrometer performance on the basis of measurements done on similar instruments. Compounding this difficulty is the possible presence of contaminants on the instrument's optical surfaces. Ubiquitous hydrocarbons are strong attenuators of XUV radiation. A 25 Å hydrocarbon layer on the mirrors will cause a loss in reflection of about 20 % of the incident photons. The mirror system was originally designed for x-ray imaging where the absorption of these molecules is not a critical concern and the mirrors had been used in oil based vacuum systems.

The angular response of the instrument is a basic factor in limiting the spectrometer wavelength and sensitivity to source line emission. In this work the angular response refers to the spot size realized in the final digital focal plane image by a hypothetical point source situated at infinity. This instrument blur is determined by the aberrations in the mirror imaging system, and degradations introduced by the finite spatial resolution of the focal plane camera. Incorrect location of the focal plane will also increase the net image blur. Spot size is generally cited in millimeters of diameter in the focal plane, or the equivalent angular diameter obtained from the 1280mm focal length (1mm ~ 2.7 arc-min). Grating dispersion and angular resolution also combine to define the

wavelength resolution. At 304 Å the grating produces a 17.4 arc-min diffraction angle in first order. For a blur circle of 2 arc-min FWHM the wavelength resolution will be 35 Å at 300 Å for a point source. Clearly, the counting statistics of the source also play a role in the spectral resolving power. The prominent XUV lines anticipated from Capella are well separated in wavelength (Stern, Wang, and Bowyer 1978) and resolution better than 40 Å is sufficient for this observation.

The nonsource background contribution to a narrow line also has a strong influence on the quality of the system sensitivity. Since the diffuse geocoronal radiation and the CEMA internal background produce a constant density of counts per area in the focal plane the background contamination in a line is proportional to the blur. In the case where a strong source continuum is present, grating dispersion also becomes a factor in the sensitivity to line emission, however this situation is not relevant to the Capella spectrum. The point response of the mirrors was measured during their inaugural flight and found to be quite poor, about 4-5 arc-min FWHM. The attributing of the poor response function to the mirrors rested on the assumptions that the focal plane was properly located, and that the detector position response (a proportional counter was the focal plane instrument) was well known. From the data obtained at the NBS we find that the mirror blur is less than 1 arc-min FWHM (see section 3.3).

Calibration is also useful in proving the integrity of the system design and hardware functions by operation under flight configuration. In the course of the calibration it was realized that the absolute efficiency of the spectrometer was substantially lower than expected. The problem was traced to the CEMA which was replaced prior to flight. The flight plate was calibrated with respect to the NBS plate prior to flight.

Addressing these issues requires an XUV source whose spectrum and normalization are known. In addition the source should be pointlike, and collimated to a divergence significantly less than the angular response of the spectrometer The physical size of the payload also demands that a very large high vacuum system be incorporated in the calibration facility. There are only two U.S. facilities meeting these specifications. One is at the Space Science Laboratories of the University of California at Berkeley. The other is the National Bureau of Standards (NBS) SURF II electron synchrotron in Gaithersburg, Maryland. The NBS synchrotron was the primary facility used in this work. The details of the ring immediately relevant to our interfacing and calibration are summarized in the next section. A more complete description can be found in **A User Guide to SURF** (Ederer and Ebner 1975).

3.2 THE SURF II FACILITY

Surf II is an electron synchrotron storage ring dedicated to the production of XUV radiation for spectroscopy, radiometry, and surface science. Three ultraviolet beamlines originate from ring tangent points to extract photons. Two of these lines are equipped with monochromators calibrated against a double ionization chamber for applications where a standardized source of monochromatic radiation is desired. A third beam transport line contains no optical components other than collimators, and is designed to serve as a spectrometer calibration facility. Flux in the beam is calculated from the storage ring parameters and beam current. This line and its accompanying vacuum chamber were minimally completed in January 1981 and we were its first users. Fig 3.2a shows the physical layout of the storage ring and the beam line.

A microtron injects electron bunches into the main ring at an energy of 10 MEV. Two r.f. cavities drive the circulating energy of the electrons to 240 MEV. Following acceleration the cavities continue to provide energy to the beam to compensate for radiative losses. The stability of the beam energy is a critical factor in maintaining a constant flux for calibration purposes. It is held at 240 MeV to better than 0.1%. A 0.1% change in energy alters the XUV flux by less than 1% (Ederer and Ebner 1975). Electrons cycle in two bunches 180 ° apart until their mutual coulomb interactions and scattering by the residual gas in the 10^{-10} torr vacuum removes them from the beam. This decay time is several hours at the operating currents used in our calibration. The ring current at injection is usually greater than 1 milliamp (mA). The high sensitivity of our instrument requires the beam current to be a factor of 10^6 less than this normal operating level to avoid rate induced gain loss in the CEMA and dead time effects. Due to the large natural collimation of relativistic synchrotron radiation (the half cone angle $\delta = \frac{M_0c^2}{E} \sim$ 2mrad at 240 MeV) it is difficult to attenuate

the flux simply by decreasing the solid angle. The very small aperture required for collimation creates a significant beam diffraction, interfering with the ability to determine the angular response function. Suitably low flux was achieved by manipulating the ring fields to induce dropout of electrons until currents were at the nano-Amp level. The large angular flux gradient requires that the beam defining apertures be accurately positioned in the orbital plane to avoid systematic errors in flux determination. Positioning is done to better than an arcsec using the optical plane locator described in the **USERS GUIDE**. The largest emission angle accepted by our beam is 0.05 mrad which lies well within the angular distribution plateau near 0 °. A further characteristic of synchrotron radiation is its intrinsic polarization in the orbital plane. Gratings exhibit strong polarization effects in the diffracted intensities in various orders when the wavelength of incident radiation is of the order of the grating period. At 304 Å the wavelength is a small fraction of the grating period hence no discernible effects were anticipated. One data set was taken in a state of polarization orthogonal to that of the other sets and no changes were noted.

Figure 3.2b shows the wavelength spectrum of SURF II accepted by our experiment as calculated by the NBS (Huey 1981 priv. comm). At 240 MeV peak intensity is near 180 Å, and emission falls off steeply below 100 Å. Errors in the calibration depend on the accuracy with which the spectral flux density and its temporal features are determined. For the direct beam used in our calibration the spectral flux density per electron can be reliably calculated as a function of the orbital parameters electron energy (E), and orbital radius (R). A principal concern in the design of SURF II was the minimization of uncertainty in E and R, and errors in spectral flux density per electron are less than 5% for wavelengths between 100 Å and 600 Å (Ederer and Ebner 1975). The total flux reaching the instrument is the product of the single electron spectrum with the number of

electrons in the ring. An additional uncertainty arises from the error in ring current determination and is typically three percent at the normal operating levels of a few milliAmps. For this work current monitoring was done by a direct electron counting system under development at the NBS (Saloman 1980). This technique, although presently limited in dynamic range, can be used at the very low ring currents employed for this calibration. A photomultiplier monitors the step decrease in radiative emission from the ring which occurs each time an electron exits the stored beam. Steps are counted down to zero flux and the time at which each step occurs is recorded. In this method the ring current is precisely known as a function of time.

The beamline is windowless because of the large, unpredictable attenuation caused by matter at these wavelengths. This forces the experimenter to maintain compatibility with the ultra high vacuum of the storage ring. A limited differential pumping capacity exists on the beam pipe but the full design capacity had not been achieved pending the installation of cold traps and cryopumps. In an attempt to reduce payload outgassing the entire experiment, with the exception of the mirrors, was sandblasted and washed in acetone, alcohol, and Freon and non-essential electronics were removed. Despite these efforts the lowest vacuum achieved in the payload chamber was 3×10^{-6} torr, too low to allow direct connection to the ring. A temporary remedy was made by insertion of the XUV bandpass filter in the beam transport pipe as a crude vacuum window. Data taking time was severly limited by leakage of hydrocarbons through the filter mount.

The payload mounts on a gimbal inside a large ($8 \times 4 \times 4$ feet) vacuum chamber. The gimbal rotates about two orthogonal axes allowing the angle between the beam and the instrument's optic axis to be varied. In particular the optic axis can be oriented parallel to the incident beam. Movement of the

gimbal is controlled by stepper motors in the tank, which are connected to an external computer. Variations in the angle of incidence of the beam change the point of intersection of the beam with the focal plane. This allows selection of the portion of the CEMA used in imaging the diffraction pattern. Motions of the instrument in the horizontal and vertical are accomplished by a hydraulic system which very accurately translates the entire tank. Adjustments in absolute positioning permit data to be taken at different locations on the mirrors and gratings. This feature is useful in assessing the extent of spatial inhomogeneities in the spectrometer elements.

Only one grating facet was available at the time of calibration. Extrapolation of the calibration results from this grating to the subsequent flight gratings is discussed in section 3.3. The grating used at NBS has a unique mounting location on the front of the mirror cell. The same beam polarization to payload orientation was maintained in all but one of the data sets. In this usual orientation the polarization vector of the incident radiation makes an angle of 75° with respect to the support wire structure of the gratings. After passing through the grating, radiation intercepts the mirror surface with the polarization vector approximately perpendicular to the plane of incidence. One data set was taken with the payload rotated through 90° so that the polarization was along the grating support wires and in the plane of incidence to the mirrors.

When the beam intersects the grating it has a diameter of about three millimeters. This is sufficiently narrow that it falls entirely within the acceptance area of the mirrors. There is no direct way of knowing the precise point at which the beam is striking the grating. The combined capabilities of the online data system to provide real time images and the computer control of the spectrometer orientation, made it possible to scan across the gratings and approximately center the beam on the grating. We are confident that there are no systematic

effects arising from the beam scraping the mirror or grating support structures. The angle between the beam and optic axis is also known from the position of the beam in the focal plane. The beam is situated in the center of the CEMA during most of the data taking since it is the objective of the attitude control system to target Capella there.

A data set acquired during a run consists of a two dimensional (counts as a function of x and y) histogram of the focal plane counts. Each histogram is based on 16,000 events. The x and y coordinates of each event are recorded on nine track tape by the online computer. The time at which a data set is taken is also noted so that the normalization can be determined from the direct electron counting system. A data set typically takes 200 seconds to complete. Variations in the flux levels during the taking of a data set due to beam decay are insignificant.

In addition to obtaining normalized histograms the online data system has the flexibility of performing a rough estimate of the spectrometer performance. This capability was used during the second day of running when it was felt that the instrument efficiency might be appreciably lower than expected. This assumption was verified and eventually led to isolation of the CEMA as the source of the problem. This situation is described in the following section.

Figure 3.2a - The SURF II Synchrotron facility presently consists of three beamlines. Beam line two has no optical elements and is 17 meters in length. It is connected to a large vacuum facility for calibration of spectrometer systems. Beam line three contains the direct electron current monitor described in the text.

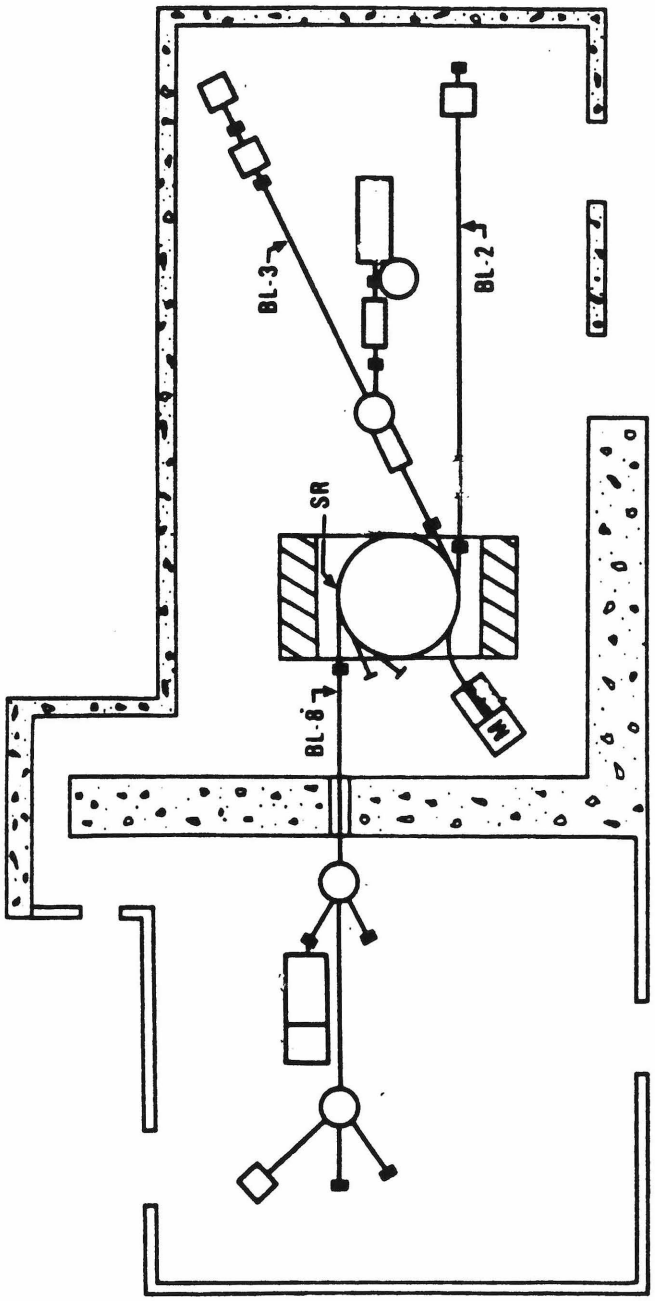

M - Microtron

BL - Beam Line

SR - Storage Ring

figure 3.2a

Figure 3.2b - The flux per second per electron in the storage ring in a one Å bandpass is displayed on the vertical axis as a function of wavelength. The number of electrons in the ring is known precisely as a result of the direct electron counting scheme.

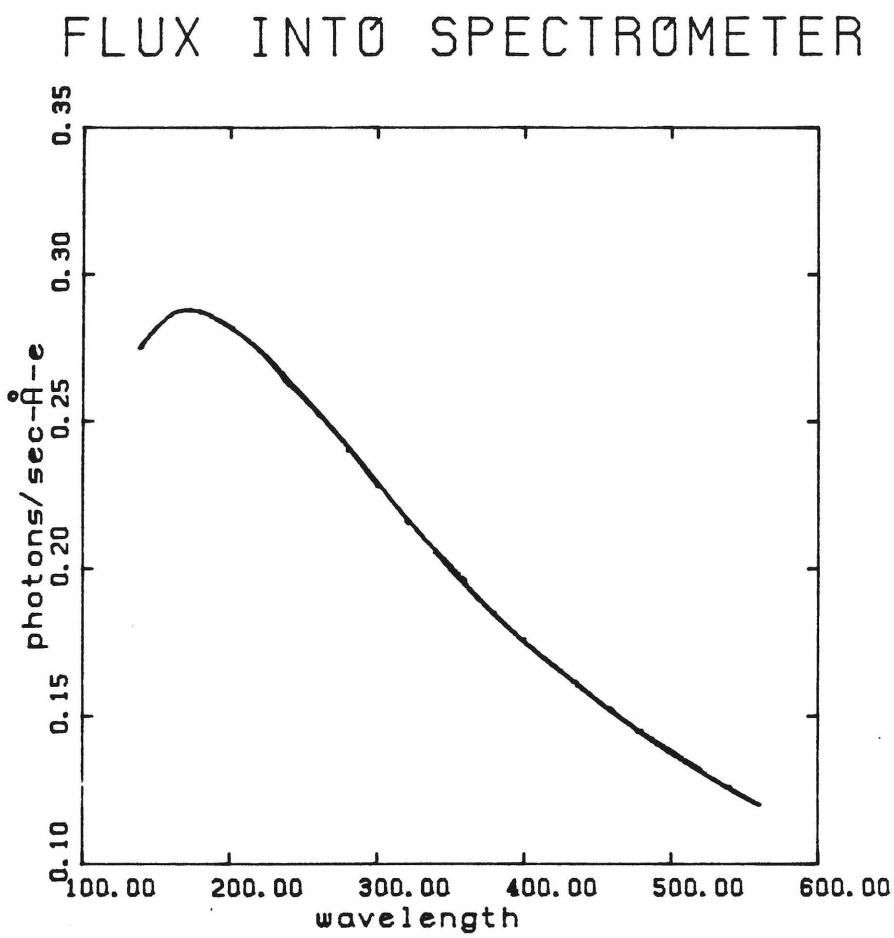
FLUX INTØ SPECTRØMETER
photons/sec-Å-e
0.10
0.15
0.20
0.25
0.30
0.35
100.00
200.00
300.00
400.00
500.00
600.00
wavelength

figure 3.2b

3.3 Efficiency Loss in the NBS CEMA; The Flight Plate

During the calibration runs it was noted that the spectrometer count rates were considerably lower than the estimates derived from the initial design parameters. The primary source of the problem was found to lie with the micro-channel plate which suffered from a combination of low photoefficiency and gain loss. Consequently this plate was replaced by a new CEMA after the NBS calibration, and prior to flight. The efficiency of the new plate was measured relative to that of the old plate using the XUV facility at Berkeley. Incorporation of the new plate into the spectrometer scales up the absolute spectrometer efficiencies derived from the NBS data by a large amount but has no effect on the angular resolution function or on the relative efficiencies of the instrument into the zero, first, and second diffracted orders.

This section reviews main aspects of the detection of the problem with the CEMA and the calibration at Berkeley of the replacement flight plate relative to the NBS plate. Section 3.4 covers the results of the detailed analysis of the NBS data.

The spectrometer efficiency was estimated with the beam incident on the inner mirror cell. The method of estimation is coarsely reproduced here to introduce the reader to the calibration effort. The expected total focal plane count rate (ie. summed over all orders of diffraction) was approximated and compared with the observed rate. In coarse fashion the expected counts are given by:

$$C = \int_{170\text{Å}}^{450\text{Å}} d\lambda \, F(\lambda) \, T_f(\lambda) \, \varepsilon_{CEMA} \, \varepsilon_{mir} \, t_g$$

Where:

$F(\lambda)$ is the synchrotron flux (see figure 3.2b)

$T(\lambda)$ is the filter transmission (see figure 2.1b)

$\varepsilon(\lambda)_{CEMA}$ is the CEMA efficiency ($\simeq$0.05)

ε_{mir} is the mirror reflectance ($\simeq$0.70)

t_g is the grating transmission ($\simeq$0.42)

The total intensity is given by:

$$F_{total} = \int_{170\text{Å}}^{450\text{Å}} d\lambda\, F(\lambda) \simeq F(300\text{Å})\,(300\text{Å})$$

Approximating the integral for C leads to:

$$C \simeq F_{total}\, T(300\text{Å})(0.4)\,(0.7)\,(0.05)$$

The expression for the efficiency is then:

$$\varepsilon = C / F_{total} \simeq 3 \times 10^{-3}$$

The efficiency is estimated from the data of figure 3.4a. There are about 4,000 counts in the spectrum which took 200 seconds to accumulate with 2,000 electrons in the ring. Figure 3.2b gives the mean flux at 300 Å, 0.22 ph $s^{-1}Å^{-1}e^{-1}$ which gives 66 ph $s^{-1}e^{-1}$ in a 300 Å bandpass. This gives and efficiency of $\simeq 2\times10^{-4}$ which is a factor of 15 below the predicted efficiency. Despite the coarseness of this estimate the factor of 15 is a significant discrepancy. The next step was isolation of the problem. Though facilities exist at the NBS to disassemble the payload and perform an individual calibration on each independent element this would have required a formidable commitment of time and money..

For several reasons the CEMA was suspect. It was apparent in the real time images that the response of the plate varied with position, particularly in the region near the ion pump port. The constant bombardment of the plate in this region by electrons of 1->3 KeV liberated by the ion pump was a possible cause of this deficiency. Visual observations of the MgF_2 coating raised questions concerning the uniformity with which the layer was coated on the photocathode. Finally small increases in the operating bias voltage produced breakdowns at the CEMA surface and very large internal background rates.

The channel plate was replaced in the focal plane by a calibrated photoemitter which would also measure total flux rates. Tungsten photoemission has been extensively studied at the NBS (Saloman 1978, Saloman 1980). We were provided with a circular piece whose photo-emission efficiency (the number of electrons liberated per incident photon) was calibrated to a few percent in the XUV. It is mounted in a paraffin holder surrounded by a cylindrical anode. Figure 3.3a shows the device's photo-electric efficiency, the mounting method, and the measurement circuitry. The tungsten cathode was located about one inch in front of the CEMA. Its diameter is large enough to accept the entire converging beam from the mirrors. The cathode current was monitored by a pico-ammeter. The anode current is an unreliable indicator of the current since not all emitted electrons are collected. The storage ring current was increased to about three milliAmps in order to produce a measurable photo-current from the tungsten.

The predicted output is calculated in the same approximation as it was for the CEMA with the response of figure 3.3a substituted for that of the CEMA. This prediction of eight pico-Amps compared favorably with the measured value of four, conclusively demonstrating that the CEMA was the main contributor to the reduced spectrometer sensitivity. Because of the nature of the approximations the remaining factor of two was not considered important.

Immediately prior to flight a new input plate was obtained and had to be calibrated relative to the NBS plate We were unable to remain at the NBS for this effort because of the pressing need to integrate at Goddard to meet the launch date, and the increasing problem of hydrocarbon leakage through the XUV shield into the main ring. Consequently this new measurement was performed with the facility at the Berkeley Space Science Laboratories (hereafter SSL).

At the SSL a monochromatic XUV beam is derived from a Perkin-Elmer grating monochrometer fed by a hollow cathode discharge source (Paresce, Kumar, and Bowyer 1971). Line spectra of the gas flowing through the discharge region are produced. In particular the He I and He II line spectra are formed in this source. The collimated beam enters a large vacuum tank where the channel plates can be mounted on a remotely actuated table. Absolute flux normalization can be obtained from a channeltron (CEM) which was calibrated to about +/- 15% (Mack, Bowyer, and Paresce 1976) against an NBS Al_2O_3 windowless photodiode transfer standard (Saloman and Ederer 1975, Saloman 1978). The CEM was available in the vacuum tank as a beam stability and flux monitor. Comparisons between the CEMA and CEM rates provide a handle on the absolute efficiency of the plate.

The CEMAs were mounted in turn on the table in the vacuum tank so that the beam intercepted the input surface at seven degrees from the normal. This corresponds to the average angle of convergence of radiation focused from the mirrors to the CEMA. The beam diameter is about eight millimeters when it intercepts the CEMA. The CEM can be rotated into the beam to monitor the flux. The source intensity was adjusted so that the CEM and CEMA count rates were a factor of ten below the onset of deadtime corrections or high rate induced gain loss.

While each plate was in the beam the count rate ratio between it and the CEM was recorded. Data were taken at the two He II lines in the center of our bandpass, 256 Å and 304 Å. An additional point outside the band at 540Å was also noted. The ratio of efficiencies between the new plate and the CEM agreed well with those of other Berkeley plates. We are confident that the flight plate performed to theoretical expectations. The beam was used to test the spatial uniformity of the plates. The NBS plate efficiency decreased noticeably as the beam was brought close to the ion pump port. The flight plate appeared uniform to the coarse 10% limit of this survey. Channel plates usually have five percent inherent spatial variations associated with inhomogeneities introduced in the manufacturing and vacuum deposition processing. Table 3.3a summarizes the data from the two plates including absolute as well as relative efficiencies. At 304 Å the new plate was a factor of 10.5 better than the NBS plate while at 256 Å the improvement was about 5.6. At 540 Å the improvement was 5.3. Based on statistical errors and reproducibility the errors in these points are about +/- 8%. From the absolute efficiencies of table 3.3a it can be seen that the NBS plate has a large drop in efficiency at 304 Å while the flight plate has a small enhancement. We attempted to fit the NBS data with the efficiency drop and were unable to obtain reasonable χ^2. Independent calibrations of CEMAs and CEMs show fairly flat efficiency curves in this spectral range (Mack, Bowyer, and Paresce 1976, Timothy 1974) A possible source of the wavelength variation of the NBS Plate efficiency is the presence of surface contaminants. These could change the wavelength dependence of the photo-emission efficiency of the NBS plate from that of a the new plate. We cannot make this argument quantitative enough to explain the nature of our data.

Only two data points are available in our bandpass from which to estimate the improvement of the flight plate over the NBS plate, though one is at the

SUMMARY OF BERKELEY RESULTS			
wavelength (Å)	256	304	540
NBS PLATE/CEM	0.0833	0.036 0.036	0.051
NBS PLATE EFF	6.6×10^{-3}	4.1×10^{-3}	6.0×10^{-3}
FLIGHT PLATE/CEM	0.46	0.40 0.37	0.27
FLIGHT PLATE EFF	3.7×10^{-2}	4.1×10^{-2}	3.2×10^{-2}
IMPROVEMENT	5.6	10.6	5.3

table 3.3a

important He II 304 Å line. Lack of a clear understanding of the wavelength dependence of the calibration results obtained at the SSL leads to an uncertainty in the factor by which to scale up the NBS efficiencies. A reasonable approach is to average the scale factors at the 256 Å and 304 Å points giving an improvement of a factor of eight. A systematic error of about 30% corresponding to the 256 Å and 304 Å improvements as lower and upper limits respectively is retained to estimate the uncertainty in the measurement. A further independent check on the flight instrument efficiency is the agreement between our flight measurement of the emission of the night sky at 304Å, and that of previous experiments. This point is discussed in detail in chapter four where the flight data provide evidence that the instrument efficiency at 304 Å is consistent with that determined from this pre-flight calibration.

Figure 3.3a - The upper panel gives the response of the tungsten photoemitter in the XUV (Saloman 1978). The lower panel show the measurement circuit of the cathode current. The anode voltage was increased until the current reached a plateau.

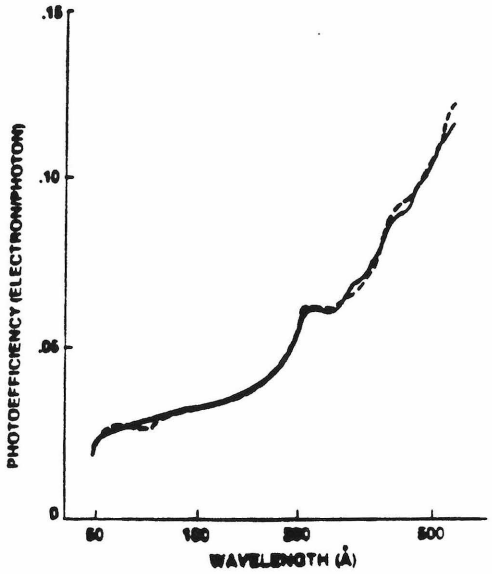
.15
.10
.05
0
PHOTOEFFICIENCY (ELECTRON/PHOTON)
50
100
200
500
WAVELENGTH (Å)

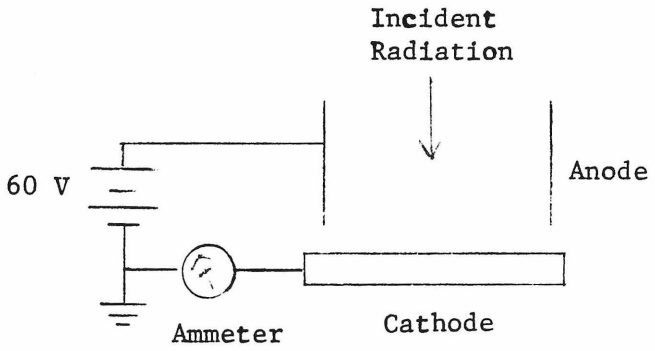
Incident
Radiation
Anode
60 V
Ammeter
Cathode

figure 3.3a

3.4 RESULTS FROM THE COMPLETE NBS DATA

The NBS data sets were interpreted to provide measurements of the detector position response function ,the photon detection efficiency in the zero, first, and second orders, and, consequently, the effective area in each order as a function of wavelength. Aside from these primary objectives the data also led to a greater understanding of the spatial uniformity of the diffraction gratings and the channel plate, as well as the XUV imaging quality of our mirrors. This section describes the methods of obtaining the flight efficiencies.

Each NBS data set is compiled into a 128 by 128 focal plane image array. An array element corresponds to 0.41mm on the channel plate or 1.1 arc-min in incident angle to optic axis of the mirrors. Figure 3.4a presents raw count spectra of a representative data set and table 3.4a summarizes the location of the beam at the gratings and in the focal plane for each set. The most important quantities in this table are the angular FWHM of the central maxima (zero order) for each set.

A. THE SPECTROMETER ANGULAR RESOLUTION

In flight calibration (performed by observing Capella in x-rays) of the mirrors during their previous flight, indicated that the mirror blur circle exceeds four arc-min. This is several times greater than previous laboratory optical and x-ray calibrations indicated. The NBS data address this question by putting a limit on the combined contribution of mirror blur and inaccurate location of the focal plane. It should be noted that the XUV blur circle measurement is only sensitive to local surface imperfections and not large scale figure distortions since the beam only illuminates a small fraction of the surface. The angular resolution is estimated in straightforward fashion from the profile of the

SUMMARY OF NBS DATA SETS			
set #	location	coord(x,y in pixels)	FWHM (arc-min)
-	geometric center of detector	61.5 67.5	-
1a	inner mirrors off grating	66.6 68.8	2.0
1b	outer mirrors on grating	65.1 68.0	2.0
2	outer mirrors on grating	65.4 67.8	2.0
3	outer mirrors on grating	51.3 52.8	2.0
4	inner mirrors on grating	65.5 67.4	2.0
5	inner mirrors on grating	60.4 72.9	2.0
6	outer mirrors payload rotated	70.0 64.1	2.0

table 3.4a

undiffracted image J_0. The method of estimation is illustrated from the data of figure 3.4a. The zero order counts total about 1500, while the two largest bins in zero order contain a sum of 1250 counts or 83% of the total. Each bin extends about 0.4mm to either side of the mean, thus giving the integral of the ideal gaussian input probability in this 0.8mm interval. The integral of a normalized gaussian from -1.25σ to $+1.25\sigma$ is also 0.83 so that 1.25σ=0.4mm. Translating to FWHM, and using the $\sim$ 2.7 arc-min/mm plate scale of the optics, produces about a 2 arc-min FWHM blur circle. Since the beam divergence is very small ($\cong$ 20 arc-sec FWHM), and contributes to the total width in quadratured the total instrument response is approximately 2 arc-min. This includes the combined contributions of the mirror aberrations, focal plane uncertainty, and the finite spatial resolution of the CEMA camera. The CEMA resolution was independently measured prior to and subsequent to flight and has an approximate FWHM of 1.8 arc-min. This indicates that the mirror blur is much smaller than 1 arc-min FWHM, consistent with previous x-ray optical laboratory calibrations. The angular resolution of the instrument is thus deduced to be better than 2 arc-min (0.75mm) FWHM. Using the diffraction angle of 17.4 arc-min for first order 304Å gives a $\frac{\lambda}{\Delta\lambda}$ of 8.7, or a $\Delta\lambda$ of 35Å.

B. EFFICIENCIES IN THE SPECTRAL ORDERS

Figure 3.4a shows the raw count spectrum of one of the six main data histograms. Two features stand out which have a bearing on the efficiency determination. The first is a small asymmetry in count rate between the two sides of the diffraction pattern. The position of lower efficiency corresponds to the ion pump port. As mentioned in section 3.3 the ion pump corner of the CEMA was found to be somewhat less efficient at Berkeley than the other side of the plate. This was

possibly a result of the electron bombardment. The relative calibration of the two plates performed there used the high efficiency side of the NBS plate for its comparison. Consequently we only reduce the half of the NBS spectra on this side of the plate.

The second feature evident from figure 3.4a is the presence of a small amount of second order in the data sets. This is a result of the fact that the NBS grating did not have precisely equal open and opaque lines. The ratio a/p of the open linewidth to grating period was found to be 0.4 by fitting the ratio to the relative efficiencies in the zero, first, and second orders in the NBS data.

To determine the zero and first order efficiency as a function of wavelength from the calibration data, the instrument angular resolution and grating second order must be removed from the data. This deconvolution was achieved by generating a model instrument response function which is convolved with the previously determined angular response and the synchrotron flux spectrum to give a model dependent predicted count spectrum. The three free parameters in the instrument model correspond to the absolute normalization (anorm), the relative efficiency of first to zero order (afirst) and second to zero order (ascnd). In principle the later two are not independent, but determined by the ratio of open to closed area of the gratings as described in section 2.1. A model with this ratio and the overall normalization as free parameters was also fit to the data. For a grid of parameter values the predicted count spectrum is compared with the observed, and χ^2 computed. The resulting χ^2 grid is searched for the best fit, giving an estimate of the efficiency. Errors are assigned from the χ^2 grid using the technique described by Lampton, Margon, and Bowyer (1976). This procedure is now made more precise.

In order to include the effects of the measured angular response with the

model efficiency K(λ), we convolve them to produce the following expression for the detected counts.

$$cts(\lambda) = \int_{170\text{Å}}^{600\text{Å}} dx \quad \frac{1}{\sqrt{2\pi}\sigma} e^{\frac{(\lambda-x)^2}{2\sigma^2}} \quad K(x)$$

The gaussian corresponds to the measured angular resolution discussed in section 3.4a. The incident synchrotron spectrum F(x), see figure 3.2b, is included in K(x), and the upper limit in the integral is sufficiently large that the contribution from λ>600Å is negligible.

In fitting to the total counts in J_0, K(x) is given by:

$$K(x) = \text{anorm } F(x)\ T(x)$$

F(x) is the synchrotron spectrum, see figure 3.2b, and T(x) is the bandpass filter transmission function from figure 2.1b. The assumed wavelength independent factors of total grating transmission, mirror reflectance, and CEMA efficiency have been absorbed in anorm which is a free parameter.

In fitting the first (J_1) and second order (J_2) components:

$$K(x) = k_1(x) + k_2(x)$$

With:

$$k_1(x) = \text{afirst} * \text{anorm} * F(x) * T(x)$$

And:

$$k_2(x) = \text{ascnd} * \text{anorm} * F\left(\frac{x}{2}\right) * T\left(\frac{x}{2}\right)$$

afirst is the efficiency of J_1/J_0 and ascnd is J_2/J_0. The wavelength dependence of the efficiency is determined entirely by the filter response T(x) in this model. The main physical assumptions relevant to the model are that the CEMA and grating efficiencies are approximately wavelength independent over the 170Å to 450Å bandpass. The validity of these assumptions is suggested by independent XUV measurement of CEMA responses (Mack, Bowyer, and Paresce 1976), and gold grating calibrations (Brinkman et al 1979; Predehl, Haelbich, and Braunginger 1979), as well as by the failure of models incorporating wavelength dependent efficiencies to fit our data. At the SSL it was noted that the CEMA efficiency did vary between the calibration points. Fits to the NBS data incorporating this variation generate poor χ^2 so it is felt that they were not present at the time of the NBS runs. Additional efforts to fit the data to small linear efficiency changes (a few percent per hundred Angstroms) also failed to provide reasonable fits.

The first step in implementing the deconvolution procedure is to bin the data into the count-wavelength distributions shown in figure 3.4a. A small complication arises here because the diffraction pattern makes an angle of 30° with the electronic readout axis. In each wavelength bin we would like the sum of the number of counts perpendicular to the diffraction direction. If the resolution elements of the electronics readout were small compared with the instrument response these sums could easily be performed. In the present situation, however, the electronic and instrument resolutions are comparable. Figure 3.4b shows the geometry. The centroid (y_i) of the y counts at at each x_i is computed and the total number of counts in these bins is assigned to the point (x_i, y_i). The wavelength at x_i, y_i corresponds to the distance from this point to J_0. Assuming the counts to be uniformly distributed within 1½ pixels of the axis the contribution to the number of counts to bins perpendicular to the axis from an x bin can be estimated. The correction derived from the geometry of figure 3.4b is:

$$cts(s)=0.67\, f_i + 0.17(\, f_{i-1} + f_{i+1})$$

s is the distance to the i^{th} point from J_0 and f_i is the number of counts associated with the i^{th} point. It turned out that the exact form of this correction was not significant. In fact varying the coefficient of f_i from 0.5 to 0.75 had no influence on the fits.

Figure 3.4c shows the fits produced by application of this deconvolution technique to data set one. The data points indicate the count rates in each wavelength bin on one side of first order. The errors are statistical and no background subtraction was necessary. The solid line results from convolving the two parameter instrument model (normalization and ratio of open line width to period of the grating a/p) with the beam flux and angular response functions. Best fit was an open to period ratio of a/p=0.4 consistent with that expected from fabrication of this grating (see section 2.5). The dashed line indicates the first order component of the model diffracted radiation ($k_1(x)$) before being degraded by the finite angular resolution of the instrument. This curve is used to calculate the first order efficiency of the spectrometer. It can be seen from the figure that the fit is quite reasonable. Not shown is the integral under the first order curve which is related to the total number of counts in zero order by the relative efficiencies in the orders given by a/p. The total χ^2 is 18 for 16 DOF. Reducing all six data sets with this technique leads to the spectrometer efficiency curves of figure 3.4d. They give the fraction of incident photons appearing in one side of first order. The total first order efficiency is twice the value shown. Recall for a moment the rough online efficiency measurement outlined in section 3.3. With the beam on the inner mirrors we found an average efficiency on the order of 2×10^{-4}. If we use the value of 3×10^{-5} at 300 Å from figure 3.4d and double it for the total first order efficiency and double again to

account for the zero order efficiency we get 10^{-4} which is in reasonable agreement with the previous estimate considering the nature of the approximations. The four high efficiency data sets of figure 3.4d were taken on the outer mirror set, while the lower two sets are from the inner mirrors. Ignoring this disparity momentarily, the agreement between the four outer data sets is quite reasonable, and consistent with the errors determined by the χ^2 grid technique.

It was found that the transmission of the inner and outer gratings differed by about a factor of $\simeq$1.7 near center. The source of the factor of $\cong$ 1.7 was uncovered while doing optical studies of the gratings with a laser. Observations with an optical microscope showed the two masks used to generate this grating were misaligned in this area causing obscuration. In addition there seemed to be particle contamination of the inner grating, most likely the result of residual glass from the etching process. The nearly precise agreement between the inner and outer mirror transmission ratios obtained in the x-ray and optical argue convincingly for this explanation. It also raises the concern that similar discrepancies might arise in the flight gratings. The problem of mask alignment will not be present in the flight gratings. Two masks were used in producing the prototype gratings to allow the addition of more support wires to test the grating response to vibration. A single mask incorporating the suitable grating and support structures was then generated for the flight fabrication. The importance of careful examination of the gratings for contaminants was not fully appreciated until the batch processed gratings became available. Only the outer mirror section of the NBS grating was examined, and it was virtually free of particle obscurations. Furthermore, the flight gratings underwent considerable microscopic inspection to insure that only the highest quality gratings of each batch were mounted on the mirror cell. We are confident that nonuniformities similar to those found on the NBS grating were not present on the flight

gratings.

C. Flight Efficiencies

To derive the flight effective areas the outer mirror efficiencies of figure 3.4d were averaged and scaled up by the relative efficiency gain of the flight CEMA over the plate used at the NBS as discussed in section 3.3. In the discussion of grating fabrication in section 2.1 it was noted that the prototype gratings had open line to period ratios of about 0.4 as a result of the thickness of gold used in their construction. This is evident in the NBS data which show the presence of second order in the spectra and give best fit ratios of first to zero and second to first orders consistent with a/p=0.4. Because of the reduced thickness of the flight gratings we expect a/p to be much closer to 0.5. This is borne out by electron micrographs of these gratings showing a/p to be essentially 0.5. This necessitates a small increase of five percent (see section 2.1) in the NBS efficiencies to compensate for the differing linewidths. The resulting efficiency is multiplied by the geometric acceptance of the mirror cell to produce the effective areas given in table 3.4b. The efficiency in zero order is about 20% greater than the first order efficiency.

EFFECTIVE AREA IN FIRST ORDER			
wavelength (Å)	area (cm^2)	statistical	systematic[2]
180.0	.335	.038	.088
200.0	.292	.033	.078
220.0	.256	.029	.068
240.0	.221	.025	.059
260.0	.190	.022	.050
280.0	.159	.018	.042
300.0	.132	.015	.035
320.0	.108	.012	.029
340.0	.087	.010	.023
360.0	.068	.008	.018
380.0	.054	.006	.014
400.0	.041	.005	.011
420.0	.032	.004	.008
440.0	.023	.003	.006
460.0	.017	.002	.005
480.0	.013	.001	.003
500.0	.008	.001	.002
520.0	.006	.001	.002
540.0	.004	.000	.001

1. This is the effective area summed over both first order components of the spectrum.
2. The systematic errors arise from the calibration of the flight CEMA relative to the NBS CEMA as discussed in section 3.3.

table 3.4b

Figure 3.4a - The raw focal plane count spectrum accumulated in 200 seconds for a typical data set is displayed as a function of the wavelength. The center of the plot indicates the zero order peak and the diffracted image appears to either side. The image should be symmetric about the zero order image but there is an asymmetry after 300 Å on the left (negative) side. This asymmetry appears in all data sets and is associated with the portion of the channelplate near the ion pump port. It is speculated that electron bombardment may have induced the problem. As discussed in the text this plate was replaced prior to flight and the new plate was only sorption pumped. A design improvement would be a fine wire grounded mesh at the ion pump port to reduce the number of electrons striking the CEMA.

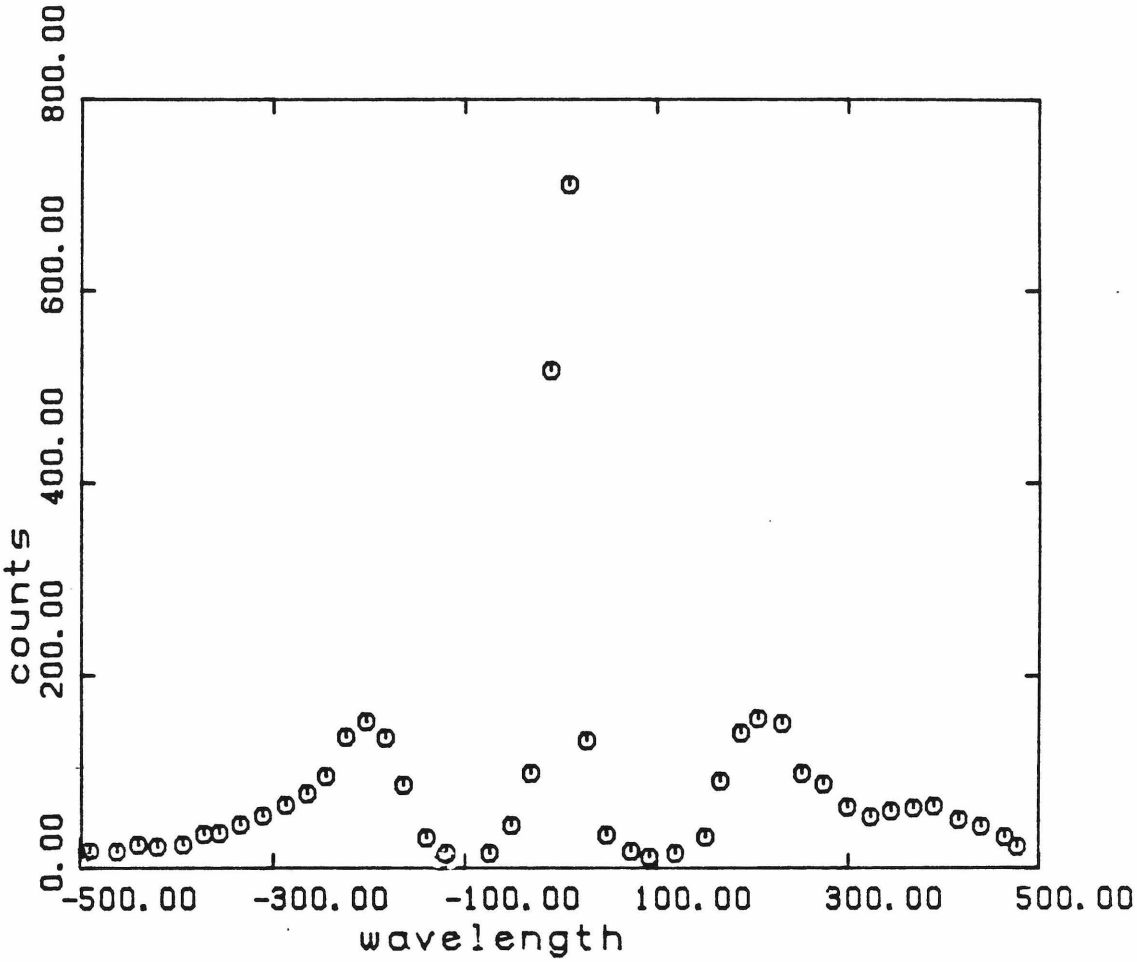
800.00
600.00
400.00
200.00
0.00
counts
-500.00
-300.00
-100.00
100.00
300.00
500.00
wavelength

figure 3.4a

Figure 3.4b - This figure illustrates the difficulty associated with the fact that the electronic resolution elements are comparable in size to the instrument point response function. The x and y axes are the focal plane camera readout axes which make an angle of 32° with the diffraction axis. At each point on the diffraction axis we would like the sum of the counts perpendicular to this axis. Readily available however is the sum over y of the counts at each x bin. From the overlap geometry and the assumption that counts are uniformly distributed within 1½ pixels of the axis we find the approximate correction given in the text. Since variations in the correction parameters caused little change in the resulting efficiencies more sophisticated approaches were not taken.

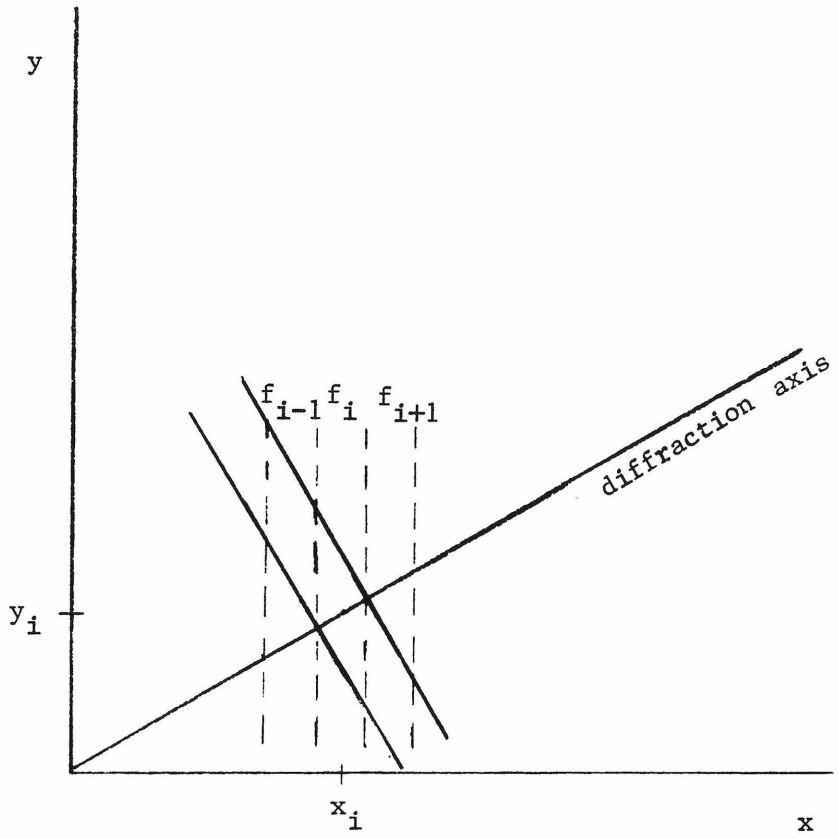

figure 3.4b

Figure 3.4c - The first order spectrum from data set one is indicated by the points. The solid line is the result of convolving the model spectrum with the angular response function of the detector for a grating with a/p=0.4. The model is also constrained to fit the total number of zero order counts, not shown in the figure. The dashed line is the first order component of the model fit only.

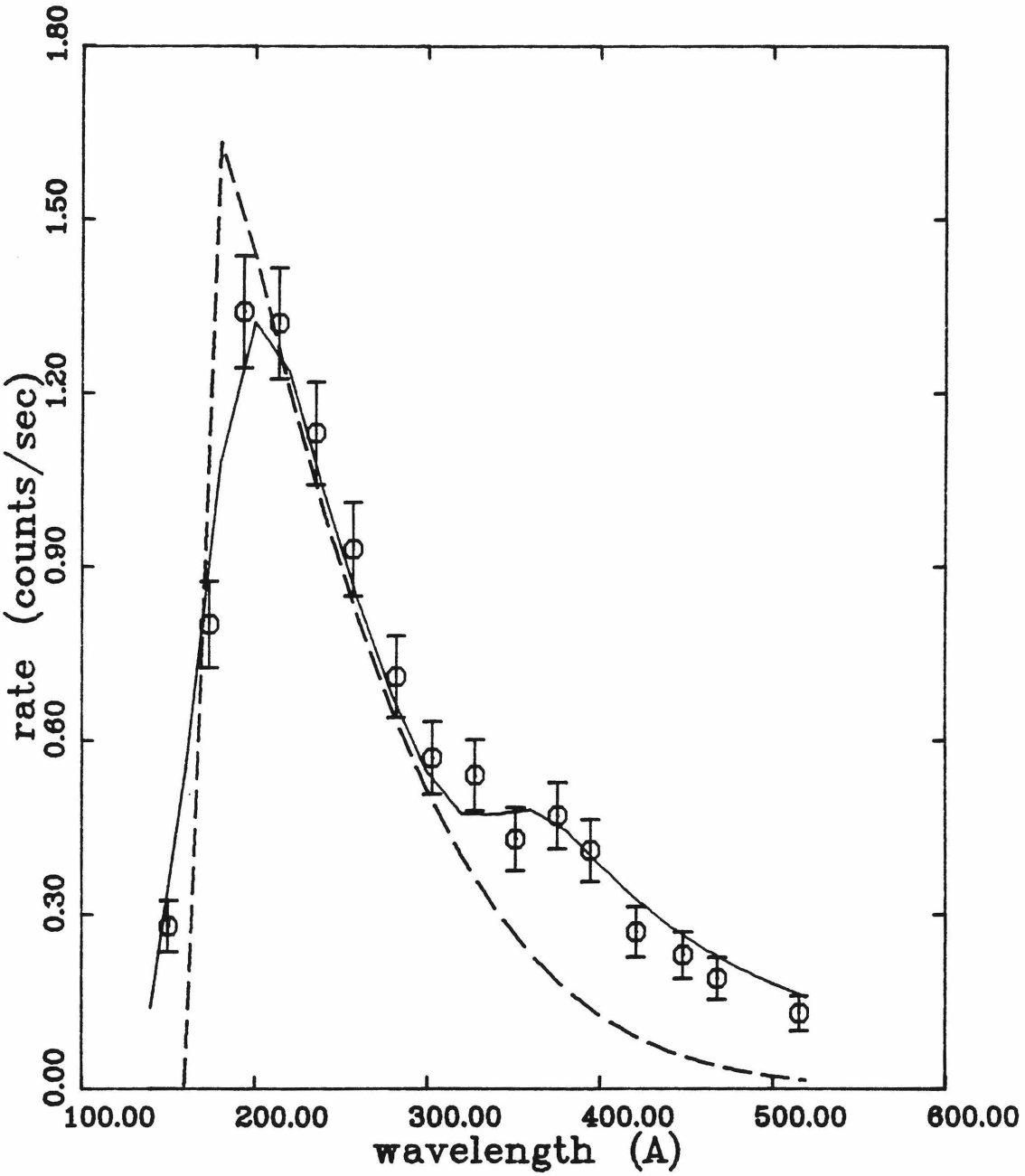
DECONVOLUTION OF FILE #1
rate (counts/sec)
0.00
0.30
0.60
0.90
1.20
1.50
1.80
100.00
200.00
300.00
400.00
500.00
600.00
wavelength (A)

figure 3.4c

Figure 3.4d - The spectrometer efficiency in one side of first order for each of the six data sets is displayed as a function of wavelength. The total first order efficiency is double that shown. The upper four curves correspond to the data sets taken on the outer mirrors, while the lower curves were taken from the inner mirrors. The reasons for the discrepancy between the inner and outer sets are covered in section 3.4. The scatter between the sets on each mirror is a good indication of the accuracy of the calibration at the NBS.

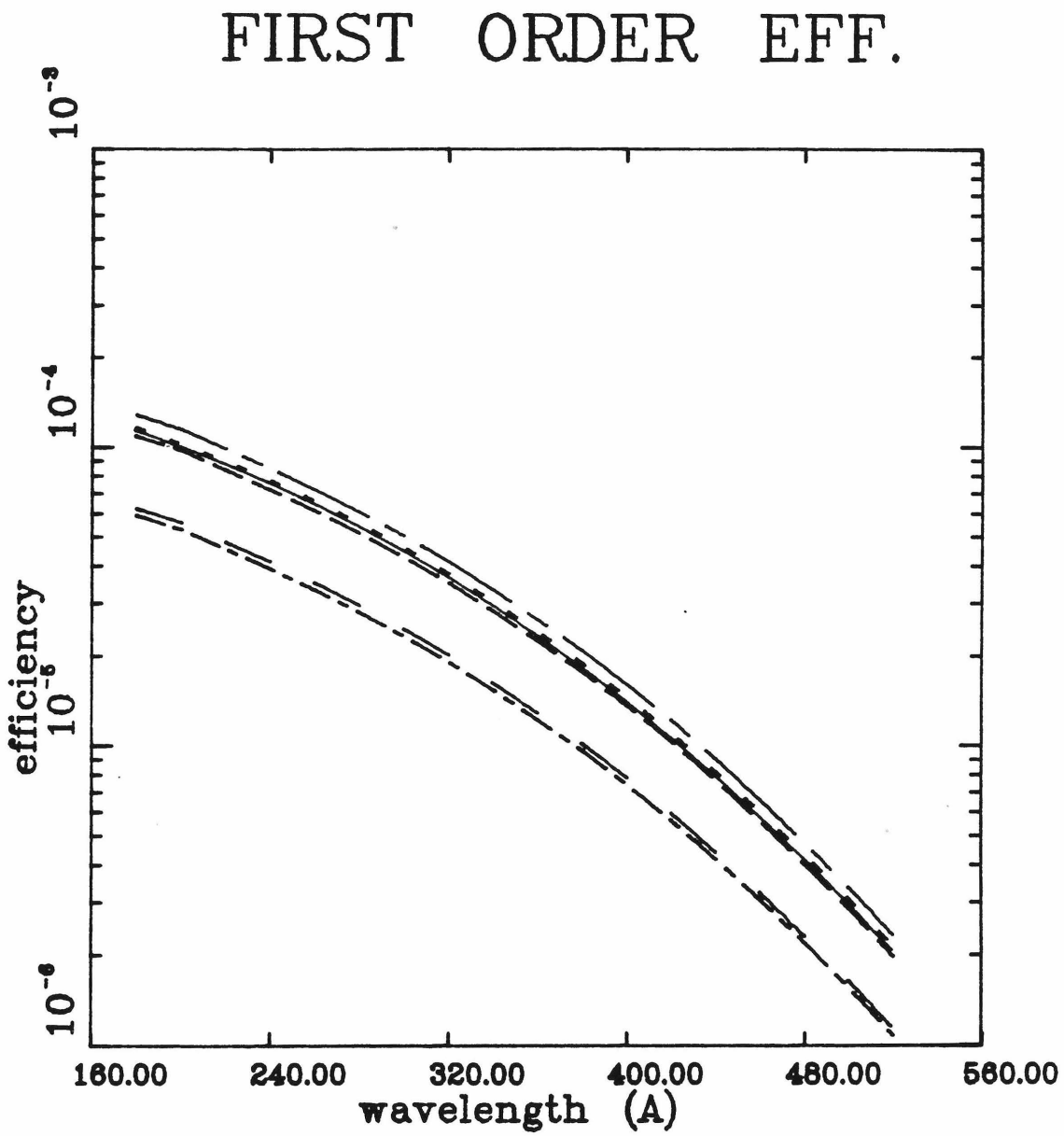
FIRST ORDER EFF.
efficiency
10^-3
10^-4
10^-5
10^-6
160.00
240.00
320.00
400.00
480.00
560.00
wavelength (A)

figure 3.4d

CHAPTER 4

4.1 Vehicle and Support System Performance

Pre-flight payload assembly, and integration with the telemetry and attitude control system (ACS) were carried out at White Sands Missile Range (WSMR). Star tracker alignment was repeated using the same technique as at GSFC (outlined in section 2.2). The flight camera and fiducial light aspect verification subsystem were tested simultaneously. No problems with the aspect systems were uncovered. Full tests of the experiment operation, telemetry, and timing functions were performed in the horizontal using flight event sequencing. Tests were carried out in the flight configuration with the exception that the MCP vacuum was maintained by an external sorption pump to permit operation.

The experiment, telemetry, attitude control, and recovery systems were integrated to flight configuration and mounted on the Black-Brandt. The completed assembly was placed in the launch tower and a final flight simulation performed. After the vacuum dome and nose cone were attached the experiment section was cryo-pumped through a pull-away vacuum connector. The pre-launch vacuum specification of 10^{-4}~10^{-5} torr was met after two days of pumping. This vacuum level was slightly above the corona threshold for the channel-plate high voltage, inhibiting detailed pre-flight MCP internal background studies in the tower. Operation of the plate for short time intervals to verify functioning of the electronics was possible.

Launch was at 20:00 hours MST on March 23,1981. At the time of launch Capella had a zenith angle of about 34° and an azimuth of 305°, while the solar zenith and azimuthal angles were 112° and 287° respectively. An apogee of

260km was obtained providing over 200 seconds of data above 220 km. The payload section separated from the second stage Black-Brandt 48 seconds into flight. The nose-cone ejected at T+65s (82km). The experiment electronics were powered on at T+74s (98km), and positive verification of the MCP valve opening was received at 90s (124km). Verification of the MCP valve closing occurred at about 455s (95km), and power shutdown was at 480s. Continuous, error free, telemetry was provided for the entire flight in both PCM links.

A brief period of enhanced detector counting rate occurred at the initial power on altitude (100km) and immediately before power off (100km) on the descent. The broad extent of the discharge and the symmetry in altitude of its occurrence strongly suggest a coronal discharge in the MCP due to poor ambient vacuum. The discharge was noted in the total event scaler, the live focal plane camera display, and the post flight digital data. On the ascent the discharge rate fell from 1,000 counts/s to ~100 counts/s in less than 8 s, presumably as the payload outgassed and external vacuum fell. The nature of the discharge on descent was almost identical.

The sole flaw in instrument operation was a temporary malfunction of either the Nikon shutter mechanism, or Nikon firing control system which caused the dropout of five star field photos during flight. Nine photos were obtained prior to the malfunction and five were taken after. This dropout is not serious since the star tracker jitter cycle is monitored during flight via the TM and is no greater than a few arc-secs. Once an initial verification of aspect is made the stability of the tracker insures that no significant changes arise. Gains and offsets of the analog electronics relevant to the position sensing were determined during flight from the digital positions of the edges of the MCP. Agreement with pre and post-flight values was better than 1%. Corrections to position calibration from 1% shifts in these parameters are considered unimportant.

Pointing aspect was obtained by comparing the position of Capella relative to the fiducial lights on the flight photographs with that of the laboratory calibration star. Since the Nikon has an 85mm lens one arc-min aspect requires measuring film images to better than 0.001 inches. Two independent techniques were used: a micrometer controlled microscope table reproducible to +/- 0.001", and a projection system in which the slide is mounted on a precision mill table and projected on a screen. Accuracy of the latter technique was double that of the microscope. Capella was located to within a 2.7 by 2.7 arc-min error box in the focal plane. Independent aspect determinations were made before and after apogee. No changes in the pointing location were noted. This is consistent with the five arc-sec pointing cycle of the ACS measured during flight.

Recovery was somewhat less successful. A butterfly valve designed to protect the mirror cell on re-entry was opened by the landing impact. Sand was driven through most of the gratings and into the lower optical bench. This prevented positive verification that all gratings survived launch. Observations of the failed gratings provide several indications that the damage was incurred at impact rather than launch. About half the gratings were intact after landing, and those farthest from the region directly exposed by the partially opened butterfly valve sustained the least damage. Furthermore the damaged gratings exhibited holes where material was completely removed, while the grating surrounding these holes was approximately intact. During vibration testing of the prototype gratings it was noted that failures occur at the boundary between the gratings and the brass mounting frames rather than at grating center. Only the gratings which received the full impact of the sand exhibited tears at the frame-grating boundary. Most significantly pre-launch testing of the gratings showed they would survive launch even at one atmosphere. We are thus confident that the all gratings were intact during the data taking period. The XUV bandpass filter was not damaged by the sand so its integrity was verified.

4.2 The Inflight Geocoronal Photon Background

Flight data analysis was initially approached by understanding the uniform, off source, focal plane count rate. These background events consist of the CEMA internal background, and the diffuse sky emission. Sky emission in our bandpass originates in the resonant scattering of solar helium line photons by neutral and singly ionized helium in the Earth's upper atmosphere and plasmasphere. The altitude dependence of these two background sources is quite different. Sky emission will show a distinctive altitude variation caused by absorption of the line photons in the residual atmosphere above the rocket. Internal background is mostly independent of altitude though it rises when the ambient vacuum is near 10^{-5} torr or the payload is outgassing. A short period of outgassing was expected immediately following nose eject.

Raw detector count rates for both the ascent and descent are shown in figure 4.2a. Rates are taken from an area of 18 cm^2 (0.4 square degrees) in the center of the focal plane (field of view) which excluded the source error box. Each point in the figure represents the counts accumulated during a ten second interval around the given altitude. During descent the count rate is observed to level off below 125 km. Data below this altitude are not available from the ascent because the MCP valve was still closed. The residual rate at low altitude is due solely to the MCP internal background since the geocoronal photons are completely photoabsorbed by the atmosphere (see below). This allows isolation of the two background sources. The two points at 125km (55cts) and 106km (65cts) imply that the internal background is about six counts per second. From the data of figure 4.2a it is also evident that the count rates below 200 km are somewhat lower on the descent than on the ascent. This is most likely a result of the payload outgassing following nose ejection on the ascent. It can be seen from the figure that the ascent and descent rates become equal above

190km.

The main feature of figure 4.2a is the dominant contribution of the diffuse sky emission to the detector count rate. At peak altitude it exceeds the internal detector background by a factor of six. Lines contributing to the sky background are He I 584 Å and He II 304 Å. He II 304 Å is the primary component of the background photons registering in the detector because the bandpass filter suppresses the He I 584 Å line by a factor of 70 over He II 304 Å, while the flux in He I has been measured to be to be less than four times greater than He II 304 Å (Meier and Weller 1972, Riegler and Garmire 1974; see table 4.2a). Though the strong geocoronal background has the adverse effect of reducing sensitivity to source emission from Capella, it can be used to establish the instrumental sensitivity at 304 Å. Inflight verification of the spectrometer response at 304 Å is crucial to the subsequent analysis of the Capella spectrum since no Capella emission was detected at He II 304 Å (see section 4.3).

Altitude dependence of sky emission is characterized by photo-absorption in residual molecular nitrogen and oxygen and atomic oxygen above the rocket altitude. A model atmosphere was constructed in order to fit the data of figure 4.2a to a theoretical extinction curve at 304 Å. Absorber densities as a function of altitude were obtained from the 1976 U.S Standard Reference Atmosphere (NASA 1976). Values of the densities correspond to periods of high solar activity since launch occurred near solar cycle maximum. (It was found, however, that the density variations induced in the above species by solar activity levels produce fairly small changes (less than 5%) in the atmospheric transmission at these altitudes and wavelengths.) Photo-absorption cross-sections in the XUV were taken from Allen (1973). A two parameter fit was chosen which incorporated a variable admixture of 304 Å and 584 Å radiation, as well as an overall normalization. The non-sky background was taken to be 6 cts/s from the data

below 125km and was assumed altitude independent. Fits were made to the descent data only because the ascent data does not contain a reliable estimate of the non-photon internal detector rate at low altitudes. A χ^2 grid was computed for models ranging from entirely 304 Å photons, to solely 584 Å photons. The pure 304 Å model is consistent with the data ($\chi^2 \sim 1.2$ for 9 DOF) while the best fit was for a 25% contribution from 584 Å. Because of the presence of the filter however, it is very unlikely that 584 Å contamination amounted to more than a few percent. The solid line in figure 4.2a represents the best fit of a pure 304 Å extinction curve to the data. The main reason a pure 584 Å model doesn't provide a good fit is that one attenuation length in the atmosphere for 584 Å was found to occur at an altitude of 175 km. Consequently the 584 Å intensity falls off too rapidly below 175 km to agree with the data. For 304 Å one attenuation length is near 155 km. As a check on the accuracy of the model calculations of atmospheric absorption, the altitudes at which one optical depth occurs for several XUV wavelengths were compared to those determined independently by Allen (1976). The extinction curves also agree well with those determined by Paresce, Bowyer, and Kumar (1973), based on the Jacchia (1970) model atmosphere. Subsequent data analysis is based on the assumption that the entire diffuse sky background in our detector originates from 304 Å photons. The atmospheric model is also used to calculate the absolute transmission of the atmosphere above the rocket to the XUV wavelengths. At apogee (262 km) the transmission towards Capella is 91% at 304 Å.

Agreement between the observed altitude variation of the count rate and that expected from the atmospheric absorption model is strong evidence that the spectrometer operated properly for the entire flight. Clearly the MCP is exhibiting a response to 304 Å radiation. The sensitivity to 304 Å photons was also found to be uniform over the field of view. This is discussed in detail in

section 4.3. A comparison between the normalized value of the 304 Å diffuse sky emission obtained with this experiment to previous independent experiments provides a consistency check on the calibration of the effective area at 304 Å performed at the NBS. To implement the comparison the data of figure 4.2a are used to derive the sky surface brightness. From the low altitude residual count rate we deduced a non-photon detector background contribution of six counts per second. At peak altitude the total count rate is about 40 per second. Thus the sky 304Å rate is 34 counts per second. Because the emission is diffuse the spectrometer efficiency will be the sum of the zero and first order efficiencies. (ie. the total transmitted efficiency of the grating since the contribution from higher orders is < 5%). From the calibrated effective areas given in table 3.4a, the sum of first and zero orders is about 0.27cm^2. Data in figure 4.2a are taken from a field of view of $\simeq 1.1\times10^{-4}$ steradians. The sky brightness I is the number of photons per cm^2 per second per steradian. For an atmospheric transmission of 91% at 262km I is given by:

$$I = \frac{34 cts/sec}{(1.1\times10^{-4} str)(0.27 cm^2)(0.9)} \simeq 1.2\times10^6 \qquad ph\ cm^{-2}\ s^{-1}\ str^{-1}$$

at a zenith angle of 34°. To facilitate comparison with previous measurements the sky brightness I we observed during this flight is converted to units of Rayleighs (one Rayleigh is defined as $1/4\pi\times10^6$ ph/cm^2-s-str). This gives I $\simeq$ 16R. Table 4.2a presents a comparison with some previous observations. The measurement reported in this work is somewhat higher than those carried out in the early and mid seventies. Plausible explanations are that the sensitivity of the instrument is higher than the NBS calibration indicated, or that the solar He II 304Å line flux was substantially more intense during our launch period than at the time of previous launches owing to variations in solar activity.

Geocoronal 584 Å and 304 Å Fluxes					
Investigator	year	sol. zen ang	apogee (km)	584 Å	304 Å
Young *etal*[1]	1967	131°	225	<12 R	5 R
Young *etal*[1]	1969	134°	217	<4 R	7 R
Paresce et al (1973a,b)	1970	150°	185	15 R	8 R
Ogawa[1]	1970	130°	300	40 R	10 R
Reigler+Garmire (1974)	1971	130°	180	5 R	2 R
This flight	1981	110°	260	-	16 R

1. adapted from Meier and Weller (1972)

table 4.2a

This latter hypothesis was tested by comparing the measured solar 304Å line flux at the time of the previous flights with the value in March 1981. Data prior to 1976 are summarized by Timothy (1977) while Hinteregger (priv comm 1982) has satellite monitors for the solar 304Å line during the interval from 1976 to July 1981, including extensive coverage during the period from April, 1980 to April 1981. He has indicated that the solar flux was enhanced during early 1981 (including March) over the mid seventies intensities by a factor of two, however his data has not been thoroughly analyzed. Timothy (1977) has shown that the solar 304 Å emission is roughly correlated with the 10.7 cm radio emission. 10.7 cm emission originates in the upper TR to Corona and thus provides some indication of the solar activity level; 100 ($\times 10^{-22} Wm^{-2} Hz^{-1}$) is considered quiet, 160 medium, and 220 is active. The 10.7 cm index for March 23, 1981 (NOAA) was 195 which is about 70% greater than typical 1976 values. This would imply a solar 304 Å line flux about 40% greater than mid 70's values if one accepts the correlation presented in Timothy (1977). The 10.7 cm fluxes during the launch periods of the geocoronal observations reported in table 4.2a were also found to be in the vicinity to 180 → 190, which fails to explain the discrepancy with our measurement. Timothy (1977) points out that correlations between 10.7 cm flux and XUV and EUV fluxes are still not very well established due to normalization difficulties in the XUV flux measurements in the late sixties and early 70's upon which his analysis is based. When more recent data such as the 1977 → 1982 solar monitoring of Hinteregger are fully analyzed a better understanding of the solar flux variations will arise. The solar 10^5 K EUV lines, especially C IV, should be reliable indicators of He II 304 Å fluxes. C IV emission in July of 1980 was twice its solar minimum value (Mount and Rottman 1981) and seems to scale linearly with 304 Å intensities (Torr et al 1979; Rottman 1981) however insufficient monitoring has inhibited establishment of a correlation.

Present evidence is insufficient to verify that the origin of the large sky emission deduced from this experiment is due to a significant increase in the solar He II 304 Å emission. It is reasonable to infer from the discrepancy with other independent geocoronal intensity measurements at 304 Å, that the spectrometer sensitivity during flight is consistent with or possibly exceeds, by as much as a factor of two, that deduced from the XUV calibration at the NBS.

figure 4.2a - The vertical axis indicates the total count rate, in ten second bins for a 0.4 square degree field of view excluding the source error box, at the altitude given by the horizontal axis. Circles indicate data from the ascent, while the triangles are taken from the descent. Above 200 km the dominant contribution to the count rate originates in the resonant scattering of the solar He II line by He II in the Earth's plasmasphere. The solid line is the best fit model atmospheric extinction curve at 304 Å as discussed in section 4.2.

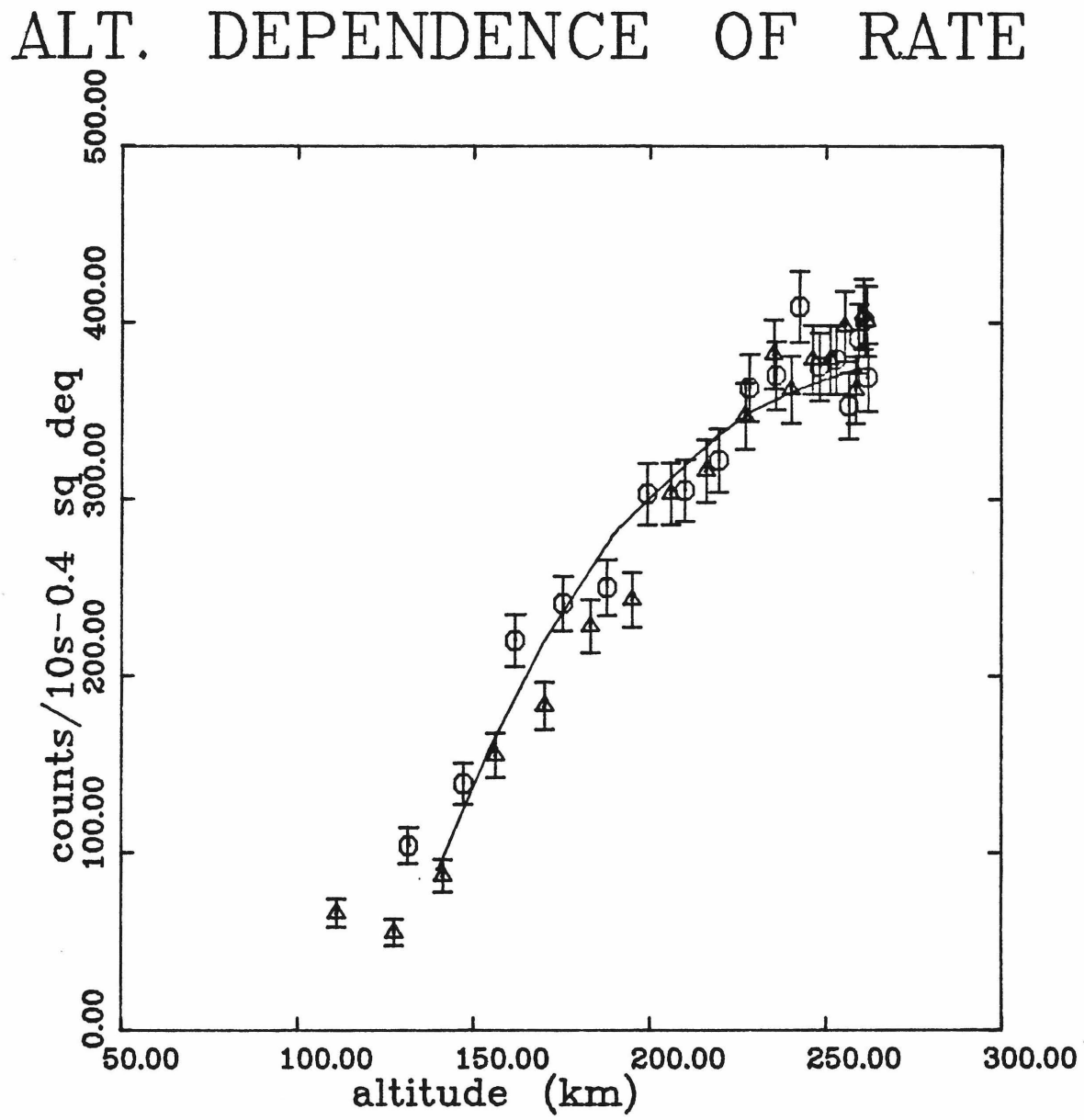
ALT. DEPENDENCE OF RATE
counts/10s-0.4 sq deq
0.00
100.00
200.00
300.00
400.00
500.00
50.00
100.00
150.00
200.00
250.00
300.00
altitude (km)

figure 4.2a

4.3 The Capella Spectrum

Measurement of the Capella spectrum is based on the 200 seconds of data acquired above 220 km. Little increase in sensitivity can be gained by using data below this altitude because the ascent and descent are rapid below 220 km providing little time and atmospheric absorption becomes severe.

Events telemetered during this 200s interval are compiled into a two dimensional focal plane count array. Each array element represents the counts registered in a 0.2mm by 0.2mm pixel at a given x and y coordinate on the MCP. The section of this array corresponding to the 1mm by 1mm (2.7 by 2.7 arc-min) error box for Capella was searched in a raster scan for the most likely location of the zero order undiffracted source signal. This location is defined as the point containing the maximum number of counts within an approximately circular beamwidth centered on that point. The beamwidth is taken to be the 2 arc-min FWHM of the instrument point response function measured at the NBS (see section 3.4A). All pixels lying within a beamwidth are weighted equally in this procedure. The maximum number of counts found in this manner was 37. For comparison the average number of counts contained in a beamwidth not located in the source error box is 22. Judgement as to whether this constitutes a significant detection is withheld until the relevant analysis of this section is completed.

As discussed in section 1.3 the Capella XUV spectrum is expected to consist of discrete line emission. Furthermore the Capella lines prominent enough to be accessible to this experiment will also be resolved by the ~35Å resolution of the spectrometer. Under these hypotheses all the flux in a particular line will be focused to a spot of 2 arc-min FWHM on each side of first order. On this basis the reasonable method of search for line emission is to step the beam along the

direction of diffraction summing counts within the beam response element. The step size is 9.3 Å or .54 arc-min. Counts recorded in each beamwidth are assigned to the wavelength corresponding to the distance from the (assumed) location of the undiffracted image. Since the beamwidth is larger than a single step size a correlation between counts at neighboring wavelengths is generated by the overlapping beamwidths.

Figure 4.3a shows the result of compiling the source spectrum in this fashion. The vertical axis indicates the number of counts in a beamwidth centered on the wavelength shown on the horizontal axis. The position indicated by 0 Å is the the anticipated location of the zero order (undiffracted) Capella image as deduced from the raster scan of the error box.

Consider first the qualitative features of the raw data shown in figure 4.3a. With an expected Capella 304 Å flux of about 1.5 phcm^{-2} s^{-1} (see table 1.4a, and an effective area of 0.07 cm^2 per side of first order over 20 counts above background are expected in the 300 Å bins. An additional 45 counts above background would also appear in zero order. Clearly this is not the case. It can also be inferred from the figure that there may be systematic changes in the detector sensitivity near the positions corresponding to -140 Å and zero Å. The broad nature of the count rate enhancement near the undiffracted image (0 Å), and the narrow dip below the mean in the wavelength region excluded by the XUV filter are convincing evidence that the non-statistical distribution of the counts is unrelated to the source.

Several approaches were taken to better understand the nature of this effect. To investigate the extent of the problem spectra were taken at random locations in the field of view, using the same technique as for the source. In addition test spectra were generated with a hypothetical diffraction axis

orthogonal to that of the actual grating alignment. Figure 4.3b is very representative of spectra derived in off source locations. Assuming statistical errors of $\sim\sqrt{N}$ where N is the number of counts in each bin the reduced χ^2 was computed in many locations, as a measure of the fluctuations in the data. Only statistically independent points were used. χ^2 was generally found to range from 1.0 to 1.3 for 16 DOF in the off source locations. The fact that χ^2 was always slightly greater than 1.0 is probably due to small non-uniformities in the MCP and readout, but these systematics are not found to cause noticeable fluctuations in the data, they appear to be approximately randomly distributed. By contrast χ^2 in the source location is about 1.7 for 16 DOF

Counting statistics of individual pixels were studied by compiling count against frequency distributions averaged over several regions in the field of view. These distributions agree closely with those expected from Poisson statistics. Mean values of the background rates were also compared between different locations in the center of the field of view and found to vary by less than 7%. From these data we must conclude that the problem is confined to a unique location on the MCP.

If the decreased efficiency spots suggested by the data of figure 4.3a are caused by non-linearities in the MCP readout a similar count distribution would be expected in data from the same region taken below 200 km. This data set is not likely to contain any source counts and, more importantly, is statistically independent of the data above 220 km. The raw distribution obtained below 200km for the combined ascent and descent, is shown in figure 4.3c. Inspection of figures 4.2a and 4.2c (ie data>220 km and data<200 km) reveals a similarity in the count rate dips at +/-140. Unfortunately the low counting statistics of this sample make detailed comparisons of the two data sets impossible. As a final point we add that the fluctuation was not observed in the post flight

calibration.

It is evident that the on source data contain non-statistical fluctuations. Since the fluctuations occur in the region excluded by the filter and include prominent excursions below the mean count rate they are inconsistent with an origin in the spectrum expected from Capella. There is no evidence that systematic problems extend to the area of the detector covering the crucial 170 Å -> 450 Å bandpass.

The Capella spectrum is revealed in more detail after removing the off source background from the region of interest. Two methods of background subtraction were used. Since the background is found to be very uniform over the field of view the value averaged over the center of the field, excluding the source error box, is subtracted from the source spectrum. In the second approach a two parameter model spectrum consisting of a single line and constant background is fit to the data of figure 4.3a. The resulting table of χ^2 is used to set upper limits to the fluxes at each wavelength.

Application of the former procedure to the data of figure 4.3a produces the distribution shown in the top panel of figure 4.3d. The error bar indicates a one sigma deviation (about 5.2 counts) where the sigma has been computed from the data of figure 4.3a. This deviation is slightly larger than the $\sqrt{N} \sim \sqrt{23}$ because of the apparent non-statistical fluctuations in the data as discussed above.

The lower panel of figure 4.2d shows both sides of the first order spectrum added together as well as the one sigma error bar for the combined bins. Each side of first order has a sigma of 5.2 and the sigma in the combined bins is $5\sqrt{2}$ or about 7 counts. There is no clear evidence for the presence of line emission in the dispersed spectrum. As noted at the beginning of this section the location of Capella in the error box was initially chosen on the basis of a raster search of

the error box for the location of maximum counts. Since we cannot conclude from the subsequent data reduction that Capella was detected, the above analysis was repeated for several other positions in the error box with no changes in the conclusions. Upper limits to the fluxes in the prominent XUV lines expected from the Capella spectrum were set using the two sigma count level of the first order spectrum. The zero order bin was not included in this technique because of the possibility of some systematic changes in the detector sensitivity at this location. The two sigma upper limit in counts is 15 per bin. The upper limit flux (photons/cm^2-s) at earth is given in terms of the first order effective area ε_λ, and the atmospheric transmission ε_{atm} by;

$$\frac{15\text{cts}}{200s\ \varepsilon_\lambda\ \varepsilon_{atm}}$$

At 304Å this upper limit is about 0.6 ph-cm^{-2} s^{-1}. Table 4.3a presents upper limits to the prominent XUV lines in our bandpass listed by Stern, Wang, and Bowyer (1978). Interpretation of these upper limits in terms of emission models and interstellar absorption is thoroughly discussed in chapter 5.

The second method of removing background and setting upper limits fits a single line and a constant background to the data. The line is assumed to appear in both zero and first order. χ^2 was computed on a grid of values for the two parameters. 95% (2σ) confidence levels to the source flux were deduced from parameter space by the method of Lampton, Margon, and Bowyer (1976). Upper limits obtained in this manner are somewhat greater (at 304 Å $\simeq$ 0.7 ph/cm^2-s) than those obtained by the previous method. This is caused by the addition of a second free parameter representing the background and the general enhancement above the mean of the region near 0 Å which is probably not affiliated with the source. The upper limits resulting from this analysis method agree closely

with those of the direct background subtraction technique and are not shown in table 4.3a.

There is no clear evidence for the presence of line emission in the dispersed spectrum. As noted at the beginning of this section the location of Capella in the error box was initially chosen on the basis of a raster search of the error box for the location of maximum counts. Since we cannot conclude from the subsequent data reduction that Capella was detected the above analysis was repeated for several other positions in the error box with no changes in the conclusions. Capella is not detected at the prominent resonance line HeII 304Å. A two sigma upper limit to the Capella 304 Å flux at earth is set at 0.6 ph$-$ s^{-1} cm^{-2}. It is important to note that detection of the HeII 304 Å diffuse sky emission during flight provides strong evidence that the spectrometer exhibits sensitivity to 304 Å radiation, and that the absolute efficiency is consistent with and possibly greater than that deduced from the pre-flight calibration. We thus feel that the upper limits cited in table 4.3a are very plausible interpretations of the flight data.

These results represent the first XUV observations of the important Capella system and were done with sufficient sensitivity to place useful constraints on future models of the atmospheres of the binary components. These results are now interpreted in more detail.

Upper Limit Fluxes at Earth				
element	wavelength	ε_λ (cm^2)	ε_{atm}	ph cm^{-2} s^{-1}
Fe XII	187	0.31	0.92	0.25
Fe XII,VII	193-195	0.30	0.92	0.24
He II	256	0.18	0.88	0.45
He II	304	0.13	0.86	0.64
Fe XVI	335	0.09	0.84	0.94
Fe XVI	361	0.07	0.82	1.24

table 4.3a

figure 4.3a - With the Capella location deduced by the position of maximum counts in the error box, a raw count distribution is derived from the wavelength to position conversion determined by the system focal length and grating dispersion. At each wavelength the number of counts falling within a beamwidth are shown. Bins are separated by 9.4 Å.

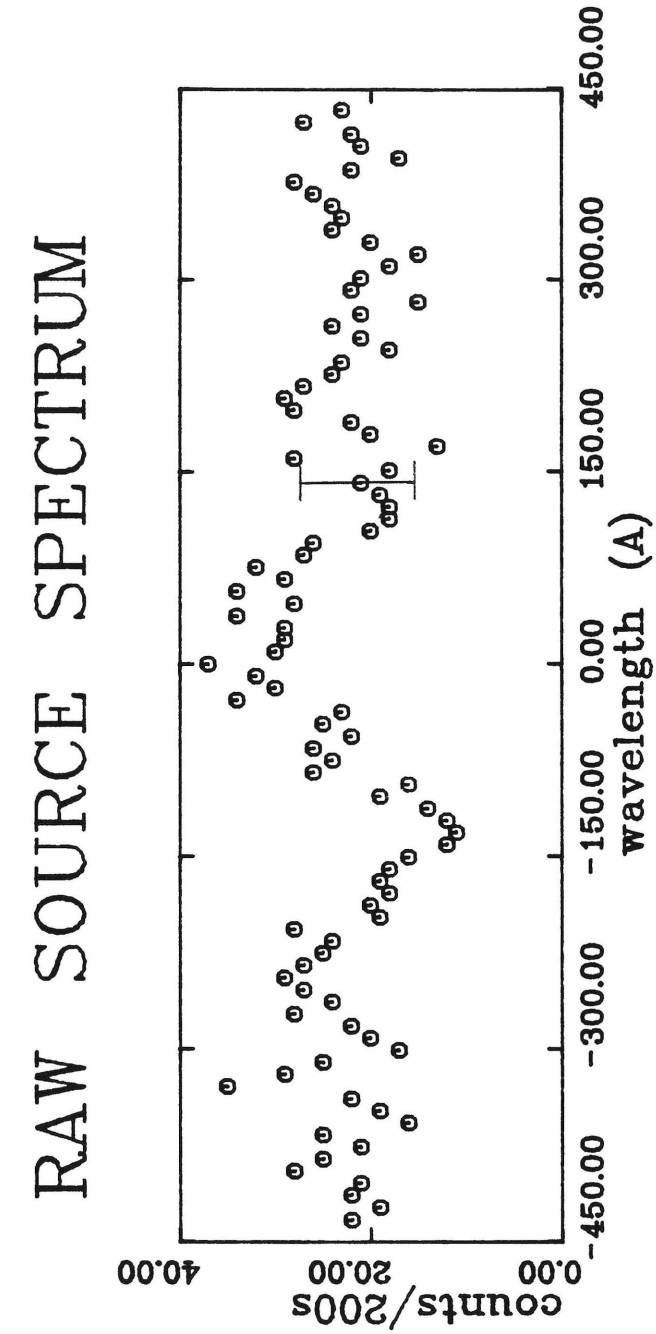
RAW SOURCE SPECTRUM
counts/200s
0.00
20.00
40.00
-450.00
-300.00
-150.00
0.00
150.00
300.00
450.00
wavelength (A)

figure 4.3a

figure 4.3b - This is a typical example of the application of the technique used to derive the raw source count distribution (figure 4.3a) to an arbitrary point in the field of view.

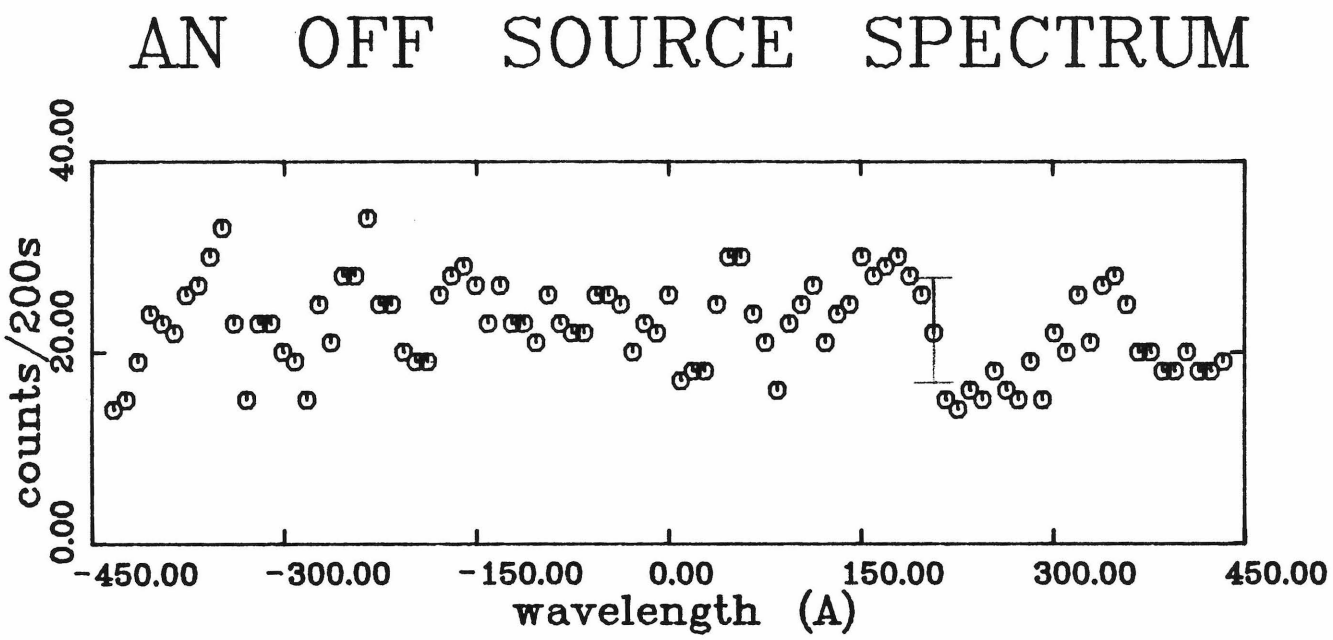
AN OFF SOURCE SPECTRUM
counts/200s
40.00
20.00
0.00
-450.00
-300.00
-150.00
0.00
150.00
300.00
450.00
wavelength (A)

figure 4.3b

figure 4.3c - In a further effort to understand the distribution of counts in the error box shown in figure 4.3a, the identical processing technique is applied to data from the same physical location, but accumulated below 200 km. Since this data set is statistically independent of that acquired above 220 km, systematic variations should be distinguishable by a correlation between the two data sets. The poor statistics counts present in this low altitude data set inhibits verification of a correlation with the data of figure 4.3a.

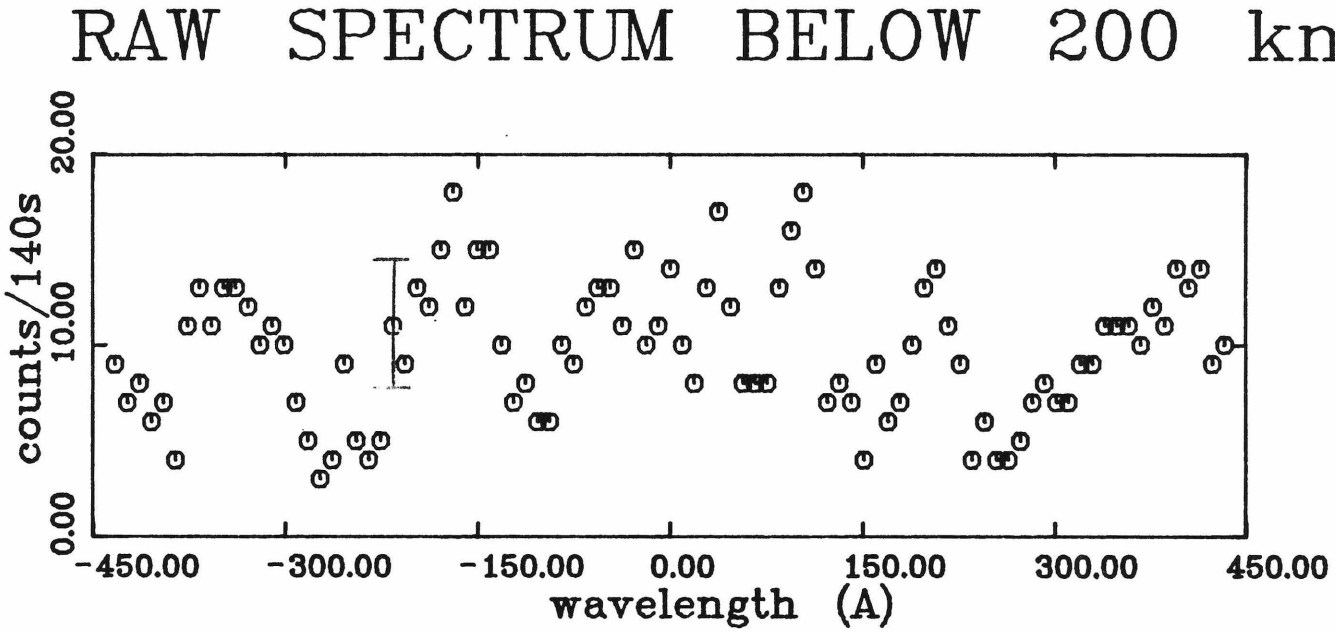
RAW SPECTRUM BELOW 200 km
counts/140s
0.00
10.00
20.00
-450.00
-300.00
-150.00
0.00
150.00
300.00
450.00
wavelength (A)

figure 4.3c

figure 4.3d - upper panel - This distribution is identical to that of figure 4.3a except that the average off source background has been subtracted from the source region. The error bar shows the one sigma deviation of the data. The residual count spectrum contains no evidence for line emission from Capella.

figure 4.3d - lower panel - The count distribution of the upper panel has been folded over so that the contributions of each side of first order are added in the same bin. The error bar indicates the one sigma error for the combined bins which is assumed to be the $\sqrt{2}$ times the single bin error shown in the upper panel. Again there is no conclusive evidence for the presence of a signal.

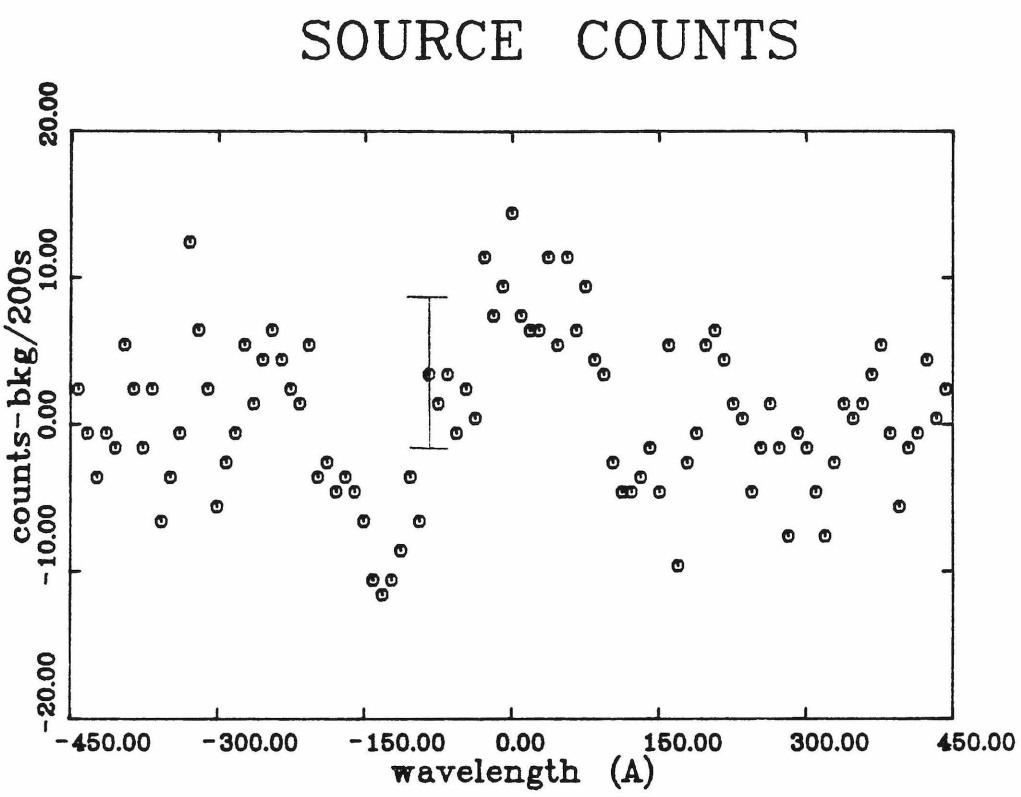
SOURCE COUNTS
counts-bkg/200s
20.00
10.00
0.00
-10.00
-20.00
-450.00
-300.00
-150.00
0.00
150.00
300.00
450.00
wavelength (A)

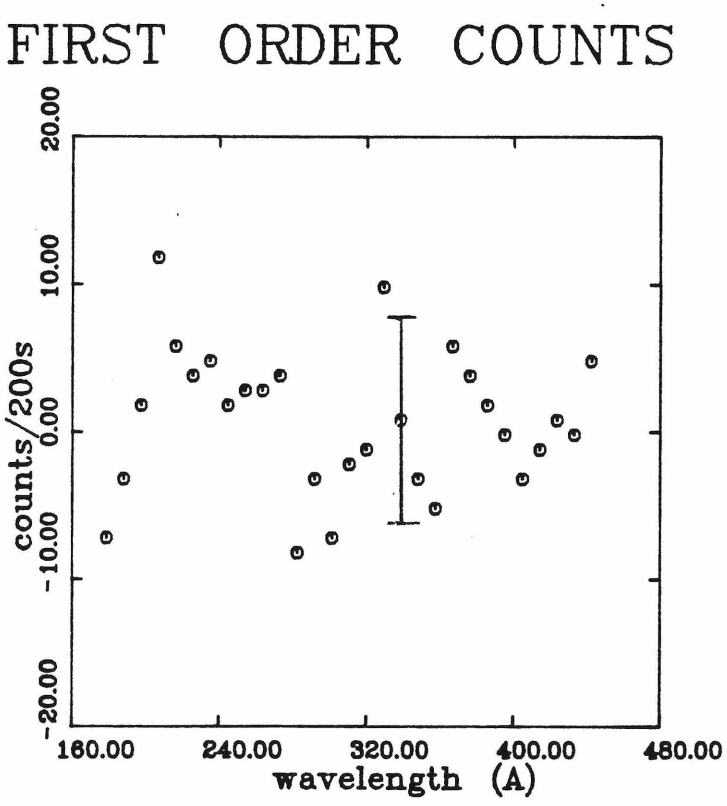
FIRST ORDER COUNTS
counts/200s
20.00
10.00
0.00
-10.00
-20.00
160.00
240.00
320.00
400.00
480.00
wavelength (A)

figure 4.3d

CHAPTER 5

5.1 INTRODUCTION

The primary result of our observation of Capella is a 2σ upper limit to the He II 304 Å flux at earth of 0.6 ph-cm^{-2}s^{-1}. A flux between 1.4 and 2.7 ph cm^{-2}s^{-1} was expected based on the ratios of Capella to solar transition region emission measures presented in the analysis of section 1.3. Two possible explanations for the discrepancy are: 1) The Capella line flux has been overestimated; 2) Attenuation in the intervening medium is significantly greater than that deduced from the observed neutral hydrogen column density and a neutral helium abundance of 10% relative to hydrogen.

The Capella 304 Å flux estimate is briefly reconsidered in section 5.2 and the conclusion reached that it would be difficult to revise the prediction downward. Several plausible attenuation mechanisms are then considered in section 5.3. A strong inference can be drawn, from our data and the Copernicus satellite observations, that the temperature in the component of the ISM along the Capella line of sight is less than 10,000 K. With the neutral hydrogen column density fixed at the Copernicus value of 1.2×10^{18}cm^{-2} (Dupree, Baliunas, and Shipman 1977) the upper limit to the flux at 304 Å reflects the total helium column density. Since the neutral hydrogen column density is known, the ionization fraction of hydrogen in the local ISM can be deduced by assuming the relative abundance of hydrogen to helium is ten. We find that the hydrogen ionization exceeds 60%. This result is compatible with the temperature, density, and ionization fraction of the interplanetary component of the ISM. Ionization is most likely maintained by an EUV radiation field in the ISM. This result fits

within the context of two (eg Bruhweiler and Kondo 1982) and three temperature phase models of the ISM (McKee and Ostriker 1977) assuming a warm cloud lies along the line of sight. Evidence that the solar system is moving through such a cloud is reviewed in the context of our observation.

5.2 The Capella HeII flux reconsidered

As noted by several authors (Avrett et al 1976, Linsky 1977, Zirin 1975) our understanding of formation of the 304 Å line in the solar transition region (TR) is deficient. A review of this problem was presented in section 1.3. Present thought and observations strongly suggest that the 304 Å resonance line is excited by electron collisions near 10^5 K in the upper transition region. Lines originated from the $n \geq 3$ states probably result from recombinations, though a combination of both mechanisms cannot be excluded for the n = 3 state (Kohl 1977). Disagreement between the collisional model predictions and observations of the total intensity of the solar 304 Å emission persist at a level of two or so. While the diffusion mechanism (Shine, Gerola, and Linsky 1975) which mixes warm ions with hot electrons may be responsible for the intensity disagreement as well as the coronal hole weakening of the line, it has not received a detailed treatment. Despite these uncertainties it is reasonable to expect that the intensity of the Capella 304 Å line will scale with the TR emission measures of Capella relative to solar under the collisional formation hypothesis. As noted in section 1.3 the EUV lines of Si IV, C IV, N V, and O VI provide ample coverage of the emission measures in the TR between 6×10^4 K and 4×10^5 K. Using the ratios of Capella to solar emission measures bypasses the need to address many specifics of the model calculations. If diffusion is responsible for enhancing the solar He II emission in active regions and decreasing it in coronal holes, we expect a similar enhancement on Capella which appears to be predominantly covered with active regions. In any case the flux should be consistent with the range 1.4 to 2.7 ph cm^{-2} s^{-1} predicted in section 1.3.

5.3 MODELS WITH ABSORPTION

Alternative explanations for the absence of a 304 Å detection in our data, based on absorption and scattering, are treated in this section. The implications of each are examined for self-consistency and compatibility with relevant observations. Models are developed on the assumption that each is the sole source of the 304 Å absorption. Combinations of various attenuation mechanisms cannot be ruled out by the data presented in this thesis.

As a starting point for this discussion origins of the absorption within the Solar System or local to Capella are considered. Mechanisms based on absorption in a warm ($T<10^4$ K), and hot ($T> 10^4$ K) local interstellar medium (LISM) are then discussed. Included in the latter case is treatment of a two phase medium consisting of an unionized warm cloud near the solar system, surrounded by a hot tenuous plasma. We find it difficult to produce the required attenuation unless the hydrogen in the warm gas is photoionized. This is consistent with either a warm uniform line of sight density to Capella or a local warm cloud surrounded by an hot, ionized plasma which does not contribute significantly to the photoabsorption at 304 Å. It should be kept in mind that the LISM is highly inhomogeneous (eg McClintock et al 1978, Cash 1978) and results pertain only to the Capella line of sight. In the notation used to refer to densities, He or H denotes the total element abundance including all ionization species, while He II denotes only the singly ionized state.

A. Attenuation in the Solar System

The presence of neutral and ionized gas in the solar system leads to the plausibility of both resonant scattering in singly ionized helium (He II), and

photo-absorption in neutral hydrogen (H I) and helium (He I), as attenuating mechanisms. Upper limits to the attenuation by both mechanisms are determined for the plasmaspheric and interplanetary mediums. Neither mechanism is found to be important.

Absorption in the plasmasphere is considered first. The cross-section for photo-ionization by He I at 304 Å is 4×10^{-18} (Cruddace et al 1974). One optical depth requires a column density N(He I) = $2.5\times10^{17}\text{cm}^{-2}$. The density of He I at 1000 km during periods of high solar activity is $\simeq10^{6}$ cm^{-3} and is 10^{4} cm^{-3} at 5,000 km (National Standard Reference Atmosphere 1976). Consequently obtaining an absorption optical depth in plasmaspheric HeI is not possible. The hydrogen contribution will be less important because the cross-section at 304 Å is only 3×10^{-19} cm^{2} and n(H I) $\leq$ n(He I). The reason for the low density of H I is that most of the hydrogen is ionized by the solar radiation field. Extending the same reasoning to the interplanetary medium where densities are < 1 cm^{-3} path lengths in excess of the scale of the solar system are required. Consequently pure absorption will be unimportant in the solar system.

The cross-section for resonant scattering by He II is large ($\simeq10^{-13}$ cm^{2}) and even though the density of He II in the plasmasphere is only $\simeq500$ cm^{-3} (Meier and Weller 1972), resonant scattering may be important. The column density of plasmaspheric He II (N(He II)) along the line of sight can be determined from our off-source measurement of the solar scattered 304 Å line described in section 4.2. Following the derivation of Meier and Weller (1972) the 304 Å intensity, I (ph-$\text{cm}^{-2}\text{s}^{-1}$) observed at peak altitude is given in terms of the solar line Flux F(λ), the absorption cross-section $\sigma(\lambda)$, and the column density $\int n(HeII)$ ds by:

$$I = \frac{1}{4\pi} p(\vartheta) \int \sigma(\lambda, T)\ F(\lambda) d\lambda \int n(\text{HeII})\ ds$$

in the single scatter (optically thin) approximation. $P(\vartheta)$ is a small correction (<10%) for the angular dependence of the scattering and is henceforth set to one. The integral of the cross-section flux product represents the rate of absorption of a 304Å photons per He II ion. Since the electron density in the plasmasphere is small each excited state radiatively decays, re-emitting the photon. The solar 304 Å profile is taken to be Gaussian with a FWHM of 0.1 Å (Doschek, Behring, and Feldman 1974). The plasmaspheric helium is assumed to be at $T \cong$ 1,000 K. For a thermally broadened absorber at 10^3 K the profile is Gaussian with a width $\simeq 0.002$Å, small compared to the solar line. In this limit the above expression for I reduces to:

$$4\pi\, I = F_0 \int \sigma(\lambda, T) d\lambda \int n(HeII)\, ds$$

where F_0 is the solar flux at line center. Using the expression for $\sigma(\lambda, T)$ from Allen (1976) the intensity becomes:

$$4\pi\, I = \frac{\pi e^2}{m_e c} f_{abs}\, F_0 \int n(HeII) ds$$

With a total integrated flux of 8×10^9 ph-cm^{-2}s^{-1} at 1 AU (Timothy 1977) and a 0.1 Å width $F_0 \simeq 8\times10^{10}$ (the solar flux may be a factor of two greater as discussed in section 4.2 however the smaller value produces a conservative upper limit estimate of N(He II)). The data of section 4.2 imply $4\pi I \simeq 16\times10^6$ phcm^{-2}s^{-1}. The absorber oscillator strength f_{abs} is 0.4123. Evaluating the above expression:

$$4\pi I \simeq (1\times10^{-2}\ \text{Hz})\ (3\times10^{-14}\text{Å Hz}^{-1})\ (8\times10^{10}\text{ph cm}^{-2}\text{s}^{-1}\text{Å}^{-1})\ \int n(HeII)\, ds$$

This results in $\int n(HeII)\, ds \leq 10^{12}$ cm^{-2}. Since the scattering cross-section at line center with $T=10^3$ K is $\simeq 10^{-13}$cm^2 the single scatter approximation is

self consistent with the upper limit column density. The fractional absorption F, of the Capella flux f (assuming no Doppler shift) is:

$$F = \frac{\int \sigma(\lambda) f(\lambda) d\lambda}{\int f(\lambda) d\lambda} \int n(HeII) ds = \frac{\pi e^2}{m_e c} f_{abs} \frac{f_0}{f_0 \Delta\lambda} 10^{12}$$

$$= \frac{3 \times 10^{-16}}{0.1 \text{Å}} 10^{12} \leq 3 \times 10^{-3}$$

Aside from the inherently low column density of He II in the plasmasphere, a major factor limiting the attenuation by He II is the narrowness of the absorber line compared to the emission line profile. As will be shown in section 5.3d even large ISM He II column densities which completely absorb the core of the line have difficulty in reducing the wings.

The column density of interplanetary He II can also be inferred from backscatter measurements, however because the solar flux falls rapidly with distance a backscatter signal originating from He further than a few AU will be lost in the plasmaspheric signal. This difficulty can be circumvented by observing through the narrow window in the plasmasphere provided by the Earth's shadow. Early sounding rocket experiments provided some evidence for column densities on the order of 5×10^{10} cm^{-2} based on this residual flux in the antisolar direction (Meier and Weller 1972; Paresce, Bowyer, and Kumar 1973). More recently a very sensitive search for backscattered 304 Å was performed by the EUV telescope on the Apollo-Soyuz mission. An upper limit of 10^9cm^{-2} was set extending out to $\simeq$ 100 AU (Paresce, Fahr and Lay 1981). The authors also considered in detail mechanisms of producing significant He II via interactions between the solar wind and the ISM and find it impossible to do so.

It is clear that under worst case assumptions we cannot account for the

failure to detect Capella at 304 Å by processes in the solar system.

B. Circumstellar Absorption

The possibility of attenuation in the Capella vicinity can be considered by analogy with the solar situation. If we assume the ISM near Capella is of similar density to the LISM the only additional source of absorbing matter will be stellar winds from the binary system. Since both stars in the system are solar-like, aside from their sizes and higher activity levels, one does not expect drastically different stellar winds. On the basis of the Copernicus EUV observations Dupree (1975) suggested the presence of a massive $10^{-8}\ M_{\odot}$ solar wind arising from the Capella primary. (At the time the EUV emission was felt, incorrectly, to originate from the primary.) This hypothesis was based on the 25 → 32 km/s blueshifts of the TR lines of N V and O VI relative to the broad Lα feature. The major problem with this interpretation of the observation was that it is very difficult to determine the wavelength of the broad Lα emission feature which is actually a superposition of the lines from both stars and hence undergoing Doppler shifts from the orbital motions. The high signal to noise ratio of the IUE has allowed detailed comparison between many TR lines and the narrow chromospheric features of O I and Si II. No evidence for blue shifts of TR lines relative to chromospheric lines is noticed (Ayres and Linsky 1980). In fact marginal evidence for a small red shift was found. Extensive surveys of cool stars in the EUV hint that these redshifts may be the result of a widespread phenomena in which TR material is carried upward and heated, then falls while radiating and cooling (Ayres 1982). Theoretical models are also not in accord with large stellar winds from bright x-ray stars (Hartmann and McGregor 1980). The underlying reason is that stars exhibiting x-ray emission are able to cool their outer atmospheres radiatively, while those without confined plasmas can only cool effectively via a

stellar wind.

It is also very difficult to produce H I, He I, or He II in a stellar wind because the high temperatures, exceeding 2×10^5 K, lead to complete ionization of hydrogen and 99% of the helium will be He III. Since the temperature of the Capella corona exceeds that of the sun by a factor of ten (Cash et al 1978) it is also reasonable to expect that the Capella solar wind would be hotter and hence further depleted in He II. Furthermore He II in the wind would not be a factor in resonant absorption because its Doppler shift relative to the stellar line will exceed 100 km/s. A crude estimate of the expected circumstellar column density can be produced by scaling the solar system upper limit of N(HeII)= $\sim 10^9 cm^{-2}$ to Capella by a factor of 50 for Capella's surface area and 100 in possible solar wind enhancement. This results in an N(He II) $\leq 10^{13} cm^{-2}$ which would be shifted well off the line. The absence of an anomalous stellar wind makes it very implausible that significant circumstellar material exists.

C. Attenuation in a Warm (T < 10,000K) ISM

The most reasonable explanation for the failure to detect the He II 304 Å emission from Capella is extinction of the line in the local interstellar medium (LISM). Considerable evidence is available to suggest that the LISM consists predominantly of two phases (Bruhweiller and Kondo 1982), a hot $10^5 \rightarrow 10^6$ K plasma with an ion density of 10^{-4} cm^{-3} interspersed with 10,000 K clouds of 10^{-1} cm^{-3}. Absorption of the stellar 304 Å photons in the LISM is considered in two parts: 1) (this subsection) In the warm phase where thermal ionization of helium and hydrogen is negligible, but photoionization of hydrogen may play a role; and 2) (subsection d) we let the temperature of the gas vary from 10,000 K to 10^6 K and compute the minimum helium column density required to produce

our result as a function of temperature. Subsection d also treats possibility of some absorption in a local warm, neutral cloud with the remainder coming from the surrounding hot plasma. In both cases, model calculations have assumed that in the absence of any ISM absorption, 3 ph-cm^{-2} s^{-1} are expected at earth and our upper limit is 0.6 ph-cm^{-2} s^{-1} (see section 1.3). After treating each model the results are compared to other relevant observations and speculations as to the nature of the LISM.

Absorption by photo-ionization in a warm medium, in which collisional ionization of hydrogen is negligible is considered. The distribution of temperature and density along the line of sight is assumed constant. The following discussion also assumes that the total (combined unionized and ionized) hydrogen and helium column densities are in a ratio of 10:1. A total interstellar transmission of less than 20% of the 304 Å flux is required.

As an initial case the line of sight column density of neutral hydrogen N(HI) compatible with our upper limit to the 304 Å flux is deduced from the assumption that N(H I) = 10 N(He I). This N(H I) is then compared with the independent Copernicus result of Dupree, Baliunas, and Shipman (1977). The photoionization cross section averaged over solar abundances is given by Cruddace et al (1974) as 6×10^{-19} cm^2 per hydrogen atom. A 20% transmission at 304 Å requires an optical depth of τ = 1.6 = N(H I) 6×10^{-19} or an N(H I) = 2.6×10^{18}cm^{-2}. This is over twice the Dupree, Baliunas, and Shipman (1977) value to which the authors assigned a 25% error. McClintock et al (1978) re-analyzed the Dupree data and suggest N(H I) may be 40-50% larger but a factor of two seems unlikely. The white dwarf G191-B2B (d=48pc) is separated in angle from Capella by only 8° and thus is expected to have a very similar N(H I). Bruhweiller and Kondo (1982) have reported N(H I) = 8.3×10^{17}cm^{-2} for this line of sight, providing strong evidence for a column density as low as 1.2×10^{18}cm^{-2} in the Capella direction. For

the remainder of this discussion N(H I) is fixed at the Copernicus level of $1.2\times10^{18}cm^{-2}$.

Within the assumptions about the intervening medium set down at the beginning of this treatment it is still possible to produce < 20% transmission with a fixed N(H I) if the hydrogen is partially ionized, which allows N(H) to vary. With a $\sigma_{HI} = 3\times10^{-19}$ cm^2 and $\sigma_{HeI} = 4\times10^{-18}$ cm^2 τ is given by:

$$\tau = (1.2\times10^{18})\,(3\times10^{-19}) + N(HeI)\,(4\times10^{-18}) = 1.6$$

This implies that N(HeI) $\geq 3\times10^{17}cm^{-2}$. N(HI)/N(HeI) is found to be ≤ 4. In a relatively warm ISM helium is unionized and the ratio N(H):N(HeI) = 10:1. The ionization fraction of Hydrogen must be:

$$\frac{N(HII)}{N(H)} = 1-\frac{N(HI)}{N(H)} = 1-\frac{N(HI)}{10N(HeI)} \geq 1-\frac{4}{10} \simeq 60\%$$

In the absence of collisional ionization this n(H II):n(H I) must be maintained by an EUV component of the EUV radiation field.

Grewing (1975) has used this hypothesis to account for the ionization populations of C, N, Mg, Al, Si, and S measured by Copernicus along the line of sight to four stars within 120 pc. Because the ionization thresholds vary the ionization state of each of the above species samples the proposed interstellar radiation field at a different wavelength. Thus he was able to reconstruct the spectral shape of the field in the EUV and XUV required to support the observed ionization fractions. He found it consistent with both a black-body at 1×10^4 K and the spectrum of an early B star. Furthermore he concluded that the density of B stars within the solar neighborhood is sufficient to accommodate the locally observed ionization states.

To place this interpretation of our data in the framework of Grewing's model we compare the photo-ionization rate J required to support our result for H such that N(H II)/N(H) ≥ 0.5, with the values Grewing derived for the heavier elements. J is expressed as an integral of the ISM radiation field with the photoionization cross- section for hydrogen ($\sigma(\lambda)$) above threshold. Designating $F(\lambda)$ as the model ISM radiation field and taking the conventional form for $\sigma(\lambda)$ near the threshold λ_0, J is given by:

$$J = \int_0^{\lambda_0} \sigma(\lambda)\, F(\lambda) d\lambda$$

With the cross-section;

$$\sigma(\lambda) = \sigma(\lambda_0)\, \frac{\lambda^3}{\lambda_0{}^3}$$

In an equilibrium situation recombination balances photo- ionization so that J is simply related to the electron density n_e, and the recombination coefficient α by:

$$n(H\ I)J = \alpha\, n(H\ II)\, n_e$$

Combining the above relations cross-section weighted integral of the ISM field F (λ) is expressed in terms of known and observable parameters.

$$\frac{1}{n_e} \int \frac{\lambda^3}{\lambda_0{}^3} F(\lambda) = \frac{n(HII)}{n(HI)} \frac{\alpha}{\sigma(\lambda^0)} \equiv X(\lambda_0)$$

To evaluate the above expression for X(13.6eV) we take $\alpha = 5\times10^{-13}cm^{-3}s^{-1}$ at a temperature of 8,000 K (Spitzer 1978). $\sigma(\lambda_0)$ is $6\times10^{-18}cm^2$. Our data provide a lower limit to the ratio n(H II)/n(H I) of $\simeq$ 1.

This translates to an upper limit on the log($X(\lambda_0)$) of $\simeq$ 5 at an energy of 13.6 eV. In figure 5.3a we have reproduced values of X determined by Grewing based on the ionization states of heavier elements. Values shown are for the three closest stars of his survey, α Leo (d=26pc), α Eri (d=40pc), and λ Sco (d=100pc). The figure includes our point at 13.6 eV. The predictions for a 10^4K blackbody, and an early B star spectrum are also indicated. The datum for H is clearly consistent with this model.

An attempt to observe the ISM radiation field was carried out with the EUV spectrometers on the two Voyager spacecraft (Sandel, Shemansky, and Broadfoot 1979). After substantial corrections for cosmic rays, internally scattered Lyα photons, and point source contamination the authors suggest that the residual flux below 912 Å is an order of magnitude greater than that demanded by the above model. In light of the complicated background subtraction required it is reasonable to conclude that their results provide support for the presence of an EUV ISM radiation field.

Some direct observational support for a warm and partially ionized medium along the Capella line of sight is available. The average line of sight temperature has been inferred from the deuterium absorption profile obtained from the Copernicus observations of Capella. Both Dupree, Baliunas, and Shipman (1977) and McClintock et al (1978) find $T < 10^4$ K. Diverse measurements of the temperature in the component of the ISM flowing through the solar system indicate 8000 K < T < 15,000 K (for a review see Meier 1980). Meier also reviews satellite and backscatter measurements of the local n(H I), and n(He I). He finds mutual agreement at an n(H I) = 0.04cm^{-3}, and n(He I) = 0.01cm^{-3}. More recent data based on the pioneer 10 spacecraft Lα and 584 Å observations imply n(H I) = 0.04 +/- 0.01 cm^{-3}, n(He I) = 0.01 +/- 0.002 cm^{-3} (Wu et al 1981). An abundance ratio of 10 requires 60% of the hydrogen to be ionized. These local values

are consistent with the limits derived from our data.

D. Attenuation in a hot (T > 10,000K) ISM

In this discussion we attempt to explain the attenuation of the Capella 304 Å flux without invoking photoionization of the ISM, but maintaining consistency with the Copernicus measure of the neutral hydrogen column density to Capella. A collisionally maintained ionization equilibrium at an electron temperature T is assumed. The neutral hydrogen column density is fixed at $1.2\times10^{18}\mathrm{cm}^{-2}$. Under these assumptions the total helium column density N(He) required to produce an ISM transmission < 20% at T is derived for the range $1{,}000\mathrm{K}<T<10^{6}\mathrm{K}$.

The dependence of the ISM transmission at 304 Å (D_{ism}) on the cross-sections σ_x, the column densities N(x), the temperature T, and the Capella 304 Å profile $f_c(\lambda)$ is:

$$D = e^{-\sigma_{HI}N(HI)}\, e^{-\sigma_{HeI}N(HeI)} \int e^{-\sigma_{HeII}(T,\lambda)N(HeII)}\, f_c(\lambda)\, d\lambda$$

The relative amounts of He I and He II are strong functions of temperature. The ratios N(He I)/N(He) and N(He II)/N(He) are defined to be:

$$\zeta^{I}(T) = N(HeI)/N(He) \quad \text{and} \quad \zeta^{II}(T) = N(HeII)/N(He)$$

where the ionization fractions $\zeta^{x}(T)$ are taken from the equilibrium calculations of Cox and Tucker (1969). With these coefficients inserted in the previous expression the transmission depends only on the total N(He).

$$D_{ISM} = e^{-\sigma_{HI}N(HI)}\, e^{-\sigma_{HeI}\zeta^{I}(T)N(He)} \int e^{-\sigma_{HeII}(T,\lambda)\zeta^{II}N(He)}\, f_c(\lambda)\, d\lambda$$

The HeII scattering profile is taken to be gaussian with a width determined primarily by the temperature. A small ($\simeq$ 5 km/s) additional contribution from ISM

turbulence (McClintock et al, 1978) is included. The source profile is also gaussian with a width of 0.1 Å by solar analogy (Doschek, Behring, and Feldman 1974). Broadening by rotation has been ignored. An important uncertainty in the calculation is the emitter to absorber Doppler shift. This is estimated to be at least comparable to the line of sight component of the Capella orbital velocity of 20 km/sec.

The lower limit helium column density derived from this model is shown in figure 5.3b as a function of temperature. The right axis is in units of ion density if we assume the ISM is uniform along the Capella line of sight. At low temperatures helium is unionized and the lower limit is constant. When the temperature is of the order of $2-3\times10^4$ a small fraction of the helium is singly ionized and the required column density decreases slightly. The reason for this is that the He I absorbs out the wings of the line, and the He II removes the core where it has a very large absorption cross-section. As T increases the He I disappears and the wings return until the temperature of the ISM approaches the temperature of line formation. Then interstellar He II is broadened sufficiently to resonantly scatter the entire line. Above 2×10^5 the dominant component of the medium is He III and the required column density increases rapidly. The total hydrogen column density is also displayed in the figure We have assumed that $N(H\ I)=1.2\times10^{18}cm^{-2}$ and used the ionization fractions of House (1963) to determine temperature dependence of N(H). The dashed line indicates the N(He) if the abundance relative to hydrogen is 0.1. As noted earlier, thermal models are inconsistent with this abundance ratio at temperatures below 10^4 K unless the warm hydrogen is partially ionized. If n(H) is restricted to values not much greater than $1cm^{-3}$ the allowed region in temperature is rather small and is not consistent with the earlier cited Copernicus observations of the temperature.

Considerable evidence is mounting for a picture of the LISM in which the solar system is moving through a cloud of warm gas of about four parsecs diameter. The cloud is surrounded by a hot 10^5 K to 10^6 K plasma which is expected to be roughly in pressure equilibrium with the warm gas (Bruhweiller and Kondo 1982). In this two phase model the Copernicus N(H I) to Capella corresponds to a total density of hydrogen in the warm cloud of about 0.05 cm^{-3} if it is unionized and 0.1 cm^{-3} if the ionization fraction is 50%. If the warm gas is *unionized* then the optical depth at 304 Å in the warm cloud is 0.72, identical to the opacity estimate of section 1.3. The hot plasma must then be responsible for an additional attenuation of at least 60% to give a combined transmission less than 20 % at 304 Å. As for the single phase model we compute the total N(He) required for a 40% transmission in the hot phase. This lower limit is indicated by the curve in figure 5.3b labeled the two phase model. The corresponding density scale on the right axis is applicable for the helium density if multiplied by 1.5, assuming the hot medium occupies $2/3^{rd}$ of the line of sight.

The helium column density in the hot medium can further be constrained by requiring approximate pressure equilibrium with the warm cloud. If the warm cloud is unionized then n(H) = n(H I) = 0.1cm^{-3}. The pressure nT is $\cong 0.1\times10^4$ K = 10^3 cm^{-3} K. Equating pressures in the two regions and using n(He) = 0.1 n(H) requires a helium density in the hot plasma of (0.1) $\times(10^{-3})/T_5$. Converting to column density by multiplying by 2/3 the Capella distance = $0.67\times(4\times10^{19})$cm we find that $N(He) =\sim \frac{2.8\times10^{16}\ cm^{-2}}{T_5}$. Comparing this with the two phase model N(He) in figure 5.2b column densities are consistent for temperatures near 10^5 K,while temperatures exceeding 2×10^5 K are less plausible. Models of the ISM generally require the temperature of the hot component to be on the order of 5×10^5 K (McKee and Ostriker 1977). A careful

consideration of temperature constraints imposed by both soft x-ray and XUV data has been undertaken by Paresce and Stern (1981). For models in which warm gas clouds are interspersed with the hot gas they find that isothermal models require $10^{5.3}$ K < T < $10^{5.5}$ K, not inconsistent with our column density. The region of mutual consistency between the column density of He required to provide 40% transmission and the pressure equilibrium density is quite small and we feel that a two phase medium in which hydrogen in the warm phase is unionized is not likely.

Figure 5.3a - The horizontal axis gives the threshold ionization energy in eV for an ionization level. The vertical axis is the quantity X, defined in the text. This figure compares the measured ionization fractions of N, C, Si, Mg, and S with hypothetical values derived from the assumption that a photoionization-recombination equilibrium dominates the steady state structure of the LISM. The solid line is a 10,000 K blackbody spectrum while the dashed line is a B 1.5 V star spectrum. Lines above (below) the markers represent upper (lower) limits while the remaining points are detections. The marker at 13.6 eV for hydrogen is from this experiment and is not inconsistent with the other data. This figure has been adapted from Grewing (1975).

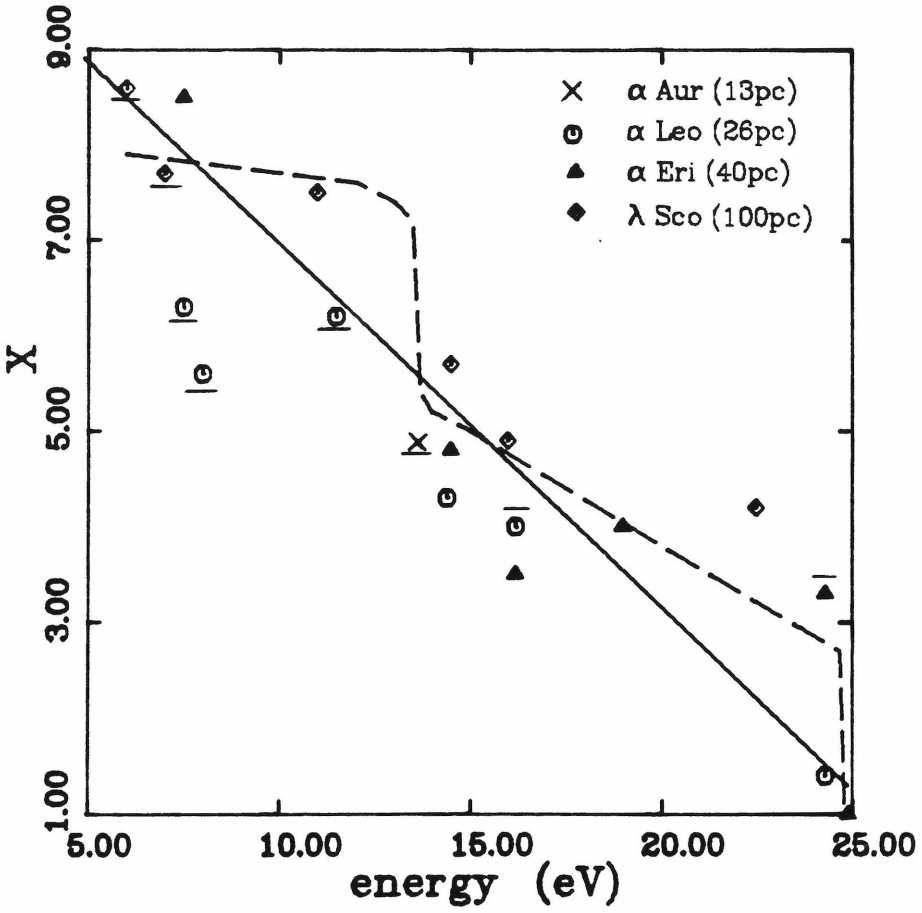
α Aur (13pc)
α Leo (26pc)
α Eri (40pc)
λ Sco (100pc)
X
9.00
7.00
5.00
3.00
1.00
5.00
10.00
15.00
20.00
25.00
energy (eV)

figure 5.3a

Figure 5.3b - The vertical scale gives the total line of sight column density on the left, and the corresponding space density (cm^{-3} on the right for a uniform distribution on the line of sight. The density scale will not apply for the curve labeled two phase as explained in the text. The horizontal scale gives the temperature.

The solid curves labeled He reflect the LISM He column densities required to attenuate the Capella 304 Å line sufficiently to be compatible with our upper limits as a function of temperature. The single phase medium assumes that the line of sight medium is uniform in temperature and density. The line labeled H gives the total N(H) as a function of temperature consistent with n(HI) measured by Copernicus. Photoionization is assumed to be negligible. Under these circumstances the He to H abundance at low temperatures is close to 0.25 instead of 0.1. Agreement with the solar abundance is only possible for T on the order of 20,000 K since higher temperatures would generate very large interstellar particle densities. This temperature is twice that measured by Copernicus (Dupree, Baliunas, and Shipman). We doubt that such a single phase model without photo-ionization correctly accounts for the state of the LISM

The two phase model assumes the solar system is immersed in a cool cloud of four parsecs radius, which is neither collisionally or photoionized. This cloud is surrounded by a hot plasma at temperature T. N(H I) in this cloud is set to the Copernicus value and N(He I)=N(H I). The curve shows the required N(He) in the surrounding hot phase. As discussed in the text this N(He)is only consistent with a pressure equilibrium of the two phase for $T \cong 10^5$ K.

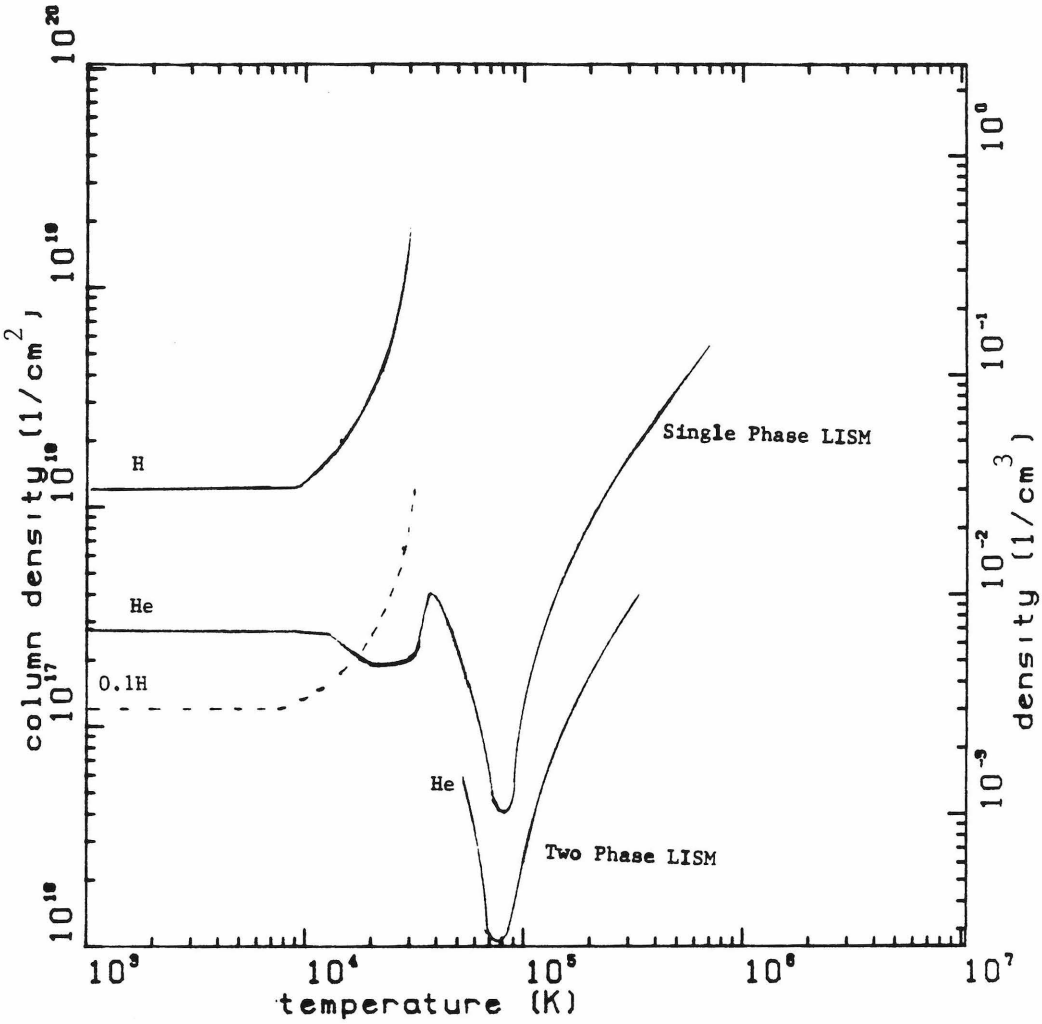
column density (1/cm^2)
density (1/cm^3)
temperature (K)
H
He
0.1H
He
Single Phase LISM
Two Phase LISM

figure 5.3b

5.4 Coronal Line Emission in the bandpass

In table 4.3 upper limits were presented to several prominent TR and coronal lines falling within our bandpass. The only possible detection is at 195 Å in the first order spectrum of figure 4.3d however it appears at the two sigma level. The volume emissivity in an XUV line is generally very sensitive to the plasma temperature in the region of formation. Consequently upper limits to line fluxes can be used to constrain the Capella emission measure at the line temperatures given a production model. Stern, Wang, and Bowyer (1978) have calculated the XUV spectrum of a hot, tenuous plasma of solar abundance. The lines of greatest volume emissivity (ε_{vem} ergs $cm^{-3}s^{-1}n_e^{-2}$) in our bandpass include the iron group (Fe VIII 186 Å, 196 Å; Fe XI 194 Å; Fe XII 194 Å, 195 Å) near 195 Å and Fe XVI 335 Å, 361 Å. Of these the strongest are the iron group at 195 Å. Furthermore both the spectrometer efficiency and ISM transmission are greatest at short wavelengths. The emission measure ($\int n_e^2\, dV$) is given in terms of the upper limit flux F_e, the optical depth τ and the distance to Capella (d) by:

$$\int n_e^2\, dV = \frac{F_e\ 4\pi\ d^2}{\varepsilon_{vem}\ e^{-\tau}} \qquad cm^{-3}$$

There are two alternative methods of evaluating τ. One is two assume N(He I) = 0.1 N(H I) with N(H I) = 1.2×10^{18} cm^{-2} (Dupree, Baliunas and Shipman 1977) which leads to a τ of 0.24. The opacity may also be computed on the reasonable hypothesis that N(He I) = 0.25 N(H I) based on the analysis of the 304 Å flux upper limit (section 5.3c). We find τ = 0.45 for the photoionized ISM model. The Fe group at 195 Å is formed near a temperature of 1.6×10^6 with a very sharp cutoff for $T \gtrsim 2.5\times10^6$. Summing the emissivities of the four Fe lines at 195 Å gives $\varepsilon_{vem} \simeq 1.5\times10^{-13}$ ph $cm^{-3}s^{-1}n_e^{-2}$. The upper limit flux is about 0.25

photons $cm^{-2}s^{-1}$. Evaluating the above expression leads to $\int n_e^2\, dV \leq 4\times10^{52}$ for τ = 0.24. This result can be compared to the emission measure determined from the HEAO I and Einstein soft x-ray observations. The HEAO I data (Cash et al 1978) were fit to an isothermal, solar abundant, plasma. The best fit temperature was about 10^7 K at an emission measure of $10^{53}cm^{-3}$, however the 90% confident limits included an emission measure of $10^{52}cm^{-3}$ at T = 2×10^6, suggesting possibly a blend of temperatures. Einstein observations with the high resolution solid state spectrometer provided very detailed spectra showing lines of Mg, Si, S, and Fe (Holt et al 1979). Using a two temperature model the best fit emission measures were $4\times10^{52}cm^{-3}$ at T = 8×10^5K and $1.2\times10^{52}cm^{-3}$ at T = 4.6×10^7 K. These values of the emission measures are comparable to the upper limit given by the XUV flux, and would also be consistent with a detection at 195 Å.

The FeXVI 335 Å, 361 Å lines are formed at a temperature of $4\rightarrow6\times10^6$. We note that the volume emissivity of these lines is about 1/3 the 195 Å lines while the instrument efficiency has also declined by more than a factor of three at these wavelengths.Since the optical depth of the ISM also substantially exceeds that at 195 Å (τ at 335 Å is 1.7), sensitivity is greatly reduced. At 335 Å the upper limit emission measure is 1.5×10^{54} cm^{-3} compared to largest value allowed by Holt et al (1979) of 10^{53}.

5.5 Summary

If one accepts the range of Capella 304 Å flux predictions cited in table 1.3a, then the upper limits reported in this thesis provide the first direct measurements of the local interstellar helium abundance. In section 5.3c it was demonstrated that a line of sight medium with a temperature of about 10^4 K, a mean density of neutral hydrogen of 0.04 cm^{-3}, and a He I density greater than 0.01 cm^{-3} will account for the absence of the 304 Å line in our data. These parameters are consistent with the density and temperature of the interplanetary medium, but photoionization of hydrogen at a level exceeding 60% must be invoked to maintain compatibility with a 10:1 abundance ratio of hydrogen to helium, as well as with the Copernicus temperature determination. This implies the existence of an interstellar EUV radiation field. Section 5.3d presented attempts to account for the attenuation in a uniform line of sight medium at temperature T > 10,000 K as well as with a two phase medium. In the single phase model only a very narrow temperature region at 20,000 K is allowed if we expect that n(H) does not exceed 1.0 cm^{-3} and the hydrogen is not photoionized. This value for the temperature is clearly inconsistent with the Copernicus value of T =~ 10,000 K (Dupree, Baliunas, and Shipman 1977). The two phase model can account for the upper limit without invoking photoionization, however the region of overlap between the N(He) required to maintain the attenuation and that required for approximate pressure equilibrium restricts the temperature to a very narrow range around 10^5 K. A small decrease in the 304 Å upper limit, or ion density will remove the region of compatibility. This lack of robustness of the two phase model without photoionization leads one to suspect its plausibility. We thus find it difficult to account for the absence of the Capella He II resonance line in our data without invoking an interstellar XUV radiation field which ionizes hydrogen.

These conclusions are not incompatible with hypothesis that the solar system is immersed in a five parsec diameter warm gas cloud surrounded by a hot plasma as suggested by Bruhweiller and Kondo (1982). We note that the average H I density in such a cloud is about 0.1 cm^{-3} from the Copernicus value of N(H I) = $1.2 \times 10^{18} cm^{-2}$ which is somewhat greater than the 0.04 cm^{-3} of the interplanetary medium (Meier 1980). Since the cloud may of course be inhomogeneous this is not a major discrepancy.

Our results are also consistent with the three phase model of the ISM proposed by McKee and Ostriker (1977). This model presumes that the ISM is inhomogeneous and time varying. The main structures are defined by interactions between expanding supernovae shells and the ambient medium. In this dynamic model three distinct temperature components are required for self-consistency. The authors predict the ISM is filled by a hot, tenuous, coronal gas of (n,T) = (0.003 cm^{-3} , $10^{5.7}$K) interspersed with dense, warm clouds. The low temperature cloud cores have (n,T) = ($40 cm^{-3}$, 100K). Cloud boundaries are hypothesized to have a temperature of $\cong$ 8,000 K and densities of order 0.2 cm^{-3}. A 10% ionization fraction of the warm core is maintained by soft x-rays while the hot boundary is proposed to be ionized at the 70% level by hot B stars. The scale of the boundary region can be as large as ten parsecs, hence capable of filling a large fraction of the LISM. Based on the data of this thesis, and the additional satellite observations of the LISM, it is not unreasonable to suppose that the solar system and the Capella line of sight are mostly contained in such a environment.

Future XUV observations of nearby stars hold much promise for answering questions about the temperature and helium densities in the LISM, as well as those dealing with the atmospheric physics of nearby stars. The accessibility of the XUV to observation has been based on the very low neutral hydrogen column

densities measured along the lines of sight to numerous nearby stars. If we are correct in explaining the upper limit to the Capella 304 Å flux in terms of photoionization of interstellar hydrogen, the opacity of the ISM may be substantially greater than that deduced from the neutral hydrogen column densities and a neutral hydrogen to neutral helium ratio of ten in a warm ISM. This will require higher sensitivities of future XUV telescopes.

In a much broader sense we have learned that the structure of the LISM is not well understood, and that the problems of discerning its structure and probing the atmospheres of nearby stars in the XUV are interwoven.

REFERENCES

Acuna, M. C., Hinds, P. L., Statel, R. J., Cannon, R. T., and Niswander J. K., 1976 "The Sounding Rocket Division Airborne PCM System," published by NASA, Goddard Space Flight Center, Greenbelt, MD.

Agrawal, P. C., Garmire, G. P., Riegler, G. R., Tuohy, I. R., 1974, unpublished paper.

Allen, C. W., in *Astrophysical Quantities*, 1973, Athlone Press, London.

Athay, R. G., White, O. R., 1978, *Ap. J.*, **226**, 1135.

Avrett, E. .H., Vernazza, J. E., Linsky, J. L., 1976, *Ap. J. (Letters)*, **207**, L199.

Ayres, T. R., 1982, preprint

Ayres, T. R., Linsky, J. L., 1980, *Ap. J.*, **241**, 279.

Ayres, T. R., Marstad, N. C., Linsky, J. L., 1981, *Ap. J.*, **247**, 545.

Brauninger, H., Lenzen, R., Trumper, J.,in *New Instrumentation for Space Astronomy*, ed. K. A. van der Hucht and G. Vaines, 1978, Pergamon Press, Oxford.

Brinkman, A. C., Dijkstra, J. H., Geerlings, W. F. P. A. L., van Rooijen, F. A., Tinnerman, C., Korte, P. H. J., 1979, *Applied Optics*, **19**, 1601.

Bruhweiler, F. C., Kondo, Y., 1982, *Ap. J.*, **259**, 232.

Brunner, E. C., McWhirter, R. W. P., 1979, *Ap. J.*, **231**, 557.

Cash, W., Bowyer, S., Charles, P., Lampton, M., Garmire, G., and Riegler, G., 1978, *Ap. J. (Letters)*, **223**, L21.

Cash, W., Bowyer, S., Lampton, M., 1979, *Astronomy and Astrophysics*, **80**, 67.

Catura, R. C., Acton, L. W., Johnson, H. M., 1975, *Ap. J. (Letters)*, **196**, L47.

Cox, D. P., Tucker, W. H., 1969, *Ap. J.*, **157**, 1157.

Cruddace, R., Paresce, F., Bowyer, S., Lampton, M., 1974, *Ap. J.*, **187**, 497.

Doschek, G. A., Feldman, U., Mariska, J. T., Linsky, J. L., 1978, *Ap. J. (Letters)*, **226**, L35.

Doschek, G. A., Behring, W. E., Feldman, U., 1974, *Ap. J. (Letters)*, **190**, L141.

Dupree, A. K., 1975, *Ap. J. (Letters)*, **200**, L27.

Dupree, A. K., Baliunas, S. L., Shipman, H. L., 1977, *Ap. J.*, **218**, 361.

Dupree, A. K., in *Cool Stars, Stellar Systems and the Sun Workshop*, 1980, Smithsonian Astrophys. Observatory, Special Report No. 389

Dupree, A. K., 1981, *Space Science Reviews*, **29**, 479.

Ederer, D. L., Ebner, S. C., *A User Guide to SURF* 1975, National Bureau of Standards, Gaithersburg, MD.

Glackin, D. L., Linsky, J. L., Margo, S. A., Bohlin, J. D., 1978, *Ap. J.*, **222**, 707.

Gerola, H., Kafatos, M., McCray, R., 1979, *Ap. J.*, **189**, 55.

Gorenstein, P., Tucker, W., 1976 *Ann. Rev. Astr. Ap.*, **14**, 373.

Grewing, M., 1975, *Astronomy and Astrophysics*, **38**, 391.

Hall, D., 1978, *Ap. J.*, **83**, 1469.

Hartmann, L., MacGregor, K. B.,preprint 1980

Hartmann, L., Dupree, A. K., Raymond, J. C., 1981, *Ap. J.*, **252**, 214.

Hearn, A. G., 1969, *M. N. R. A. S.*, **142**, 53.

Holt, S. S., White, N. E., Becker, R. H., Boldt, E. A., Mushotzky, R. F., Serlemitsos, P. J., Smith, B. W., 1979, *Ap. J. (Letters)*, **234**, L65.

Holzer, T. E., Axford, W. I., 1971, *J. G. R.*, **76**, 6965.

House, L. L., 1963, *M. N. R. A. S.*, **196**, 307.

Huber, M. C. E., Foukul, P. V., Noyes, R. W., Reeves, E. J., Schmahl, E. J., Timothy, J. G., Vernazzo, J. E., Withbroe, G. L., 1974, *Ap. J. (Letters)*, **194**, L115.

Iben, I., 1965, *Ap. J.*, **142**, 1447.

Jacchia, L. G., 1970, SAO special report 322

Jordan, C., 1975, *M. N. R. A. S.*, **170**, 429.

Kellogg, E., Henry, P., Murray, S., Van Speybroeck, L., Bjorkholm, P., 1976, *Reviews of Sci. Instruments*, **47**, 282.

Kohl, J. L. 1977, *Ap. J.*, **211**, 958.

Lampton, M., Paresce, F., 1974, *Reviews of Sci. Instruments*, **45**, 1098.

Lampton, M., Margon, B., Bowyer, S., 1976, *Ap. J.*, **208**, 177.

Lapson, L. B., Timothy, J. G., 1976, *Applied Optics*, 15, 1218.

Linsky, J. L., Ayres, T. R., 1978, *Ap. J.*, **220**, 619.

Linsky, J. L., Haisch, B. M. 1979, *Ap. J. (Letters)*, **127**, 1979.

Linsky, J. L., 1980, in *Cool Stars, Stellar Systems, and the SUN*, ed. A. K. Dupree, Smithsonian Astrophys. Observatory, Special Report 389.

Liu, S. Y., 1974, *Ap. J.*, **189**, 359.

Lukirskii, A. P., Savinov, E. P., Brytov, I. A., Shepelev, Y. F., 1964, *USSR Acad. of Sci., Bull. of Physics*, **28**, 774.

Macau, J. P., Jamar, J., Gardier, S., 1976, *IEEE Transactions on Nuclear Science*, **23**, 2049.

Mack, J. E., Bowyer, S., Paresce, F., 1976 *Applied Optics*, **15**, 86.

Malina, R. F., Bowyer, S., Paresce, F.,1978, in *X-Ray Astronomy*, ed. W. A. Baity, L. E. Peterson, Pergamon Press, Oxford.

Mango, S. A., Bohlin, J. D., Glackin, D. L., Linsky, J. L., 1978, *Ap. J.*, **220**, 683.

McClintock, W., Henry, Linsky, J. L., Moos, 1978, *Ap. J.*, **225**, 465.

McKee, C., Ostriker, J., 1977, *Ap. J.*, **218**, 148.

McCray, R., Snow, T. P., 1974, *Ann. Rev. Astron. Astrophys.*, **17**, 213.

Meier, R. R., 1980, *Astron. Astrophys.*, **91**, 62.

Meier, R. R., Weller, C. S., 1972, *Journal of Geophys. Research*, **77**, 1190.

Mewe, R., Heise,J., Gronenschild, E. H. B. M., Brinkman, A. D., Schrijver, J., Den Boggende, A., 1975, *Ap. J. (Letters)*, **202**, L67.

Milkey, A. W., 1975, *Ap. J. (Letters)*, **199**, L131.

Milkey, R. W., Heasley, J. N., Beebe, H. A., 1973, *Ap. J.*, **186**, 1043.

Mount, G., Rottman, G., 1981,*Journal of Geophys. Research*, **86**, 9193.

Mullen, D. J., 1978, *Ap. J.*, **226**, 151.

NASA *The U.S. Standard Reference Atmosphere* 1976, NASA, NOAA, USAF.

NOAA *Solar Geophysical Data - Prompt Reports* pub. National Oceanic and Atmospheric Administration.

Paresce, F., Bowyer, S., Kumar, S., 1973a, *Ap. J. (Letters)*, **183**, L87.

Paresce, F., Bowyer, S., Kumar, S., 1973b, *Journal of Geophys. Research*, **78**, 71.

Paresce, F., Fahr, H., Lay, G., 1981, *Journal of Geophys. Research*, **86**, 10038.

Paresce, F., Kumar, S., Bowyer, S., 1971, *Applied Optics*, **10**, 1904.

Paresce, F., Stern, R., 1981, *Ap. J.*, **247**, 89.

Predehl, P., Haelbich, R. P., Brauninger, H., 1979, *Applied Optics*, **18**, 2906.

Riegler, G. R., Garmire, G., 1979, *Journal of Geophys. Research*, **79**, 226.

Rottman, G. 1981, *Journal of Geophys. Research*, **86**, 6697.

Saloman, E. B., 1978, *Applied Optics*, **17**, 1489.

Saloman, E. B., 1980, *Nuclear Instruments and Methods*, **172**, 79.

Saloman, E. B., Ederer, D. L., 1975, *Applied Optics*, **14**, 1029.

Samson, J. A. R., 1967, *Techniques of Vacuum Ultraviolet Spectroscopy*, John Wiley & Sons, New York.

Sandel, B. R., Shemansky, D. E., Broadfoot, A. L., 1979, *Ap. J.*, **227**, 808.

Schnopper, H. W., Van Speybroek, L. P., Delvaille, J. P., Epstein, A., Kallne, E., Bachrach, R. Z., Dijkstra, J., Lautward, L., 1977, *Applied Optics*, **16**, 1088.

Shine, R., Gerola, H., Linsky, J. L., 1975, *Ap. J. (Letters)*, **202**, L101.

Spitzer, L., 1978, in *Physical Processes in the Interstellar Medium*, Wiley and Sons, New York.

Stein, R. F., Leibacher, J., 1974, *Am. Rev. Astr. Ap.*, **12**, 407.

Stern, R., Wang, E., Bowyer, S., 1978, *Ap. J. Suppl. Series*, **37**, 195.

Stevens, K. T., 1974, *Electronic Design*, **4**, 96.

Timothy, J. G., in *The Solar Spectrum and Its Variation*, ed. White, O. R., Univ. of Colorado Press, Boulder, 1977

Torr, M. R., Torr, D. G., Ong, R. A., Hinteregger, H. E., 1979, *Geophysical Research Letters* **6**, *76*.

Ulmschneider, P. 1979, *Space Sci. Rev.*,

Ulmschneider, P., Schmitz, F., Renzini, A., Cacciari, C., Kalhofer, W., Kurucz, R. L., 1977, *Astron. Astrophys.*, **61**, 515.

Vaiana, G. S., Rosner, R., 1978, *Ann. Rev. Astron. Astrophys.*, **16**, 393.

Vaiana, G. S., Cassinelli, J. P., Fabbiano, G., Giaconni, R., Golub, L, Gorenstein, P., Haisch, B., Harnden, F., Johnson, M., Linsky, J., Maxson, C., Mewe, R., Resner, R., Seward, F., Topka, K., Zwaan, C., 1981, *Ap. J.*, **245**, 163.

Walter, F. M., Linsky, J. L., Bowyer, S., Garmire, G., 1980, *Ap. J. (Letters)*, **236**, L137.

Weller, C. S., Meier, R. R., 1981, *Ap. J.*, **246**, 386.

Wiza, J. L., 1979, *Nuclear Instruments and Methods*, **162**, 587.

Wu, F. M., Suzuki, K., Carlson, R. W., Judge, D. L., 1981, *Ap. J.*, **245**, 1145.

Zirin, H., 1975, *Ap. J. (Letters)*, **199**, L63.